Advanced Signal Processing Methods for Analysis of Cortico-Muscular Coherence

Xu, Yuhang

Awarding institution:
King's College London

Advanced Signal Processing Methods for Analysis of Cortico-Muscular Coherence

Yuhang Xu

Department of Informatics

King's College London

This dissertation is submitted for the degree of

Doctor of Philosophy

March 2018

Acknowledgements

First and foremost, I would like to express my sincere gratitude to Professor Zoran Cvetković for accepting me to the PhD programme and for his continuous support, patience, motivation and inspiration. His guidance helped me in all the time of research.

Besides, I am grateful to Dr. Verity M. McClelland and Professor Kerry R. Mills for their guidance on neuroscience, for the fruitful collaboration and constant encouragement. Without them, this journey would not have been possible.

I would also like to thank Dr. Matthew Howard for inviting me for their group activities and for his helpful advice on giving presentations, and to thank Dr. Wei Dai for his guidance on dictionary learning.

Special thanks go to my friends for giving me a shoulder to lean on when I was in trouble, for picking me up when I was down, and for sharing with me happiness and wonderful moments.

Last but not least, I would like to thank my family, who has always had my back and believed in me. I owe all the achievements to them. Especially, I wish to thank my beloved grandfather, who inspired me to study abroad. Although you can only remember the "little me" because of the disease you got after my leaving, I will always love you.

Abstract

This thesis is concerned with signal processing methods which can be applied to electroencephalogram (EEG) and electromyogram (EMG) signals for identifying interactions between the brain and muscles of human subjects. An experimental framework for assessing methods is developed and neurophysiological data and simulated data are used to illustrate the potential of the proposed methods. The concept of cortico-muscular coherence with time lag (CMCTL) is introduced. A methodology based on CMCTL for discovering temporal relationships between synchronised activities in the brain and muscle is developed. Simulated data are used to demonstrate that under certain conditions the time lag obtained by the method corresponds to the average delay along the involved cortico-muscular conduction pathways. Experimental results show that the method enhances the coherence between cortical and muscle signals, and that time lags which correspond to local maxima of CMCTL provide estimation of delays involved in cortico-muscular coupling. The time delays obtained by the proposed method are more mutually consistent and in a closer agreement with the underlying physiology compared to the delays obtained by some state-of-the-art methods. Two approaches for noise removal based on Wavelet Independent Component Analysis and Sparse Signal Representation are developed. A component selection algorithm is proposed for use in these methods to reconstruct a version of signal which contains relatively higher levels of coherent components with respect to

the considered activity. The methods achieve a pronounced enhancement to the cortico-muscular coherence, resulting in up to a three times increase in CMC levels for physiological data.

Table of contents

List of figures

List of tables

List of Symbols and Acronyms

$(x)_+$: $\max(x,0)$

$\mathbf{A}^T$: transpose of matrix $\mathbf{A}$

$\mathbf{A}^{-1}$: inverse of matrix $\mathbf{A}$

$\oplus$: orthogonal sum of vecter spaces

$\|\cdot\|_0$: ℓ_0-norm

$\|\cdot\|_1$: ℓ_1-norm

$\|\cdot\|_2$: ℓ_2-norm

$\|\cdot\|_F$: Frobenius norm

arg $\min\{f(x)\}$: value of x that minimises the function $f(x)$

$\text{sgn}(\cdot)$: sign function

$A \subset B$: A is a subset of B

$E(\cdot)$: expectation operator

$f^*(x)$: complex conjugate of $f(x)$

ADMM: alternating direction method of multipliers

BSS: blind sourse separation

CL: confidence limit

CMC: cortico-muscular coherence

CMCTL: cortico-muscular coherence with time lag

COWICA: coherent wavelet enhanced independent analysis

DTF: directed transfer function

DWT: discrete wavelet transform

EEG: electroencephalogram

EMG: electromyogram

FDI: first dorsal interosseous

FIR: finite impulse-response

FPB: flexor pollicis brevis

ICA: independent component analysis

LTI: linear time-invariant

MOD: method of optimal directions

MSE: mean-square error

MVC: Maximum voluntary contraction

OMP: orthogonal matching pursuit

RIP: restricted isometry property

sEMG: surface electromyogram

SNR: signal-to-noise ratio

STFT: short-time Fourier transform

SVD: singular value decomposition

TFA: time-frequency analysis

WCs: wavelet components

WGN: white Gaussian noise

WICA: wavelet independent component analysis

WICs: wavelet independent components

WT: wavelet transform

WTD: wavelet threshold denoising

Chapter 1

INTRODUCTION

1.1 Motivation

Millions of people worldwide suffer from various types of movement disorders, such as Parkinson's disease, stroke, dystonia, cerebral palsy and multiple sclerosis. Patient-specific treatment strategies are needed for them, but their development is still an unmet clinical need. Although there are new therapies that are well-established, a lack of scientific knowledge regarding the underlying pathophysiology results in the benefits of these new therapies for movement disorders to not be fully realised. The concept that not only the motor system disturbances but also abnormalities of sensory pathways, processing or abnormal sensorimotor integration are involved in the disorders is being accepted by more and more people [1, 2]. An essential way to understand sensorimotor control is to identify the specific cortico-muscular interactions. They provide important information concerning the bidirectional communication between the cortex and muscle as well as on how the motor command is modulated by sensory information. Therefore, unravelling the interactions between cortical sensorimotor activity and the

muscle is key to understanding the underlying physiology and exploring more individualised therapies.

The mechanisms of cortico-muscular interactions can be studied by analysing electroencephalogram (EEG) and electromyogram (EMG) signals which are recorded synchronously from the sensorimotor cortex and muscle, respectively, during controlled movement tasks. The advantages of such neuophysiological techniques are that they are resource efficient, non-invasive and most critically offer the required time-resolution which cannot be achieved by imaging approaches. In this context, cortico-muscular coherence (CMC) analysis, which detects the presence of synchronous components in electrophysiological recordings from the brain and concurrently active muscles, is one of the most common signal processing methods [3–5]. The spectral technique of CMC has become one of the primary methods for quantifying functional coupling between the motor cortex and muscle activities [6–10] since Conway found the initial evidence in humans relating to the significant coherence between motor cortex EEG and surface EMG (sEMG) of the first dorsal interosseous (FDI) muscle during constant isometric contractions [4]. Evidence that CMC is of functional importance includes the findings that CMC in the β range is task dependent [3, 8], related to motor performance [11, 12] and modulated differentially by various types and intensities of afferent stimuli [13, 14], specifically where the stimulus is functionally relevant to the on-going motor task [13, 14]. There is also evidence showing that the information flow is not just from the brain to the muscle but instead bidirectional [12, 14–17] and abnormal CMC patterns are reported in patients with dystonia and Parkinson's disease [18–20]. These studies indicate that EEG and EMG signals recorded synchronously during controlled movement tasks contain substantial information that is needed to understand the mechanisms of cortico-muscular interactions.

However, CMC is often very weak and even some healthy subjects do not express CMC above a significant threshold. There are two known factors that could weaken CMC, one of which is the misalignment between EEG and sEMG signals due to the time delay between synchronised processes in the muscle and the cortex [21–23]. The other factor is the presence of noise and components unrelated to the considered activity in both EEG and sEMG. Since CMC reveals protocols of cortico-muscular interactions, providing information which is required to understand mechanisms of movement control and how they are disrupted in movement disorders [24–26], it is of great importance to be able to enhance the CMC levels. The thesis concentrates on delay estimation between EEG and EMG signals, as well as denoising methods for removing components irrelevant to the observed activity.

1.1.1 Time delay between coherent EEG and EMG events

EEG and EMG events that are coherent do not occur simultaneously, but rather with a delay which reflects signal propagation between the brain and the muscle as well as possible information processing. If it is not accounted for, this delay may decrease the level of coherence [27], and thus make the cortico-muscular coupling difficult or impossible to detect. Here, a cortico-muscular coherence with time lag (CMCTL) function, which is the coherence between segments of the motor cortex EEG and EMG signals displaced from a central observation point is proposed, and it is shown that CMCTL enhances the level of CMC and provides more detailed information about the temporal structure of cortico-muscular interactions than the conventional CMC. Afterwards, an algorithm is proposed for the estimation of the delay between coherent EEG and EMG events. The algorithm amounts to finding the time lag which maximises local coherence. In addition to its relevance

of enhancing the CMC, knowing the time delay between the motor cortex and the periphery can reveal important information regarding the communication between motor cortex and muscles by characterising the direction via which the oscillations propagate and/or by differentiating the cortico-spinal pathways via which the activity is transmitted. This information is significant as it not only increases our fundamental understanding of the physiology of cortex-muscle interactions, but also increases the potential utility of cortico-muscular coherence for use as a clinical and research tool.

A method which is widely used on the identification of time delays in biological systems is based on the estimation of the slope of the phase of cross spectral density corresponding to considered processes [28–31]. This approach has however produced conflicting results [5, 7, 16, 32] and also suffers from some methodological problems. In particular, the slope of the cross spectral density is well defined only if the two processes are connected via a linear-phase system, which is in general not the case when it comes to cortico-muscular pathways. This issue has been addressed by Lindemann *et al.* [30] who proposed using the Hilbert transform to identify and remove the phase component which is non-linear and then to estimate the delay from the remaining linear component. Unfortunately, their work has rarely been used in physiological studies, which could be due to its technical sophistication and underlying assumptions which are difficult to verify in practice. Furthermore, there is evidence of bidirectional connectivity in the motor control system [14–17] and the delay estimated from the phase spectrum being subject to errors if the coupling is bidirectional within the estimated period [33, 34]. Although some groups have considered directed coherence based on the Granger causality [16, 35–37], which in principle can discern different propagation directions, the results vary much from individual to individual. Moreover,

there could be more than one event in the observation period and the delay of each event could be different. Finally, many groups perform EMG rectification prior to the calculation of CMC, which introduces non-linear distortion of the EMG signal and its phase spectrum [21].

The concept of delay estimation via the time offset which maximises coherence of two signals has been previously applied successfully to acoustic signals [38]. It has also been used in the context of cortico-muscular interactions, however with limited success [39] and under the assumption of continuous constant-delay flows of information within narrow frequency bands, which may not be applicable to biological signals such as EEG and EMG [39]. The authors conclude that further work is needed to make the method applicable to non-stationary events [39]. The concept is revisited in the thesis with a series of modifications that make it yield delay estimates that are consistent with underlying physiology. More importantly, the interpretation of the results provided by the method in the context of multi-path propagation, which is a more realistic model of the channels of cortico-muscular communications, is studied.

1.1.2 Noise components involved in EEG and EMG signals

Another factor which decreases the CMC levels, in addition to the time delay, is the noise component involved in the recordings. The use of electrodes placed on the scalp to record EEG results in a very small amplitude. Moreover, EEG is often contaminated by artefacts from various sources such as breathing, eye movements and the heartbeat. On the other hand, sEMG which indicates the functional state of muscle fibres, is often recorded from the skin surface. sEMG can also be affected by contaminations, such as movement of the subject as well as cross-talk from other muscles [40–42]. When quantifying functional coupling, sEMG can be

represented as a linear combination of several motor unit signals, in addition to noise, which consists of not only artefacts but also other signals unrelated to the considered cortical activity [22, 23].

Wavelet denoising algorithms have been widely used to eliminate noise in biological signals [43–45], especially when it comes to the removal of white Gaussian noise (WGN). However, when dealing with suppressing the components which have high energy concentrated in narrow bands, wavelet denoising algorithms may lose their efficiency. Another algorithm that is very successful for noise reduction of multi-channel biological signals is independent component analysis (ICA) [46–49]. However, this algorithm requires data from sufficiently many channels to be able to separate the sources. In order to overcome such limitations, some groups proposed to apply wavelet decomposition prior to ICA to generate wavelet components (WCs) leading to increased redundancy, since the event that can be found in just one original channel is now found in several wavelet components [50–53]. Moreover, although ICA is typically very effective for finding artefacts, it is less effective for extracting components related to cortical activities [54].

Two methods are proposed for the enhancement of relevant components of EEG and sEMG, one of which is based on the concept of Wavelet Independent Component Analysis (WICA), which has been proposed previously in the context of artefact rejection from EEG signals [50–53, 55]. This study focuses on increasing the relative level of coherent components in the mixture of signals collected by sEMG. A method is proposed to apply ICA to low-channel count sEMG signals with the aim of minimising the costs and complexity of the operation for data collection, and then select components from the mixture using a greedy algorithm that aims to maximise the coherence between the resynthesised sEMG signal and EEG.

The other method for extracting coherent components is based on dictionary learning and sparse signal representation. A natural signal could be redundant and a few measurements may be enough for its reconstruction. The sparse representation may capture the inherent structure of signals. This technique is widely used in signal reconstruction, especially for image processing such as image compression and inpainting [56, 57]. Sparse representations are also applied to biological signals [58–61]. Dictionary learning and sparse representation is used here in order to represent components of interest in EEG and sEMG signals using a few waveforms from their corresponding highly structured dictionaries. Thus, extraction of coherent components from EEG and EMG signals is facilitated and CMC enhancement is achieved.

1.2 Thesis Structure

This thesis consists of six chapters. Chapter 2 provides the background and reviews some related existing approaches with respect to the analysis of CMC. A simplified model of the motor control system, which is assumed to be linear time-invariant (LTI) is introduced and will be used for further coherence analysis. Relevant aspects of coherence analysis are reviewed and two major factors that influence the level of coherence are discussed. Finally, the algorithms regarding solving the problems caused by those two factors are presented, with a discussion on the limitations of previous methods.

Chapter 3 presents an experiment in which EEG and EMG data were collected for further study. The general experimental arrangement, the positions of electrodes for recording EEG and EMG signals and the pre-processing of the data are introduced. Conventional coherence analysis of the recordings is demonstrated.

CMCTL methodology is developed Chapter 4, which is applied to the time delay estimation between EEG and EMG. The transmission between EEG and EMG is via multiple paths. The notion of the global delay is introduced to define the delay involved in the multi-path model. The physical interpretation of the global delay is explored through both mathematical expressions and simulations. CMCTL is used as the method for estimating the global delay and examples of CMCTL applied to physiological data with results of delay estimation are presented. Furthermore, healthy subjects which do not express significant CMC are considered.

Chapter 5 proposes two methods which could extract the coherent EEG and sEMG components, so that the coherence between reconstructed EEG and sEMG would increase to a relatively high level. One of these methods is inspired by WICA and is referred to as Coherent Wavelet Enhanced Independent Analysis (COWICA). A component selection algorithm for selecting coherent components in this method is proposed for use. Experimental results are presented along with a comparison to the results obtained using the wavelet threshold denoising technique. In addition, a combination of the CMCTL and COWICA methodologies are considered and discussed. Dictionary learning and sparse representation techniques are utilised in the other proposed denoising method. A component selection algorithm which is analogous to the one used in COWICA is applied for further extraction of coherent components from EEG and sEMG signals. Results concerning CMC enhancement are presented by applying the methods to both simulated and neurophysiological data.

The conclusion is given in Chapter 6 and possible directions for future research are presented.

1.3 Contributions and Relevant Publications

The main contributions of this thesis are listed as follows:

- The CMCTL is developed with the potential to enhance CMC and reveal finer temporal structures of cortico-muscular interactions compared to the conventional CMC.
- An algorithm is proposed for the delay estimation between coupled cortical and muscle activities by investigating the time lag corresponding to the local maxima of the CMCTL. The analysis and interpretation of CMCTL in the context of multi-path propagation is provided. Delay estimates obtained by applying the proposed algorithm to physiological data are in close agreement with the underlying physiology.
- A method is developed, inspired by WICA, for CMC enhancement in situations where there is a small number of channels for ICA to be able to separate the independent sources.
- A method based on dictionary learning and sparse signal representation to extract coherent components from simultaneously recorded EEG and sEMG signals is developed, which leads to a significant increase of CMC.

The relevant publications are listed as follows:

1. Y. Xu, V. M. McClelland, Z. Cvetković, and K. R. Mills, "Delay estimation between EEG and EMG via coherence with time lag," in Proceedings of *IEEE International Conference on Acoustics, Speech and Signal Processing (ICASSP)*, March 2016, pp. 734-738. (Chapter 4)

2. Y. Xu, V. M. McClelland, Z. Cvetković, and K. R. Mills, “Corticomuscular coherence with time lag with application to delay estimation,” *IEEE Transactions on Biomedical Engineering*, vol. 64, no. 3, pp. 588–600, March 2017. (Chapter 4)

3. Y. Xu, V. M. McClelland, Z. Cvetković, and K. R. Mills, “Cortico-muscular coherence enhancement via coherent wavelet enhanced independent component analysis,” in Proceedings of *39th Annual International Conference of the IEEE Engineering in Medicine and Biology Society (EMBC)*, July 2017, pp. 2786-2789. (Chapter 5)

4. Y. Xu, Q. Yu, W. Dai, Z. Cvetković, and V. M. McClelland, "Cortico-muscular coherence enhancement via sparse signal representation," presented at *IEEE International Conference on Acoustics, Speech and Signal Processing (ICASSP)*, Calgary, Alberta, Canada, April 2018. (Chapter 5)

Chapter 2

BACKGROUND AND RELATED WORK

The thesis directly focuses on the two main factors which weaken the coherence between signals from the motor cortex and the muscle: time delay and the noise component. Many previous works have provided methods for either delay estimation between the cortex and its periphery or denoising of EEG and sEMG. However, these methods suffer from limitations and/or methodological problems and some traditional methods also produce conflicting results [5, 7, 16, 32].

This chapter is organised as follows. Section 2.1 introduces a model of motor control system. In Section 2.2, relevant aspects of coherence analysis are reviewed. Section 2.3 and Section 2.4 discuss the methodologies proposed in previous studies for delay estimation between EEG and EMG as well as the denoising algorithms for noise removal in biological signal processing, respectively.

2.1 Simplified Model of Motor Control System

Cortical events propagate to the periphery and the motor cortex receives input from the periphery [6, 9, 17]. Let us first consider a scenario in which information transmission is unidirectional between the cortex and periphery. This transmission is not instantaneous, instead it has a delay which is primarily caused by the transmission speed of the neural conduction. Cortical activity is transmitted to the motor neurones within the spinal cord via the corticospinal tract, which contains nerve fibres of differing conduction velocities. Therefore, each of them may introduce a different delay and attenuation. Each motor neurone innervates multiple fibres within the muscle comprising a motor unit. The noiseless response $y_i(t)$ of a motor unit i can thus be represented as a linear combination of delayed and attenuated versions of the cortical signal $x(t)$, that is

$$y_i(t) = \sum_{k=0}^{K_i} \alpha_{i,k} x(t - T_i - \tau_{i,k}) \,, \tag{2.1}$$

where $\alpha_{i,k}$ are attenuations, while T_i and $\tau_{i,k}$ are delays of individual fibres, defined so that T_i is equal to the minimal delay within the motor unit which contains K_i fibres and $0 = \tau_{i,0} \leq \tau_{i,1} \leq \ldots \leq \tau_{i,K_i}$. Within the pick up area of an electrode, there are several motor units that would be recruited by the same cortical activity [64–67]. Therefore, sEMG signal $y(t)$ is a linear combination of several motor unit signals, as well as signals unrelated to the considered cortical activity, which will be collectively referred to as noise. The sEMG signal thus has the form

$$y(t) = \sum_{i=1}^{I} \beta_i y_i(t) + n(t) \,, \tag{2.2}$$

where β_i factors represent the attenuation of the pathways between particular motor units and the electrode, while $n(t)$ is the noise and I is the number of involved motor units. Expressed in terms of the cortical event $x(t)$ the sEMG signal therefore has the form

$$y(t) = \sum_{i=1}^{I} \sum_{k=0}^{K_i} \beta_i \alpha_{i,k} x(t - T_i - \tau_{i,k}) + n(t) \ , \tag{2.3}$$

that is, $y(t)$ is a sum of delayed and amplitude-scaled versions of $x(t)$. To simplify the notation, in the following, the above model will be expressed as

$$y(t) = \sum_{i=1}^{N} b_i x(t - D_i) + n(t) \ , \tag{2.4}$$

where N is the number of different pathways involved in the model, b_i and D_i are the attenuations and delays, respectively, corresponding to the different pathways. One can introduce more complex models of individual fibres, and the propagation between motor units and the electrode, but as long as all stages along the path are modelled as linear filters, the overall system between the cortex and the sEMG electrode will be a causal, finite-impulse-response (FIR), linear time-invariant (LTI) system, the most general form of which is given by (2.4). Under excitations of small amplitude and within limited time intervals, the systems can be well approximated by LTI systems [68, 69]. Besides, the coherence analysis applies only to processes connected via LTI systems, hence our model is not any more restrictive than the fundamental assumptions of coherence analysis.

An analogous model can be established for transmission of sensory events from the periphery. Hence in the case of bidirectional signalling sEMG signal has

the form

$$y(t) = y_0(t) + \sum_{i=1}^{N_x} b_{x,i} x_0(t - D_{x,i}) + n_y(t) \ , \tag{2.5}$$

while the EEG signal has the form

$$x(t) = x_0(t) + \sum_{i=1}^{N_y} b_{y,i} y_0(t - D_{y,i}) + n_x(t) \ , \tag{2.6}$$

where $x_0(t)$ is the cortical event that performs muscle control, whereas $y_0(t)$ is the sensory event which is transmitted to the cortex, while $n_x(t)$ and $n_y(t)$ are the noise components. N_x and N_y indicate the number of descending and ascending pathways, respectively. Attenuations $b_{x,i}$, $b_{y,i}$ and delays $D_{x,i}$, $D_{y,i}$ correspond to x and y as shown in the subscripts.

2.2 Coherence Analysis

Cortico-muscular coupling is commonly detected and quantified by means of coherence analysis. The coherence $C_{xy}(\omega)$ between two stationary processes $x(t)$ and $y(t)$ is defined as

$$C_{xy}(\omega) = \frac{|S_{xy}(\omega)|^2}{S_{xx}(\omega) S_{yy}(\omega)} \ , \tag{2.7}$$

where $S_{xx}(\omega)$ and $S_{yy}(\omega)$ are their power spectral densities, and $S_{xy}(\omega)$ is their cross spectral density [70]. Notice that $C_{xy}(\omega)$ is called coherence in the thesis and agrees with some references [70, 71], but is the squared magnitude of the defined coherence in some others [72, 73]. The value of coherence is a real number between 0 and 1, with 0 indicating a complete absence of linear association between two processes such that they are totally incoherent and 1 indicating a perfect linear association such that two processes are completely coherent.

Section 2.2.1 describes the time-frequency representation of coherence, which turns the coherence between non-stationary processes into the coherence between stationary processes corresponding to different time intervals. In section 2.2.2, two main factors that could weaken the coherence are put forward and discussed.

2.2.1 Time-frequency representation

Time-frequency analysis (TFA) studies a signal in both the time and frequency domains simultaneously. Compared to the classical Fourier analysis which assumes that signals are periodic or infinite in time, TFA works better in practice being suitable for a wider range of signals which are of a short duration and change substantially over their durations [74].

Short-time Fourier transform (STFT) [72, 75] is the most basic form of TFA. In the discrete time case, the signal to be transformed could be broken up into frames by a window $w(t)$ shifting along the whole period. A Fourier transform is performed with each frame centred at time t_c. Thus in the discrete time case, the STFT of a signal $x(t)$ can be expressed as [76]

$$\mathbf{STFT}\{x(t)\}(t_c,\omega) \equiv X(t_c,\omega) = \sum_{t=-\infty}^{\infty} x(t)w(t-t_c)e^{-j\omega t} \,. \tag{2.8}$$

The STFT has a fixed resolution which depends on the length of the window function. Wavelet transform (WT) is another common technique of TFA which has multiresolution. Generally, the WT of discrete time series $x(t)$ can be expressed as

$$\mathbf{WT}\{x(t)\}(t_c,\omega) \equiv W_x(t_c,\omega) = \sum_{t=-\infty}^{\infty} x(t)\psi^*_{t_c,\omega}(t), \tag{2.9}$$

where * is the complex conjugate symbol and $\psi_{t_c,\omega}(t)$ is the analysing wavelet shifted and scaled by both scale and position parameters [77–79]. There are several wavelet functions with different shapes and properties. For the wavelet coherence analysis of physiological signals, it has been demonstrated that the Morlet wavelet is a good choice because of its simplicity, smooth spectrum and the good balance between localisation in time and frequency domains [78, 80].

When the coherence between non-stationary processes is estimated via the STFT [75], it segments the signals into intervals over which their statistical properties remain fairly constant. To that end, a window of a finite duration T is placed at a discrete set of time instants, $t_c = n\Delta t,\ n \in \mathbb{Z}$, and for each window position, the discrete Fourier transform of the windowed signal is computed at frequencies $\omega_c = 0, \Delta\omega, \ldots, (M-1)\Delta\omega,\ \Delta\omega = \frac{\Omega_s}{M}$ where Ω_s is the sampling frequency, and M is the size of the discrete Fourier transform. In this manner time-frequency representations

$$x(t) \xrightarrow{STFT} X(t_c, \omega_c)$$
$$y(t) \xrightarrow{STFT} Y(t_c, \omega_c)$$

are obtained, where $X(t_c, \omega_c)$ and $Y(t_c, \omega_c)$ reflect events within the time-frequency support of the window centred around (t_c, ω_c).

An analogous representation under the WT can be obtained as

$$x(t) \xrightarrow{WT} W_x(t_c, \omega_c)$$
$$y(t) \xrightarrow{WT} W_y(t_c, \omega_c),$$

where the set of time instants t_c and frequencies ω_c depend on the position and vectors' scale, respectively.

In neurophysiological studies, the STFT is typically estimated using windows of length $T = 500$ ms, with shifts Δt between 250 ms and 500 ms. Some transient events, however, are much shorter and could be easily obscured by the use of such a short-time Fourier analysis (STFA) as it reflects cumulative effects of all events within the window. Shorter windows would therefore be more suitable for the analysis of the transient phenomena. However, a better time resolution comes at the expense of a worse frequency resolution, and it is important to ensure that the bandwidth of the window does not considerably exceed the frequency range of interest.

Once an adequate time-frequency resolution of spectral analysis is decided upon, the time varying power spectral and cross-spectral densities are estimated by averaging the STFT magnitude spectra over different epochs (trials):

$$\hat{S}_{xx}(t_c, \omega_c) = \frac{1}{L} \sum_{n=1}^{L} |X_n(t_c, \omega_c)|^2 \,, \tag{2.10}$$

and analogously for $\hat{S}_{yy}(t_c, \omega_c)$, while

$$\hat{S}_{xy}(t_c, \omega_c) = \frac{1}{L} \sum_{n=1}^{L} X_n(t_c, \omega_c) Y_n^*(t_c, \omega_c) \,, \tag{2.11}$$

where L is the number of epochs. Therefore, the coherence between $x(t)$ and $y(t)$ is estimated as

$$C_{xy}(t_c, \omega_c) = \frac{|\hat{S}_{xy}(t_c, \omega_c)|^2}{\hat{S}_{xx}(t_c, \omega_c) \hat{S}_{yy}(t_c, \omega_c)} \,. \tag{2.12}$$

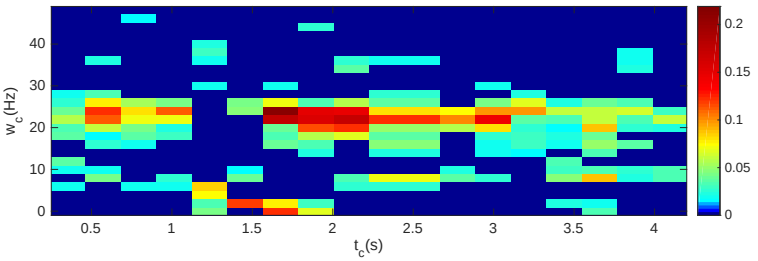

(a)

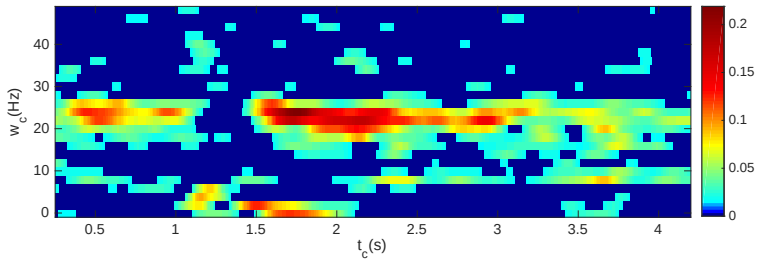

(b)

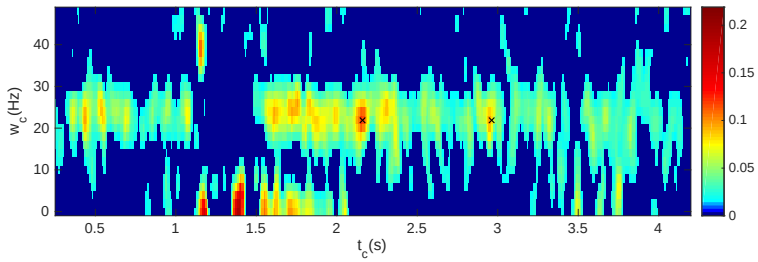

(c)

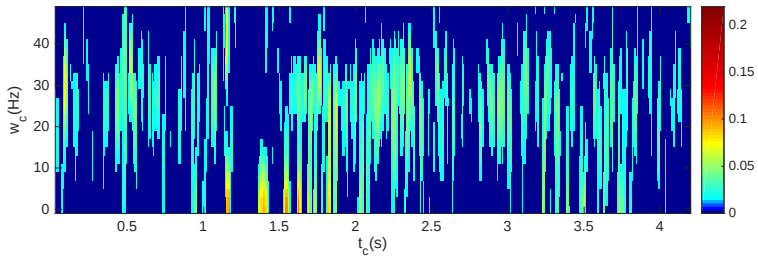

(d)

Fig. 2.1 CMC plots obtained with different time-frequency resolutions of spectral estimation, illustrating its effect on the information revealed by the subsequent coherence analysis. The STFT is computed at $M = 512$ frequencies using Hanning windows of different lengths T and with different shifts Δt between consecutive windows. CMC values below the 95% confidence limit are set to zero. (a) $T = 500$ ms, $\Delta t = 250$. (b) $T = 500$ ms, $\Delta t = 9.8$ ms. (c) $T = 125$ ms, $\Delta t = 9.8$ ms; two most prominent peaks, marked by $\times$ signs, will be referred to in Chapter 4. (d) $T = 62.5$ ms, $\Delta t = 9.8$ ms.

Analogous to the short-time Fourier based coherence (2.12), the wavelet coherence $CW_{xy}(t_c, \omega_c)$ is defined by

$$CW_{xy}(t_c, \omega_c) = \frac{|\hat{SW}_{xy}(t_c, \omega_c)|^2}{\hat{SW}_{xx}(t_c, \omega_c)\hat{SW}_{yy}(t_c, \omega_c)} , \tag{2.13}$$

where the power and cross-spectrum are estimated in the wavelet domain with $W_x(t_c, \omega_c)$ and $W_y(t_c, \omega_c)$ over different epochs (trials) in the same way as (2.10) and (2.11).

Significant coherence can be defined by setting the confidence limit (CL) to 95% which is estimated as

$$CL_{(a\%)} = 1 - \left(1 - \frac{\alpha}{100}\right)^{\frac{1}{(L-1)}} , \tag{2.14}$$

where α is set to 95 and L is the number of trials used in the estimation of auto- and cross-spectra [81].

The effects of time-frequency resolution trade-offs in CMC analysis are illustrated in Fig. 2.1 using EEG and EMG signals collected during a controlled motor task (see Chapter 3). Signals are sampled at 1024 Hz. The STFT used for the CMC plot in Fig. 2.1(a) is computed using a Hanning window of length $T = 500$ ms (512 samples), at $M = 512$ frequencies, corresponding to $\Delta\omega = 2$ Hz, and with $\Delta t = 250$ ms (256 samples). The coherence plot in Fig. 2.1(b) is obtained using the same STFT parameters, however, in an attempt to refine the time resolution of the analysis Δt is reduced to $\Delta t = 9.8$ ms (10 samples). For the CMC analysis plotted in Fig. 2.1(c), the STFT is computed using a Hanning window of length $T = 125$ ms (128 samples), whereas the time shift is kept at $\Delta t = 9.8$ ms. The coherence plot in this figure suggests that communication between the brain and muscle involves a sequence of transient events (seen on the plots in Fig. 2.1(a)

and Fig. 2.1(b)), corresponding to the 500 ms analysis window, that are merged into what appears to be one longer event, even when the shift between consecutive analysis windows is decreased to $\Delta t = 9.8$ ms. The effect of reducing the length of the analysis window further is illustrated in Fig. 2.1(d), which shows the CMC plot obtained using Hanning window of length $T = 62.5$ ms (64 samples), with $\Delta t = 9.8$ ms. The time-frequency resolution of the STFT in this case does not match well with that of the cortico-muscular signals, which results in lower coherence levels, in addition to a poor frequency resolution.

Fig. 2.2 shows the CMC plot of the same events with spectral estimation performed in the wavelet-transform domain. A Morlet wavelet centred at 24 Hz is used, to capture the frequency band of the highest coherence. One can observe that the wavelet analysis, due to its low time resolution at low frequencies fails to capture significant coherence patterns below 10 Hz.

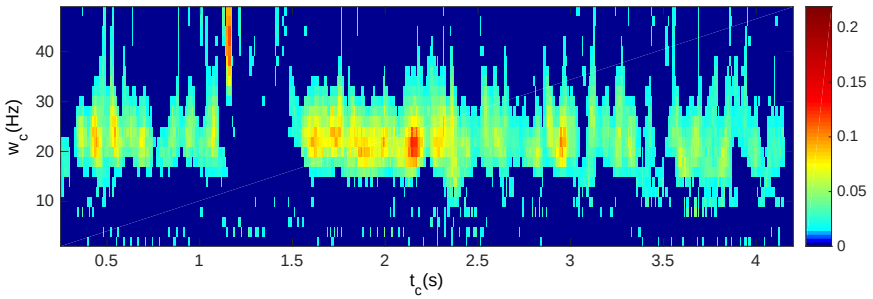

Fig. 2.2 Wavelet coherence using Morlet wavelet centred at 24 Hz.

2.2.2 Factors influencing levels of coherence

The value of coherence is between zero and one. There are several factors that could make CMC so small that the synchrony between EEG and EMG signals would be difficult to detect. One of the factors is the time delay between synchronised events in the brain and the muscle, which can be described as the bias due

to misalignment. The effect of misalignment is best illustrated in the case of two processes $x(t)$ and $y(t)$, one of which is a delayed version of the other,

$$y(t) = bx(t-D) + n(t) \ , \tag{2.15}$$

where $n(t)$ is the additive noise. If the coherence is estimated within an observation window of duration T, the coherence is decreased by a factor, which depends on the ratio between the delay and the duration of the observation window [27]. More specifically

$$E[\hat{C}(\omega)] \approx \left(1 - \frac{|D|}{T}\right)^2 C_{max}(\omega), \qquad |D| \leq T \tag{2.16}$$

where $E[\hat{C}(\omega)]$ is the estimated coherence and $C_{max}(\omega)$ is the maximum coherence without misalignment. The estimated coherence would be maximal when there is no time lag. This dependence of coherence level on temporal alignment of considered processes motivates the cotico-muscular coherence with time lag (CMCTL) analysis and the delay estimation methodology studied in Chapter 4.

Another factor is the noise component, which includes not only the environmental noise but also components unrelated to the process of interest [21]. In movement control, a cortical excitation signal $x_c(t)$ is transmitted to the controlled muscle via multiple paths, each of which has a different delay and attenuation. The corresponding sEMG $y(t)$ is a mixture of the control signal received by the muscle, $y_c(t)$, with noise and various other events unrelated to the considered task. These all combine to produce a signal $n_y(t)$ that will be referred to as noise. The sEMG signal expressed as (2.4) thus has the form

$$y(t) = y_c(t) + n_y(t) \ , \tag{2.17}$$

where $y_c(t) = \sum_{i=1}^{N_x} b_i x_c(t - D_i)$.

Analogously, a synchronously recorded EEG signal $x(t)$ is a mixture of the muscle-control event $x_c(t)$ and a component $n_x(t)$ that is a combination of noise, other cortical events and artefacts. Hence the EEG signal has the form

$$x(t) = x_c(t) + n_x(t) \ . \tag{2.18}$$

If $y_c(t)$ is the response to $x_c(t)$ via an LTI system $B(\omega)$ and both $n_x(t)$ and $n_y(t)$ are independent and zero-mean processes, the coherence between the sEMG and EEG signals at a frequency ω can be shown to have the form

$$C_{xy}(\omega) = \frac{|B(\omega)|^2 S^2_{x_c x_c}(\omega)}{\left(S_{x_c x_c}(\omega) + S_{n_x n_x}(\omega)\right)\left(|B(\omega)|^2 S_{x_c x_c}(\omega) + S_{n_y n_y}(\omega)\right)} \ , \tag{2.19}$$

where $S_{x_c x_c}(\omega)$, $S_{n_x n_x}(\omega)$,$S_{n_y n_y}(\omega)$ are power spectral densities of $x_c(t)$, $n_x(t)$ and $n_y(t)$, and $B(\omega)$ is the frequency response of the propagation channel in (2.17). It can be observed that in the absence of the noise components n_x and n_y the coherence is equal to one. On the other hand, the coherence can be very low if the components x_c and y_c, involved in cortico-muscular interaction, are weak compared to the noise.

2.3 Estimation of Time Delay between EEG and EMG

This section reviews the existing methods for delay estimation, and summarises their drawbacks and limitations when dealing with the motor control system between the cortex and periphery.

Section 2.3.1 briefly outlines the phase model, which has traditionally been considered when estimating the time delay between the brain and the muscle. It

reviews principles of delay estimation based on the analysis of the phase spectrum of EEG-EMG cross-spectral density. In order to solve the problem of cortico-muscular systems where non-linear phase components are present, a modified algorithm based on the Hilbert transform is used. Another method based on maximising coherence is reviewed in Section 2.3.2.

2.3.1 Phase-based estimation

The traditional way of time delay estimation between the cortex and muscle is based on the phase model [5, 7, 16, 28–32]. The cross-spectrum $S_{xy}(\omega)$ can contain complex values and is expressed in the polar form as

$$S_{xy}(\omega) = |S_{xy}(\omega)|e^{j\phi_{xy}(\omega)} , \tag{2.20}$$

where $\phi_{xy}(\omega)$ is the phase angle between the two processes.

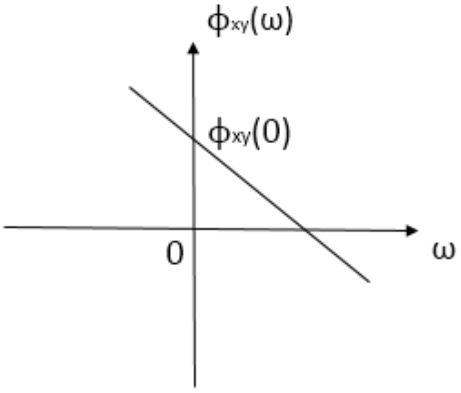

Fig. 2.3 Model of generalised linear phase. The phase $\phi_{xy}(\omega)$ between two processes is a linear function of frequency ω. Corresponding time delay is indicated by the slope of the line.

If $y(t)$ is a delayed and amplitude-scaled version of $x(t)$, $y(t) = bx(t-D)$, x and y are connected via a generalised linear phase system as shown in Fig. 2.3,

where the phase follows a straight line given by the equation

$$\phi_{xy}(\omega) = \phi_{xy}(0) - \omega D \, . \tag{2.21}$$

From here on, the word "generalised" will be omitted when referring to generalised linear phase systems.

Under this model of cortico-muscular signalling pathways, several regression methods have been used so far [82, 83] to estimate the delay between the two processes as the slope of the phase spectrum. However, the slope of a straight line is fitted to the phase spectrum only if the two processes are connected via a linear phase system. In general, the phase function cannot be simply expressed by (2.21) but also contains the argument of the transfer function $A(\omega)$ of the two processes without delay. If the argument of the transfer function $A(\omega)$ is not equal to zero, the phase approach will not be valid [30]. Thus, to ensure that the delay can be calculated from the slope, $A(\omega)$ needs to be estimated in advance or needs to be figured out while estimating the time delay such as done by Lindemann *et al.* who propose estimating the delay from the remaining linear phase component after the nonlinear phase component is identified and removed by using the following Hilbert transform relation [30]

$$\arg A(\omega) = \frac{1}{2\pi} \int_0^{\pi} \log|A(\omega)| \left(\cot \frac{\omega - \theta}{2} + \cot \frac{\omega + \theta}{2} \right) d\theta \, . \tag{2.22}$$

However, this method can only be applied under the assumption that the system satisfies the minimum-phase [84] condition which is rarely seen in practice [30].

In the traditional procedures, the phase estimation is taken in one or several periods which altogether last for a few seconds, during which a number of events could occur. Invariable delay for all the events involved cannot be expected. There

are several pieces of evidence showing that not only can a signal be lead from the cortex to the muscle, but also vice-versa in some circumstances [12, 16, 85]. Thus, if the connection between two processes contains components of opposite directions, the phase spectrum represents a complex combination of both. Unless multidirectional flow is ruled out by a priori information, the temporal relations are ambiguous. The directed transfer function (DTF) in the frequency domain which provides information on the directionality of propagation is used in the situation of bidirectional flow. However, Cassidy and Brown indicate that the DTF provides no advantages in the case of multidirectional interactions [33]. Nevertheless, there is still a motivation for estimating the phase combined with the DTF. That is when the DTF is asymmetric and a clear phase is obtained, a good estimation of delay can be made from the phase spectrum since the flow can be regarded as unidirectional [33].

On a more fundamental level, methods above can be used when the system follows the single-path propagation model. However, the cortico-muscular conduction system, as modelled in (2.4) is not a single-path system. Moreover, since cortical events propagate to muscles via multiple paths, each of which might introduce a different delay, the question that naturally arises is whether this delay is actually well defined, and if so, what it would be, and how to estimate it. These problems are addressed in Chapter 4.

2.3.2 Maximising coherence

Govindan *et al.* proposed estimating the delay as the time offset between EEG and EMG signals which maximises their coherence [39]. In order to realign the time series to compensate for the delay which causes a reduction in coherence, they artificially shifted one of the signals by a lag τ while keeping the other

fixed and then repeated the same operation for the other signal. The maximal coherence in the selected frequency band could be obtained with a certain lag which indicates the time delay between these two signals. However, this method involves Fourier analysis over relatively long segments and rectification of EMG signals, which has recently been challenged by some groups who point out that nonlinear processing generates spurious frequencies [21, 86–88]. Furthermore, it requires the assumption of a continuous constant-delay flow of information in narrow frequency bands, which may make it inapplicable in the case of biological signals such as EEG and EMG. The authors conclude that further work is needed to make the method applicable to nonstationary events.

2.4 Noise Suppression of Biological Signals

The observed sEMG signal, as expressed in (2.17), is composed of the component of interest $y_c(t)$ as well as the noise component $n_y(t)$. The goal of denoising is to recover the unknown signal $y_c(t)$ from the noisy data $y(t)$ by finding a signal $\hat{y}_c(t)$ that approximates $y_c(t)$.

This section presents some key techniques for noise reduction in biological signals and discusses their merits and deficiencies. Section 2.4.1 introduces the multiresolution analysis before describing the methods based on wavelet analysis. Next, the wavelet threshold denoising (WTD) technique is reviewed in Section 2.4.2. In Section 2.4.3, ICA is briefly described, and then the method that takes advantage of both the wavelet analysis and ICA is reviewed in Section 2.4.4. Finally, the dictionary learning and sparse representation problem together with some algorithms to solve it are reviewed in Section 2.4.4.

2.4.1 Multi-resolution analysis

Before reviewing the methods for noise reduction based on wavelet analysis, it is worth introducing the multiresolution analysis which is directly related to the construction of wavelets. A multiresolution analysis of $L^2(\mathbb{R})$ is composed of a nested chain of subspaces, such that

$$0 \cdots \subset V_1 \subset V_0 \subset V_{-1} \subset \cdots \subset V_{-n} \subset V_{-(n+1)} \subset \cdots \subset L^2(\mathbb{R}) \, . \tag{2.23}$$

The subspaces have properties that satisfy regularity relations as well as completeness and certain self-similarity relations [89, 90]. Defining the subspace W_j which is the orthonormal complement of V_j in V_{j-1}, the following relation is seen

$$V_{j-1} = V_j \oplus W_j \, , \tag{2.24}$$

where $\oplus$ denotes the orthogonal sum of subspaces. Therefore, for $j < j_0$, the subspace V_j can be represented as

$$V_j = V_{j_0} \oplus W_{j_0} \oplus W_{j_0-1} \cdots \oplus W_{j+1}. \tag{2.25}$$

The multiresolution structure is shown in Fig. 2.4 as a "dyadic tree" [89]. In the first level, the signal $f(t)$ is decomposed into two parts, one of which consists of low-frequency components for approximation while the other is composed of high-frequency components for detail. Both of them are then subsampled and the low-frequency sub-band which contains most of the energy is split into two parts in the second level. The process can be repeated into K_m levels. The original signal can thus be estimated by the sum of the approximation and detail at the current level, as well as the details at all the lower levels.

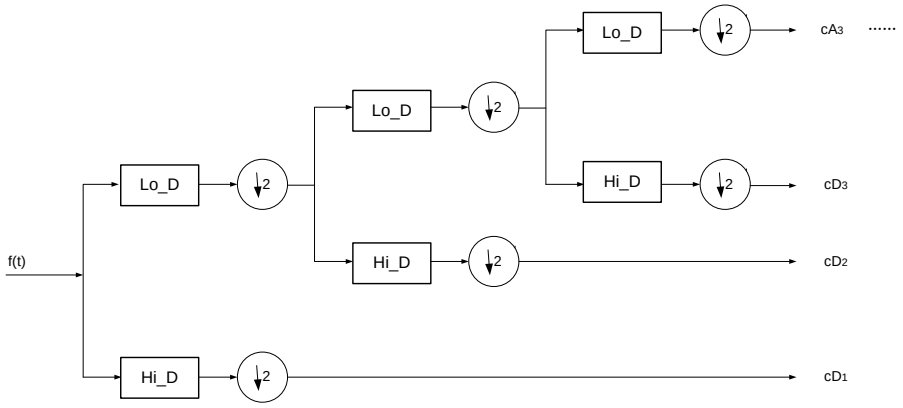

Fig. 2.4 Multiresolution structure shown as "dyadic tree". *Lo_D* and *Hi_D* represent low-pass and high-pass filters, respectively. Both the low-frequency and high-frequency components are subsampled.

Associated with wavelets, the scaling basis $\{\varphi_{j,k};\ k \in \mathbb{Z}\}$ and the wavelet basis $\{\psi_{j,k};\ k \in \mathbb{Z}\}$ form the orthonormal basis of the subspaces V_j and W_j, respectively. Wavelet expansion of a signal is a combination of the scaling basis functions $\varphi_{j_0,k}(t)$ and the wavelet basis functions $\psi_{j,k}(t)$ as

$$f(t) = \sum_k c_{j_0,k}\varphi_{j_0,k}(t) + \sum_{j \le j_0}\sum_k d_{j,k}\psi_{j,k}(t)\ , \tag{2.26}$$

where $c_{j_0,k}$ is the projection of $f(t)$ on the scaling basis $\varphi_{j_0,k}$ such that

$$c_{j_0,k} = \int f(t)\varphi^*_{j_0,k}(t)dt\ , \tag{2.27}$$

while $d_{j,k}$ is the projection of $f(t)$ on the wavelet basis $\psi_{j,k}$ such that

$$d_{j,k} = \int f(t)\psi^*_{j,k}(t)dt \ . \tag{2.28}$$

The first item on the right side of (2.26) is defined as the low-resolution approximation and the second item is the linear sum of all the wavelet details.

2.4.2 Wavelet threshold denoising

Wavelet threshold denoising (WTD) is one of the standard techniques for denoising of biological signals, and will be considered in this study as a reference method. The method first involves finding a wavelet expansion of a signal, followed by the thresholding of expansion coefficients. The thresholding effectively removes some of the noise from wavelet coefficients, and the signal is then synthesised from the denoised coefficients.

There are two rules of thresholding to achieve shrinkage, one of which is the hard thresholding and the other is the soft thresholding. The hard thresholding is specified by the following function

$$\eta_H(x) = \begin{cases} x, & \text{if } |x| > \Theta \\ 0, & \text{otherwise} \end{cases} \tag{2.29}$$

while the soft thresholding rule is given by

$$\eta_S(x) = \text{sgn}(x)(|x| - \Theta)_+ \ , \tag{2.30}$$

where Θ is the threshold, $\mathrm{sgn}(\cdot)$ is the sign function and $(|x|-\Theta)_+ = |x|-\Theta$, if $|x|-\Theta \geq 0$, otherwise $(|x|-\Theta)_+ = 0$ [91, 92]. Fig. 2.5 shows an example of hard and soft thresholding when $\Theta = 0.5$.

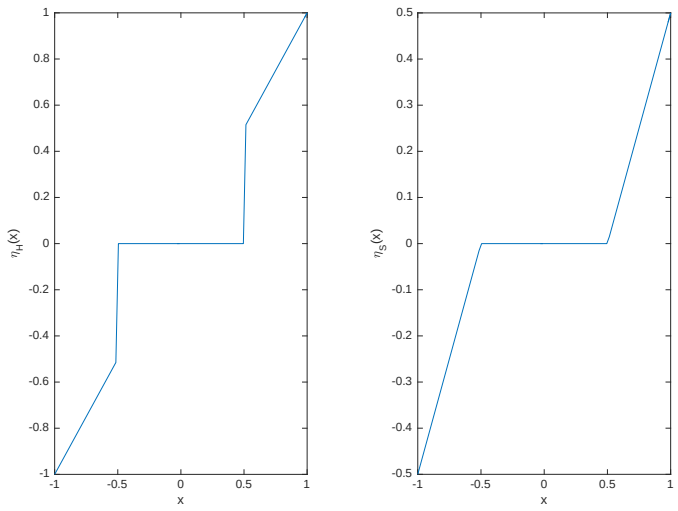

(a) (b)

Fig. 2.5 Two typical threshold operators for denoising. (a) Hard thresholding. (b) Soft thresholding.

The WTD technique is capable of removing some background noise and some Gaussian white noise from EEG and sEMG signals. However, it may not be effective in removing some of the components unrelated to the control process of interest.

2.4.3 Independent component analysis

Independent component analysis (ICA) is a technique for separating independent source signals $\mathbf{q}_j,\ j = 1,\ldots,N_\mathrm{s}$ from their linear mixtures $\mathbf{x}_i,\ i = 1,\ldots,N_\mathrm{mix}$ which

can be described as

$$\mathbf{x}_i = \sum_{j=1}^{N_s} a_{ij}\mathbf{q}_j, \tag{2.31}$$

where a_{ij} is the (i,j)th entry of $N_{\text{mix}} \times N_s$ mixing matrix $\mathbf{A}$ and the noise terms are contained in the source signals $\mathbf{q}_j$. The mixing representation can be expressed in matrix form as

$$\mathbf{X} = \mathbf{AQ}, \tag{2.32}$$

where $\mathbf{X} = [\mathbf{x}_1\ \mathbf{x}_2\ \ldots\ \mathbf{x}_{N_{\text{mix}}}]^T$, $\mathbf{Q} = [\mathbf{q}_1\ \mathbf{q}_2\ \ldots\ \mathbf{q}_{N_s}]^T$. The superscript T indicates the transpose [93]. ICA amounts to finding the inverse matrix $\mathbf{W} = \mathbf{A}^{-1}$ by making the demixed components of $\mathbf{Q}$ maximally independent. The estimated source signals $\hat{\mathbf{Q}}$ can then be derived as

$$\hat{\mathbf{Q}} = \hat{\mathbf{W}}\mathbf{X}\ , \tag{2.33}$$

where $\hat{\mathbf{W}}$ is the estimated demixing matrix. According to the Central Limit Theorem which states that a sum of independent random variables tends to have a distribution that is closer to Gaussian distribution than any of the original random variables and in order to make the components of $\mathbf{Q}$ maximally independent, the non-Gaussianity of $\mathbf{Q}$ must be maximised [93]. Independence can also be measured by the mutual information [94] and the maximum likelihood estimation[95]. However, the mutual information is difficult to evaluate. In addition, the maximum likelihood estimation criterion may produce wrong results in practice [93].

There are several ways to measure non-Gaussianity. The classical way is to use kurtosis, but it is not robust. Another important measure of non-Gaussianity is by negentropy. However, its estimation is difficult. In practice, some approximations of negentropy are proposed to be used for ICA. Thus, finding the inverse of the

mixing matrix that maximises the non-Gaussianity of **Q** is roughly equivalent to finding directions in which the approximation of negentropy is maximised. It is worth noting that to simplify the estimation, the observed variables should be centred (zero-mean) and with the variances equal to unity. Therefore, it is useful to do some pre-processing for centring and whitening.

Exemplary ICA applications on EEG and sEMG signals include the decomposition of sEMG for gesture identification [96, 97], muscle fatigue synchronisation of sEMG [98, 99], and demonstrating the coupling between sEMG and EEG [100].

In order to have the mixing matrix **A** of full rank for its inverse to exist, the number of observed mixtures N_{mix} must be at least as large as the number of estimated components N_{s}. Hence, when the number of channels is insufficient, ICA might not be able to separate the sources. However, in order to minimise the costs which include the costs of equipments, the time spent on placing electrodes for data collection as well as the simplification of the operation prior to and during signal collection, the consideration regarding data acquisition using a small number of channels is necessary.

2.4.4 Wavelet independent component analysis

To overcome the limitations imposed on ICA in the context of low-channel count data acquisition, some previous work introduced to use wavelet-independent component analysis (WICA) which investigated applying wavelet decomposition prior to ICA to generate wavelet components (WCs) for increasing the effective number of mixtures [50–53, 55, 101]. The method based on the joint use of discrete wavelet transform (DWT) and ICA for artefact removal in biomedical signals was first proposed by Azzerboni *et al.* [101] to overcome the limitations and encompass the advantages of both techniques.

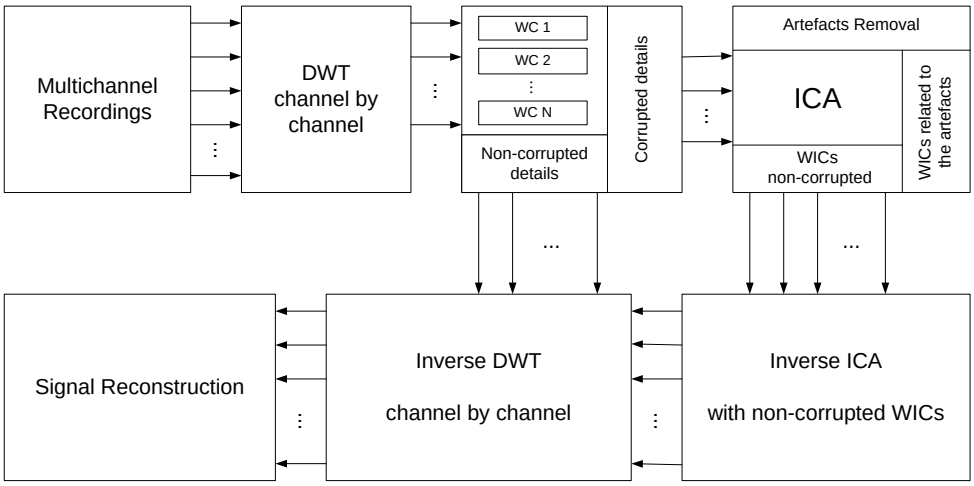

Fig. 2.6 Block diagram of WICA for artefact removal.

The main procedures of WICA are illustrated by the block diagram shown in Fig. 2.6. Firstly, DWT is applied to each channel of data separately. Secondly, only the WCs which contain artefacts are selected to which ICA is applied. After applying ICA, wavelet independent components (WICs) are estimated and those related to the artefacts are removed. Finally, signal reconstruction is performed and the denoised multichannel signals are obtained [101].

2.4.5 Dictionary learning and sparse representation

The aim of dictionary learning and sparse signal representation is to find a sparse representation of the observed signal which can express almost all useful information within the signal. They have been widely applied in the fields of audio, image and video processing. The analysis of sparse representation has been used for biological signal processing as well [58–61].

Given the observed dataset $\mathbf{R} = [\mathbf{r}_1\ \mathbf{r}_2\ ...\ \mathbf{r}_m]$, $\mathbf{r}_i \in \mathbb{R}^n$, we intend to find both a dictionary $\mathbf{D} \in \mathbb{R}^{n \times K}$, which consists of K atoms for columns such that $\mathbf{D} = [\mathbf{d}_1\ \mathbf{d}_2\ ...\ \mathbf{d}_K]$, and a sparse representation $\mathbf{S} = [\mathbf{s}_1\ \mathbf{s}_2\ ...\ \mathbf{s}_m]$, $\mathbf{s}_i \in \mathbb{R}^K$ subject to $\| \mathbf{R} - \mathbf{DS} \|_F^2 \leq \varepsilon$, where $\| \cdot \|_F$ indicates the Frobenius norm. This can be achieved by finding a dictionary $\mathbf{D}$ and a representation $\mathbf{S}$ to solve the following optimisation problem

$$\arg \min_{\mathbf{D},\mathbf{s}_i} \left\{ \sum_{i=1}^{m} \left\{ \| \mathbf{r}_i - \mathbf{D}\mathbf{s}_i \|_2^2 + \lambda \| \mathbf{s}_i \|_0 \right\} \right\}. \tag{2.34}$$

The ℓ_1-norm can be used to measure sparsity [102] instead of the ℓ_0-norm in order to make this optimisation problem convex with respect to each of the dictionary $\mathbf{D}$ and the sparse coding $\mathbf{S}$ when the other one is fixed. The problem above thus becomes

$$\arg \min_{\mathbf{D},\mathbf{s}_i} \left\{ \sum_{i=1}^{m} \left\{ \| \mathbf{r}_i - \mathbf{D}\mathbf{s}_i \|_2^2 + \lambda \| \mathbf{s}_i \|_1 \right\} \right\}. \tag{2.35}$$

Most of the proposed algorithms for solving this problem are based on the idea of alternating between the two variables so that they iteratively update one while keeping the other fixed before turning to the other.

One of the most popular methods to solve this problem named the method of optimal directions (MOD) was proposed by Engan *et al.* [103]. The MOD sets an initialised $\mathbf{D}$ to get the sparse coding by finding the solution of (2.34) using a pursuit such as the orthogonal matching pursuit (OMP). Then it updates $\mathbf{D}$ by using the Moore-Penrose pseudoinverse of the sparse coding, $\mathbf{S}^+$, to solve the problem of minimum ℓ_2 norm, so that $\mathbf{D} = \mathbf{R}\mathbf{S}^+$. The dictionary $\mathbf{D}$ is renormalised before updating the sparse coding again. The process is repeated until the residue is sufficiently small.

Another very popular method is the K-SVD method, which was first presented by Aharon *et al.* [104]. As its name implies, the core of it involves both the

K-means algorithm and singular value decomposition (SVD). Specifically, the sparse coding stage is identical to that of the MOD, but during the dictionary update stage, each column of $\mathbf{D}$ is processed one by one with the corresponding row of $\mathbf{S}$. The error matrix for all the m examples when the gth atom is removed is computed by

$$\mathbf{E}_g = \mathbf{R} - \sum_{j \neq g} \mathbf{d}_j \mathbf{s}^j \,, \tag{2.36}$$

where $\mathbf{s}^j$ denotes the jth row in $\mathbf{S}$. In order to enforce the sparsity constraint in the update of $\mathbf{d}_g$, $\mathbf{E}_g$ is restricted to $\mathbf{E}_g^R$ by keeping columns i where $\mathbf{s}^g(i) \neq 0$. SVD is then applied to $\mathbf{E}_g^R$ so that

$$\begin{aligned} \mathbf{E}_g^R &= \mathbf{U}\Delta\mathbf{V}^T \\ &= \begin{bmatrix} u_{11} & u_{12} & \cdots & u_{1n} \\ u_{21} & u_{22} & \cdots & u_{2n} \\ \vdots & \vdots & \ddots & \vdots \\ u_{n1} & u_{n2} & \cdots & u_{nn} \end{bmatrix} \times \begin{bmatrix} \delta_{11} \cdot v_{11} & \delta_{11} \cdot v_{21} & \cdots & \delta_{11} \cdot v_{h1} \\ \delta_{22} \cdot v_{12} & \delta_{22} \cdot v_{22} & \cdots & \delta_{22} \cdot v_{h2} \\ \vdots & \vdots & \ddots & \vdots \end{bmatrix} , \end{aligned} \tag{2.37}$$

where h is the total number of columns of $\mathbf{E}_g^R$. The first column of $\mathbf{U}$ is defined as the updated dictionary column $\tilde{\mathbf{d}}_g = [u_{11}\ u_{21} \cdots u_{n1}]^T$ while the first column of $\mathbf{V}$ multiplied by $\Delta(1,1)$ is defined as the coefficient vector $\mathbf{s}^g = \delta_{11} \cdot [v_{11}\ v_{21} \cdots v_{h1}]$.

When the dictionary $\mathbf{D}$ is known, Alternating Direction Method of Multipliers (ADMM) which combines the benefits of both augmented Lagrangian and dual decomposition methods [105] is used to obtain higher accuracy of the sparse representation. The ADMM algorithm was designed for the following problem

$$\begin{aligned} &\min \left\{ f(\mathbf{x}) + g(\mathbf{z}) \right\} \\ &\text{subject to } \mathbf{A}\mathbf{x} + \mathbf{B}\mathbf{z} = \mathbf{c} \,, \end{aligned} \tag{2.38}$$

where $f(\cdot)$ and $g(\cdot)$ are convex, $\mathbf{x} \in \mathbb{R}^p$, $\mathbf{z} \in \mathbb{R}^q$, $\mathbf{A} \in \mathbb{R}^{l \times p}$, $\mathbf{B} \in \mathbb{R}^{l \times q}$, and $\mathbf{c} \in \mathbb{R}^l$. The augmented Lagrangian for (2.38) is

$$L_\rho(\mathbf{x}, \mathbf{z}, \beta) = f(\mathbf{x}) + g(\mathbf{z}) + \beta^T(\mathbf{A}\mathbf{x} + \mathbf{B}\mathbf{z} - \mathbf{c}) + (\rho/2)\|\mathbf{A}\mathbf{x} + \mathbf{B}\mathbf{z} - \mathbf{c}\|_2^2 \,, \quad (2.39)$$

where β is called the dual variable or the Lagrange multiplier and $\rho > 0$ [105]. The ADMM consists of two separate minimisation steps and a multiplier update. Explicitly, the algorithm does the following updates iteratively

$$\begin{aligned} \mathbf{x}^{k+1} &:= \arg \min_{\mathbf{x}} L_\rho(\mathbf{x}, \mathbf{z}^k, \beta^k) \\ \mathbf{z}^{k+1} &:= \arg \min_{\mathbf{z}} L_\rho(\mathbf{x}^{k+1}, \mathbf{z}, \beta^k) \\ \beta^{k+1} &:= \beta^k + \rho(\mathbf{A}\mathbf{x}^{k+1} + \mathbf{B}\mathbf{z}^{k+1} - \mathbf{c}) \,. \end{aligned} \quad (2.40)$$

Comparing to the augmented Lagrangian method, the ADMM has the important advantage that it does not involve a joint minimisation with respect to $\mathbf{x}$ and $\mathbf{z}$ [105].

2.5 Conclusions

This chapter first introduced a simplified model of motor control system, which was causal, FIR and LTI. The forms of sEMG and EEG signals considering bidirectional signalling were also presented.

Section 2.2 reviewed relevant aspects of coherence analysis. TFA by the means of STFT and WT was described. EEG and EMG signals collected during a controlled motor task which is presented in Chapter 3 were then used to illustrate the effects of different time-frequency resolutions on the information revealed

by the coherence analysis. Section 2.2 also discussed two primary factors that could influence the level of CMC and make its value so small that the synchrony between EEG and EMG would be difficult or even impossible to detect.

Section 2.3 reviewed the traditional and the state-of-the-art methods for the estimation of time delay between EEG and EMG, which is one of the factors that influence CMC levels. In addition, drawbacks and limitations of these methods in the context of underlying physiology and properties of the cortico-muscular conduction system were discussed. A novel method for delay estimation by CMCTL is proposed in Chapter 4.

As an introduction to novel methods for extracting cortico-muscular signals involved in muscle control from EEG and sEMG signals, proposed in Chapter 5, state of the art methods for noise suppression in biological signals were reviewed in Section 2.4. In particular, the WTD technique was discussed, along with its limitation in the context of CMC analysis. Then the WICA was discussed. Finally, a brief overview of methods of dictionary learning and sparse signal representation was given, which is used in Chapter 5 as the basis of a novel algorithm for the extraction of synchronous components from EEG and sEMG signals.

Chapter 3

DATA ACQUISITION

The aim of this study is to develop a set of advanced signal processing tools which can be applied to EEG and EMG signals recorded simultaneously and non-invasively during particular movement tasks, in order to more precisely characterise the underlying cortico-muscular interactions. Therefore, a designed experiment is needed for data collection. Towards unravelling general principles of movement control, signals collected from healthy volunteers are used. The data are used in the research on time delay estimation and coherent component extraction. The methodologies proposed in Chapter 4 and Chapter 5 are assessed using the data collected in the experiment presented in this chapter.

3.1 Introduction

EEG and EMG signals were collected during a controlled motor task [13]. In Section 3.2, the general experimental arrangement is introduced. The motor task is described in detail. Section 3.2 also presents the positions of EEG and EMG electrodes as well as the pre-processing of the data for further study. Section 3.3

gives the reason as to why a specific window has been chosen and demonstrates the coherence analysis with the signals collected from the motor task. Further considerations are presented in Section 3.4.

3.2 Experiment

3.2.1 General experimental arrangement

Subjects sit comfortably at a table and perform a simple motor task with their right hand holding a 15 cm plastic ruler in a key grip between the thumb and index finger with 2 cm of the end of the ruler grasped, keeping the ruler parallel to and 2 cm above the table surface. In order to minimise contraction of other muscles and fatigue, the wrist and forearm are supported. Mechanical perturbations to the motor task are provided from an electromechanical tapper that generates pulses of lateral displacement of the ruler, giving the subjects the sensation that their grip on the ruler may be lost. The subjects are asked to hold the ruler gently against the stylus of the tapper to maintain its position as well as they can throughout each run. The stylus of the tapper is placed halfway along the length of the ruler and perpendicular to it. Fig. 3.1(a) shows the positions of tapper, ruler and hand. The perturbation lasts for a total duration of 20 ms with 5 ms as the rise time. The lateral displacement of the tapper against the ruler is 1 mm with a velocity of 0.2 m/s while the angular displacement at the grip point is at 0.76 degrees.

A single trial lasts 5 seconds, with the stimulus delivered 1.1 s after the start of the data collection period. The stimuli are delivered at pseudorandom intervals varying between 5.6 s and 8.4 s (mean 7.0 s) so that subjects cannot anticipate the

arrival of the next stimulus. Data are collected in blocks of 25 trials (data epochs) with a short rest between blocks, to avoid fatigue. Up to 8 blocks of data (200 trials) are collected for each subject.

The muscle pair, first dorsal interosseous (FDI) and flexor pollicis brevis (FPB), is predominantly activated during this task. Throughout the study, the subjects are observed by the experimenter carefully so as to ensure that they maintain the position of the ruler.

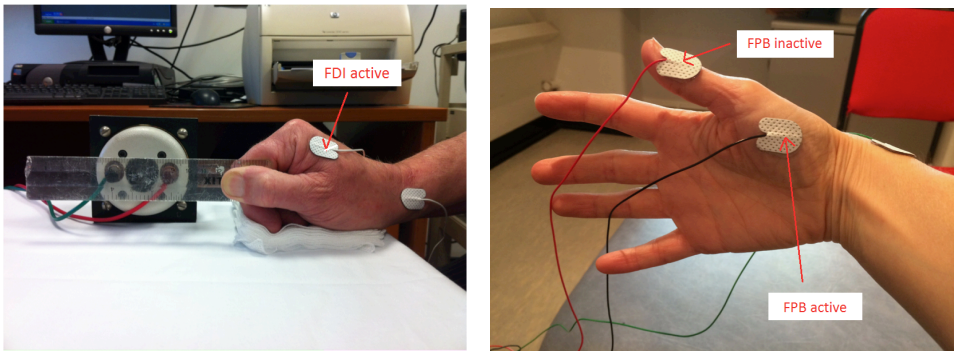

(a) (b)

Fig. 3.1 Photographs of the experiment. (a) Positions of the tapper, ruler, hand and FDI active (muscle belly) electrode. The FDI inactive (tendon) electrode is placed on the side of the index finger which cannot be seen in this photo. (b) Positions of the FPB active (muscle belly) and inactive (tendon) electrodes.

3.2.2 EEG and EMG recording and data pre-processing

Bipolar EEG is recorded from the scalp overlying the contralateral motor cortex using an electrode which is placed 5 cm lateral to the vertex along the interaural line, and the other electrode is positioned 2.5 cm anterior to it (see Fig. 3.2). There is also an earth electrode positioned in the midline of the forehead. Conductive paste is used to apply these electrodes to the scalp and skin preparation is performed to reduce the electrode impedance below 5 kOhm. EMG is recorded using adhesive electrodes in a belly-tendon montage over FDI and FPB of the dominant hand (see

Fig. 3.1). EMG and EEG signals are amplified and bandpass filtered (0.5 – 100 Hz for EEG; 5 – 500 Hz for EMG). Signals are passed to a digital converter and sampled at 1024 Hz. Raw EEG signals are scrutinised off-line by eye and any epochs of data containing movement artefacts are rejected from further analysis, *i.e.* the whole data epochs which also include the epochs of corresponding EMG signals are excluded. The power line noise is removed by a digital notch filter. The raw data for one trial corresponding to subject J are shown as an example in Fig. 3.3.

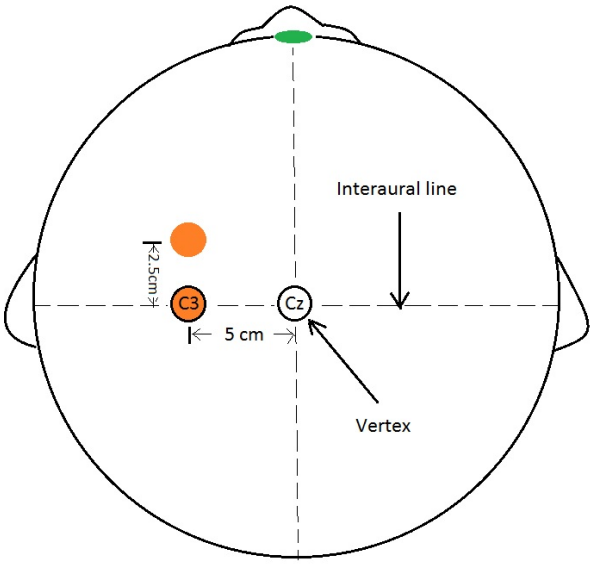

Fig. 3.2 Positions of EEG electrodes. The bipolar EEG is recorded using two electrodes shown as orange dots and an earth electrode is placed on the midline of the forehead shown as green dot.

For the original neurophysiology study [13], 12 healthy right-handed subjects are recruited. The coherence observed in a majority of subjects is however very weak. One such instance of weak coherence is illustrated in Fig. 4.9 in Chapter 4. It can be noted that except in a short interval immediately following the stimulus the coherence is weak and, moreover, the time-frequency region where the CMC

is present is very sparse. For the development and validation of the methodologies presented in this study, 5 subjects with pronounced coherence patterns, such as the one illustrated in Fig. 2.1, therefore are taken into main consideration.

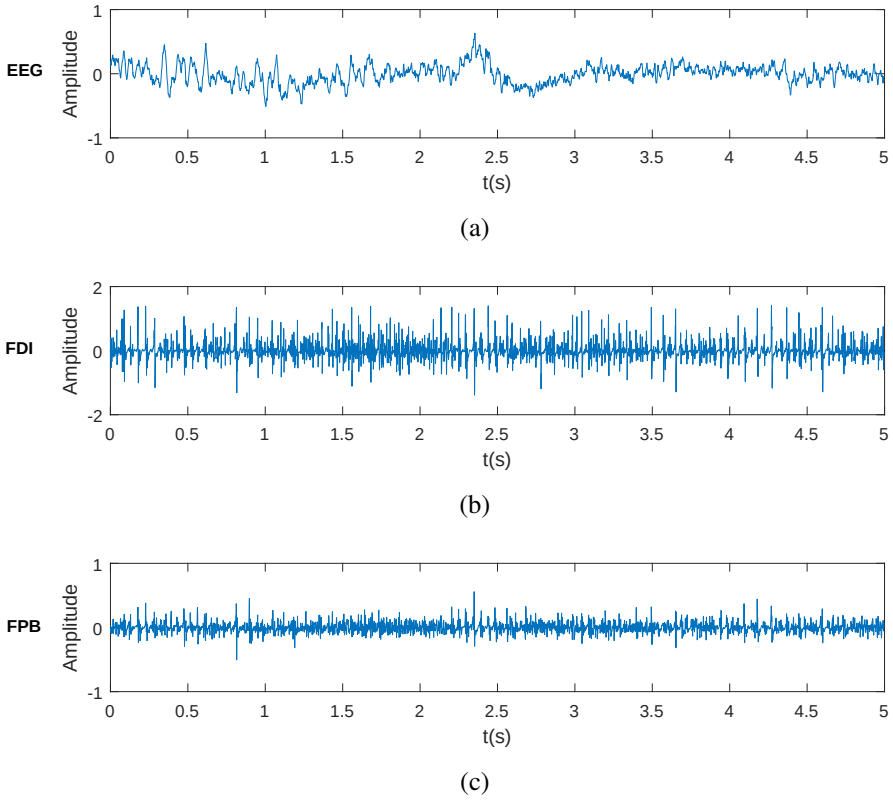

Fig. 3.3 Raw data recorded during the motor control task for one trial. (a) EEG. (b) FDI. (c) FPB.

3.3 Coherence Analysis

Signals collected in the experiment are analysed using STFT and WT with time-frequency resolutions described in Chapter 2, as illustrated in Fig. 2.1 for signals corresponding to subject J. The STFT using Hanning window of length $T = 125$ ms, with time shifts of $\Delta t = 9.8$ ms between consecutive analysis windows (Fig. 2.1(c)) provides the most suitable time-frequency resolution in terms of the ability

to discriminate between consecutive transient events without a considerable drop in coherence levels and it will be used in all experiments reported in this and subsequent chapters.

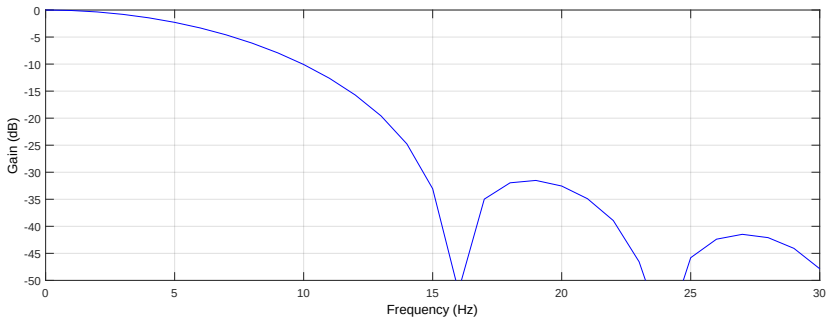

Fig. 3.4 Magnitude response (dB) of Hanning window of length 125 ms when sampling frequency is 1024 Hz. The 3 dB bandwidth of it is about 11 Hz.

The CMC is observed primarily within the β range, $13-36$ Hz, in this study, which is in keeping with other reports of similar low level contraction tasks [10, 16, 36]. Therefore, when developing the methods and considering the choice of windows, it has to be taken into account that β range is the main frequency range of interest. Fig. 3.4 shows the magnitude response of the Hanning window of length $T = 125$ ms, of which the main lobe width (as defined by a 3 dB corner) is about 11 Hz. Although the peak frequency is within the β range, it varies between subjects [13]. In terms of the central position which is at theses different peak frequencies, Hanning window of length $T = 125$ ms can cover most of the central β band. CMC corresponding to subject J at its peak frequency 24 Hz and CMC corresponding to subject L at its peak frequency 16 Hz obtained using Hanning window of length $T = 125$ ms, with $\Delta t = 9.8$ ms are shown in Fig. 3.5. CMC in Fig. 3.5 is calculated following (2.12), where the number of trials is 194 for subject J and 163 for subject L. Fig. 3.5 illustrates that the coherence does not always keep significant during the estimated period even at its peak frequency.

Especially in Fig. 3.5(b), the coherence drops under the significant level every very short time. It could result from that the motor cortex and the muscle might not exhibit synchronous behaviour constantly. The estimation of the peak frequency of coherence of each subject and further analysis with respect to the coherence peaks are presented in Chapter 4.

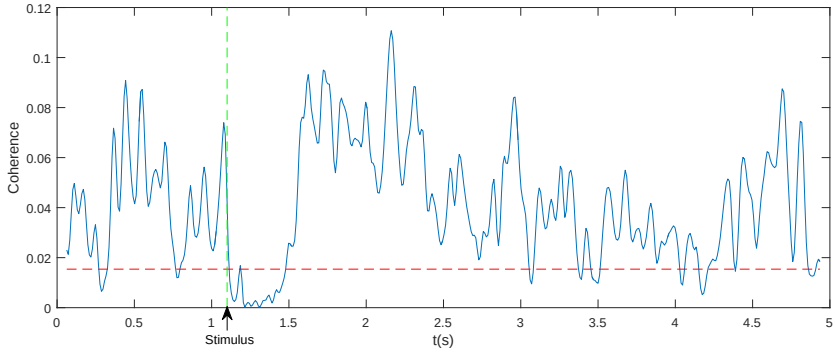

(a)

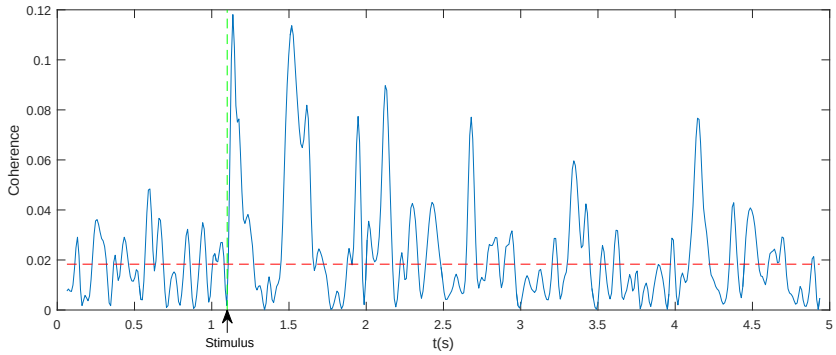

(b)

Fig. 3.5 CMC at peak frequency obtained using Hanning window of length $T = 125$ ms, with $\Delta t = 9.8$ ms. The dashed red line indicates the 95% confidence limit and the dashed green line indicates the time instant when the stimulus was delivered during each trial. (a) CMC at 24 Hz corresponding to subject J. (b) CMC at 16 Hz corresponding to subject L.

The whole period could be separated by the time instant, at which the stimulus is delivered, into two periods: pre- and post-stimulus periods. There are subjects who show just a little or no significant β-range CMC in the pre-stimulus period, but post-stimulus increases their CMC in β range (see Fig. 3.6). Fig. 3.6 is

obtained using the same STFT parameters as those used for Fig. 3.5. This is in agreement with some previous works which support the hypothesis that under the optimised circumstances, all individuals may actually present β-range CMC [11, 13, 17].

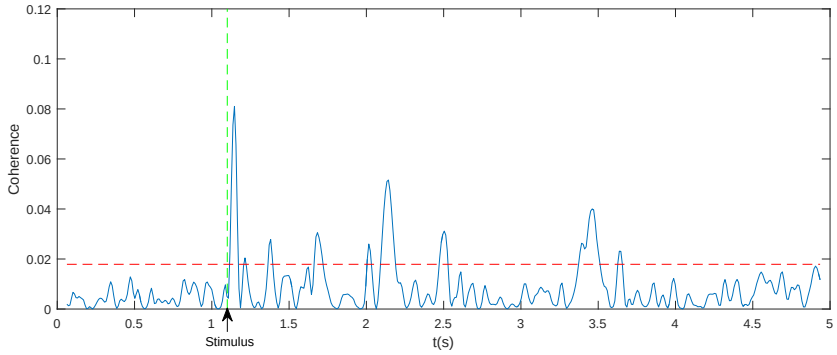

Fig. 3.6 CMC at 24 Hz corresponding to subject G obtained using Hanning window of length $T = 125$ ms, with $\Delta t = 9.8$ ms. The dashed red line indicates the 95% confidence limit and the dashed green line indicates the time instant when the stimulus was delivered during each trial.

It is worth noting that significant coherence in the β range disappears in the immediate post-stimulus period and reappears soon after 1.5 s. In addition, there is a burst of α-range ($8-13$ Hz) coherence in the immediate post-stimulus period. It could be caused by the artefacts related to a rapid movement of the ruler and the associated reflexes in muscle and brain, which requires further study.

3.4 Further Considerations

Since the immediate post-stimulus period shows some results which are difficult to interpret, this period is excluded from further estimation. To investigate the nature of the changes in coherence that is observed during this period, some other experiments with slow change should be considered in future research so as to avoid the effect caused by the artefacts related to the fast movement.

3.5 Conclusions

This chapter introduced the motor control task, during which EEG and EMG signals were collected. The experiment was designed, including the design of general experimental arrangements and considerations of EEG and EMG recordings, stimulation protocols and data pre-processing. EEG and EMG signals were then used for further study.

As indicated in Section 3.3, the STFT was used in the analysis of CMC in this study and the window for it was chosen by considering the suitable time-frequency resolution in terms of the trade-off between the coherence levels and discrimination between consecutive transient events. The main frequency range of interest regarding this experimental paradigm was the β range. However, during a period right after the stimulus was delivered, the coherence disappeared around the β range but appeared prevalently in the α range. Since it could be caused by the artefacts with respect to rapid movement, some other experiments need to be considered. Nevertheless, the estimation in Chapter 4 and Chapter 5 is mainly carried out with this period being excluded.

The developed approaches that are presented in Chapter 4 and Chapter 5 are applied to the data recorded in the experiment described in this chapter. The mechanical perturbation provided a functionally relevant peripheral input to the system, which caused a significant increase of the β-range CMC. Therefore, when developing the methods, the β range is considered as the main frequency range of interest. The CMCTL proposed in Chapter 4 investigates the changes and temporal structures of cortico-muscular interactions after the stimulus, and is compared to conventional CMC. Delay estimation and noise removal is studied using the simultaneously recorded EEG and EMG signals. The developed methods focus on

the post-stimulus period, especially the segments around two particular coherence peaks. One of the peaks is within a short time, around 1 s, after the mechanical stimulus, and the other appears after a longer period time, around 2 s. In this manner, the performance of developed algorithms under different situations, taking the influence of possible bidirectional signalling and stabilisation of movement control into account, can then be compared.

For each subject, all trials of data excluding those containing movement artefacts which were rejected as mentioned in Section 3.2.2 are used for the proposed algorithms in Chapter 4 and Chapter 5. The number of used trials ranges from 164 to 200, which is within the range of trials that is sufficient to avoid spurious coherence spectra, to stabilise the value of coherence [106].

Chapter 4

CORTICO-MUSCULAR COHERENCE WITH TIME LAG

Functional coupling between the motor cortex and muscle activity is usually detected and characterised using the spectral method of CMC. This functional coupling occurs with a time delay, which, if is not properly accounted for, may decrease the coherence and make the synchrony difficult to detect. Therefore, in this chapter, an approach for delay estimation between the motor cortex and the periphery is developed. This method is applied to the neurophysiological data collected in the experimental controlled motor task presented in Section 3.2.

4.1 Introduction

The time delay between coupled EEG and EMG signals is one of the factors that could decrease the level of coherence, whereby compensating for the delay could result in CMC enhancement. Moreover, the estimation of the time delay between the motor cortex and the periphery is of great importance because it

provides understanding on the direction of information propagation and helps differentiate the cortico-spinal pathways of the transmission in considered events. However, the delay estimation is very challenging. Several methods for delay estimation were reviewed in Chapter 2, which include the methods based on the phase of the cross spectral density of considered processes as well as another technique which estimates the delay as the time offset between EEG and EMG signals that maximises their coherence. In addition, the issues that could make those methods lead to erroneous results were discussed. In this Chapter, a novel method is proposed for estimating the delay between coupled EEG and EMG events based on local maxima of the cortico-muscular coherence with time lag (CMCTL).

This chapter is organised as follows. Section 4.2 outlines the CMCTL and the method for the delay estimation. Section 4.3 presents examples of CMCTL applied to physiological data and results of delay estimation. Finally, further considerations concerning healthy subjects which do not express significant CMC are given in Section 4.4.

4.2 Methods

In this section, a method to estimate the time delay between EEG and EMG is proposed. Section 4.2.1 derives the CMCTL from conventional CMC. In Section 4.2.2, first, the notion of the global delay is introduced to define the delay over multiple paths. Next, the method of the global delay estimation by using CMCTL is described in detail. Section 4.2.3 presents the physical interpretation of the global delay.

4.2.1 Cortico-muscular coherence with time lag

Towards achieving time alignment between EEG and EMG events, we propose to consider coherence between their versions shifted in time. Two additional variables corresponding to the displacements of EEG and EMG in the short-time Fourier based coherence (2.12) are introduced. In particular, the following CMCTL function is proposed

$$C_{xy}(t_c, \tau_1, \tau_2, \omega) = \frac{|\hat{S}_{xy}(t_c + \tau_1, t_c + \tau_2, \omega)|^2}{\hat{S}_{xx}(t_c + \tau_1, \omega)\hat{S}_{yy}(t_c + \tau_2, \omega)} \tag{4.1}$$

where t_c is the reference observation time instant, while τ_1 and τ_2 are displacements of $x(t)$ and $y(t)$ observations, respectively, from that reference point. Hence, the observation windows for $x(t)$ and $y(t)$ are centred at $t_c + \tau_1$ and $t_c + \tau_2$, respectively. In this manner the compensated time delay between these two processes is $\tau = \tau_2 - \tau_1$.

There are several points regarding CMCTL that are worth noting:

1) Cortico-muscular processes are not stationary and often involve transient events which could be much shorter than the window of the underlying STFA. Consequently, the fact that two pairs of displacements (τ_1, τ_2) and (τ_1', τ_2') satisfy $\tau_2 - \tau_1 = \tau_2' - \tau_1'$ does not imply that $C_{xy}(t_c, \tau_1, \tau_2, \omega) = C_{xy}(t_c, \tau_1', \tau_2', \omega)$.

2) Apparently, one of the CMCTL time variables, t_c, τ_1, and τ_2, is redundant, however, having all of them explicitly makes the CMCTL function easier to read.

3) A convenient way to visualise the CMCTL function is by plotting it in the (τ_1, τ_2) plane for a pair of fixed (t_c, ω_c) parameters. Fig. 4.1(a) shows an

example of the conventional CMC plot with two prominent peaks marked by $\times$ signs, while Fig. 4.1(b) shows the CMCTL plotted for fixed $t_c = 3.441$ s and $\omega_c = 24$ Hz which are the coordinates of the second prominent peak (the second peak is considered here just as an illustration, whereas both peaks are discussed in Section 4.3). The sampling frequency of data acquisition is $\Omega_s = 1024$ Hz, while the STFT is evaluated at $N = 128$ frequencies using the $T = 125$ ms Hanning window (128 samples). Each point on this plot thus reflects events situated within the corresponding 125 ms interval, and within the 11 Hz frequency band (the bandwidth of the window) centred around 24 Hz.

4) Whereas t_c is not explicitly represented on CMCTL plots centred around a fixed (t_c, ω_c) pair, it evolves along the line $\tau_1 = \tau_2$. Hence, the conventional CMC is given by a sequence of regular samples of CMCTL along this line.

Fig. 4.1 illustrates benefits of the CMCTL compared to the conventional CMC, in terms of either enhancing the coherence or providing additional insights. In particular:

1) The coherence maxima do not occur along the line $\tau_1 = \tau_2$, but are seen at points away from this line.

2) All local coherence peaks are on the same side of the line $\tau_1 = \tau_2$, suggesting signalling in the same direction; this information is absent from the conventional CMC.

3) The duration of cortico-muscular coupling events is always longer if considered along the line of their maximal coherence as opposed to the the line $\tau_1 = \tau_2$.

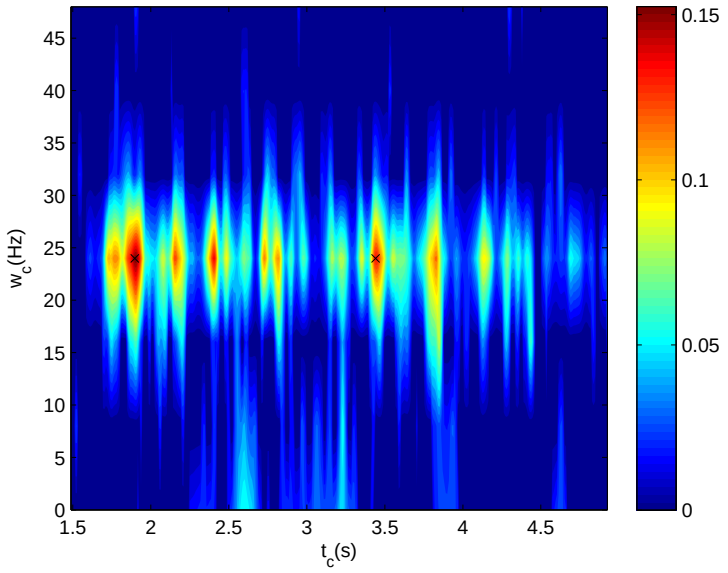

(a)

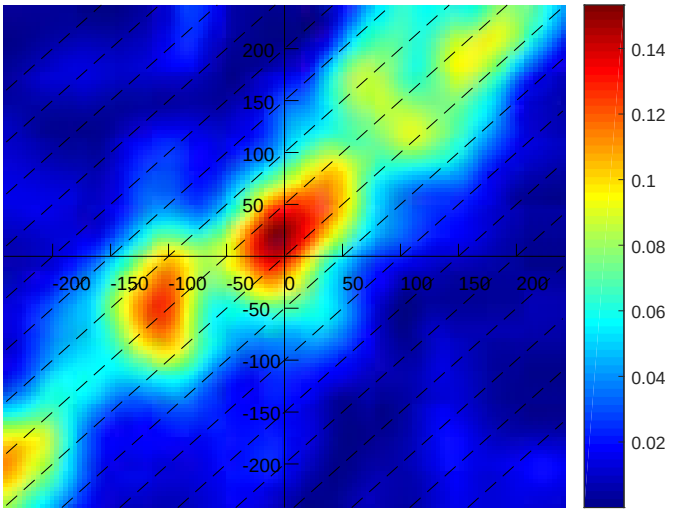

(b)

Fig. 4.1 Examples the conventional CMC and CMCTL. (a) The conventional CMC for a controlled motor tasks with two prominent coherence peaks marked by $\times$ signs, which will be referred to in Section 4.3. (b) CMCTL plotted around fixed (t_c, ω_c), in this case the coordinates of the second prominent peak. In this plot the x-axis represents τ_1 and the y-axis represents τ_2 in samples. Note that local maxima of the CMCTL are found away from the $\tau_1 = \tau_2$ line, demonstrating coherence enhancement achieved via CMCTL. Observe also that all local maxima of the CMCTL are situated on the same side of the $\tau_1 = \tau_2$ line, suggesting signalling in one direction.

4.2.2 Delay estimation

According to the equation for the coherence bias in (2.16), in the case of a single-path system the CMCTL is maximised when the time lag $\tau = \tau_2 - \tau_1$ is equal to the delay between the two processes. However, cortico-muscular interactions involve signalling over multiple paths, as modelled in (2.4), which blurs the notion of the delay. We propose to introduce the notion of the *global delay*, D_g, and in analogy with the single-path case define it as the time lag between the two processes corresponding to a local maximum of $C_{xy}(t_c, \tau_1, \tau_2, \omega)$:

$$D_g := \tau_2^\star - \tau_1^\star \ , \ (\tau_1^\star, \tau_2^\star) = \arg\max_{\tau_1, \tau_2} C_{xy}(t_c, \tau_1, \tau_2, \omega) \ . \tag{4.2}$$

It will be illustrated in the following that under some reasonable assumptions the global delay coincides with the mean of the distribution of the delays in the multi-path system.

The CMCTL is a four-dimensional function which is difficult to visualise and unnecessary to compute over the full range of its variables t_c, τ_1, τ_2, and ω. It was found to be practical to first compute the conventional CMC, identify peaks in the (t_c, ω_c) plane, and then compute CMCTL for t_c and ω_c corresponding to the locations of the peaks. Fig. 4.1 illustrates the procedure. The top plot shows the conventional CMC, where two prominent peaks are identified. The bottom plot then shows the CMCTL centred around the peak at $t_c = 3.441$ s, $\omega_c = 24$ Hz. Fig. 4.2 then shows the same CMCTL at a finer scale. Displacement pairs (τ_1, τ_2) with the same delay are situated along the lines parallel to $\tau_1 = \tau_2$, while the corresponding delay is equal to the coordinate of the crossing of such lines with the τ_2 axis (or the τ_1 axis, but with the reversed sign of the delay). It can be read from the plot in Fig. 4.2 that the estimated delay is approximately 25 ms.

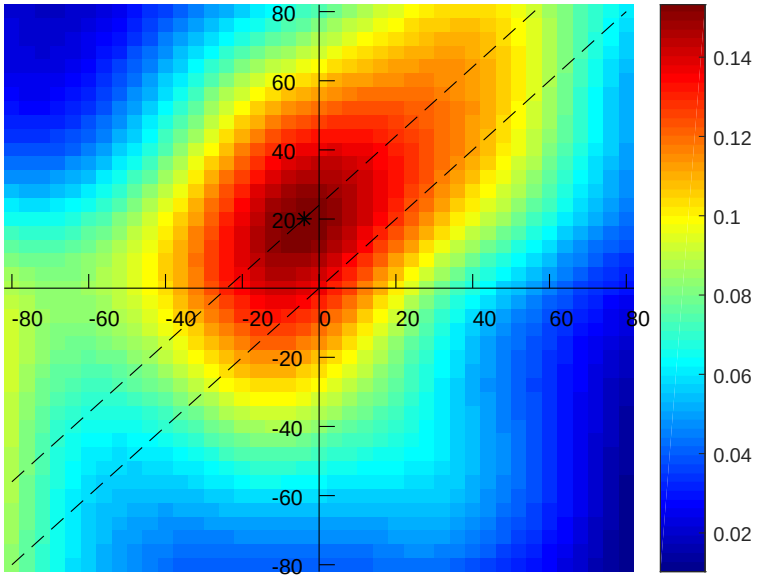

Fig. 4.2 The procedure of time delay estimation. Here the CMCTL plot from Fig. 4.1(b) can be observed at a finer scale. Again, the x-axis represents τ_1 and the y-axis represents τ_2 in samples. The dashed line through the origin corresponds to $\tau_1 = \tau_2$ and the asterisk marks the local maximum of the coherence. The dashed line going through this local maximum, with the slope equal to one intersects the axes at coordinates which are equal to the estimated delay.

The concept of estimation of the delay between two processes via the time lag that maximises their coherence has been previously proposed in the context of cortico-muscular coherence by Govindan *et al.* [39]. The authors proposed it for the estimation of the delay between stationary narrow-band signals, which inherently involves spectral estimation over relatively long time segments, and assumes constant-delay flow of information from one process to the other. The authors conclude that these assumptions are frequently violated in biological systems and that further work is needed to address the dynamic nature of cortico-muscular interactions. The method proposed in the thesis is designed to specifically deal with non-stationary processes, by using much shorter analysis windows, which

consequently cover a broader range of frequencies, and performing the estimation around local peaks of the CMC in the time-frequency plane. Further, due to the assumed stationarity, in [39] the authors estimate the delay by considering only time lags along τ_1 and τ_2 axes, whereas the CMCTL is considered in the whole (τ_1, τ_2) plane, and it will be seen in Section 4.3 that the maximum is always found away from the axes. Another major methodological difference is that in [39] the authors propose rectification of EMG signals, which is avoided here due to its non-linear nature and the resulting modification of the spectral content of EMG signals [21]. As a result of all these modifications delay estimates which are in much closer agreement with underlying physiology are obtained (see Section 4.3). Finally, an interpretation of delay estimates in the context of multi-path propagation is provided, and it is discussed in the next subsection.

4.2.3 Physical interpretation of the global delay

According to (2.16), which is derived for two processes $x(t)$ and $y(t)$ such that $y(t) = bx(t-D) + n(t)$, if in order to compensate for the delay, $y(t)$ is shifted by D_s in the opposite direction, the bias ratio of the coherence becomes

$$\frac{E[\hat{C}(\omega)] - C_{max}(\omega)}{C_{max}(\omega)} \approx -\frac{2|D-D_s|}{T} + \left(\frac{|D-D_s|}{T}\right)^2, \tag{4.3}$$

where T represents the length of observation window. Apparently, the coherence would be maximal when D_s is equal to the delay. However, if considering the model of motor control system in (2.4), sEMG signal has the form $y(t) = \sum_{i=1}^{N} b_i x(t-D_i) + n(t)$, which is a sum of several delayed and amplitude-scaled versions of the EEG signal $x(t)$ and additive noise. If we introduce a shift D_s in $y(t)$, the sEMG signal becomes $y(t+D_s) = \sum_{i=1}^{N} b_i x(t-D_i+D_s) + n(t)$,

hence

$$\begin{aligned} S_{xy}(\omega) &= E\left[\frac{1}{T}X(\omega)Y^*(\omega)\right] \\ &= \frac{1}{T}\int_0^T\int_0^T E\left(x(v)\Big(\sum_{i=1}^N b_i x^*(u-D_i+D_s)+n^*(u)\Big)\right) \\ &\quad \times e^{-j\omega v}e^{j\omega u}dudv \\ &= \frac{1}{T}\int_0^T\int_0^T\Big(\sum_{i=1}^N b_i R_{xx}(u-v-D_i+D_s)e^{j\omega(u-v)}\Big)dudv \end{aligned} \tag{4.4}$$

where R_{xx} is the autocorrelation function of $x(t)$. By letting $g=u-v$ and assuming R_{xx} is narrow, it is obtained that

$$\begin{aligned} S_{xy}(\omega) &= \frac{1}{T}\Big(\sum_{i=1}^N b_i\int_{-T}^T(T-|g|)R_{xx}(g-D_i+D_s)e^{j\omega g}dg\Big) \\ &\approx \left(\sum_{i=1}^N b_i\Big(1-\frac{|D_i-D_s|}{T}\Big)e^{j\omega(D_i-D_s)}\right)S_{xx}(\omega) \end{aligned} \tag{4.5}$$

In such a scenario, where the output is a sum of several delayed versions of the input, it is difficult to compensate all involved delays $D_1, D_2, ..., D_N$, but we can just find D_g which maximises the coherence. The bias ratio between the coherence and its maximum in this case has the following form

$$\frac{E[\hat{C}(\omega)]-C_{max}(\omega)}{C_{max}(\omega)} \approx \frac{\left|\sum_{i=1}^N b_i\Big(1-\frac{|D_i-D_s|}{T}\Big)e^{j\omega D_i}\right|^2}{\left|\sum_{i=1}^N b_i\Big(1-\frac{|D_i-D_g|}{T}\Big)e^{j\omega D_i}\right|^2}-1 \tag{4.6}$$

It can be shown that the same expression is valid also for the more general model described by (2.5) and (2.6) under the following two assumptions: (i) concurrent sensory and cortical events $x_0(t)$ and $y_0(t)$ are uncorrelated, (ii) $S_{x_0,x_0}(\omega) \approx S_{y_0,y_0}(\omega)$. The first assumption amounts to the fact that the brain cannot respond instantaneously to sensory input, while the second would be satisfied if both R_{x_0,x_0}

and R_{y_0,y_0} are narrow so that their spectra are approximately flat. The difference in the bias ratio formula in (4.6) between the unidirectional and bidirectional signalling scenarios is that delays D_i take only positive values in the former case, whereas in the latter case they can have both positive and negative values. Finding an analytical solution for the time lag D_g which maximises the coherence seems very challenging. Below, such a multi-path system is simulated and the impact of parameters of the distribution of the delays on D_g and the drop-off of the coherence away from its maximum is investigated.

The physiological data which are used in this study pertain to movement control of the hand, so in simulations of (4.6) the parameters are set to reflect signal propagation between the cortex and hand muscles. The scale factors and delays in the above models are influenced by several factors which include conduction velocity, fibre length, fibre diameter etc. [87, 107]. Based on the conduction velocity values of the nerve fibres, which is around $50-65$ m/s in the arms [108–110], and setting the distance between the scalp and the hand to around 1.2 m, most of the delays D_i obtained are between 18 ms to 24 ms. To introduce the effects of other factors, such as the conduction velocities of other kinds of fibres and the differences of their lengths, in the first instance we assume that D_i follow Gaussian distribution with mean of 20 ms and standard deviation of 4 ms, which means about 95% of the delays are between 12 ms and 28 ms. It has long been held that the surface myoelectric activity assumes a Gaussian amplitude distribution [111–115], hence the attenuation parameters b_i are also according to a Gaussian distribution normalised between 0.05 and 0.95.

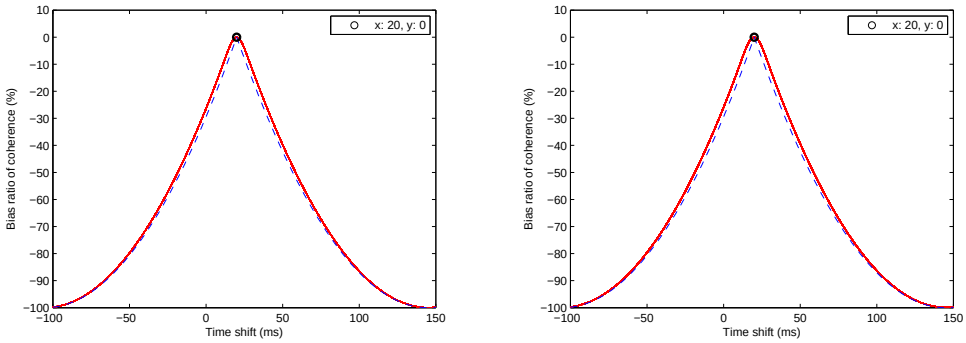

(a)

(b)

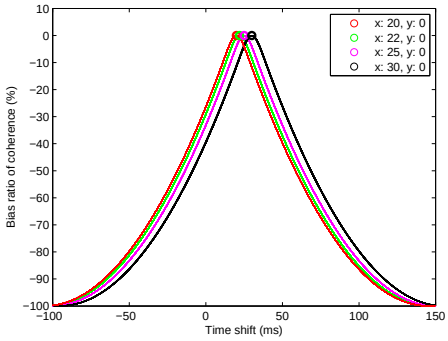

(c)

Fig. 4.3 Coherence bias curves in (4.6) for different distributions of delays between the brain and the muscle, along with the curve corresponding to the single-path case in (4.3) (dashed-blue). Each solid curve consists of 1000 curves, each of which is a different simulation of (4.6). The delay in the reference equation (4.3) is set to be the same as the corresponding global delay D_g of (4.6). (a) D_i assume Gaussian distribution with mean of 20 ms and standard deviation of 4 ms. (b) D_i assume Gaussian mixture distribution with the mean of 15 ms, 20 ms and 25 ms, with equal standard deviations of 4 ms, and weights equal to 0.25, 0.5 and 0.25, respectively. (c) The delays are modelled according to (2.3), where T_i assume Gaussian distribution with mean of 20 ms and standard deviation of 4 ms, while for $\tau_{i,k}$ four cases are considered: $\tau_{i,k}$ are all set to zero (red), which gives again the curves plotted in (a), and then $\tau_{i,k}$ assume Gaussian distributions with mean of 2 ms and standard deviation of 1 ms (green), mean of 5 ms and standard deviation of 1 ms (pink), and mean of 10 ms and standard deviation of 2 ms (black). The frequency f is set to 24 Hz and T is set to 125 ms. In all considered cases, coherence bias curves have maxima at time shifts D_g which coincide with means of propagation delay distributions.

Fig. 4.3 shows results of simulations of the multi-path formula in (4.6) for different propagation scenarios. The curve corresponding to the single-path bias

formula in (4.3) is represented by the dashed blue line, as a reference case where the delay is unambiguously defined. Fig. 4.3(a) shows first the case when D_i have Gaussian distribution with mean 20 ms and standard deviation 4 ms. The global delay D_g which maximises the coherence is in this case equal to the mean delay and the coherence has a relatively sharp peak at this value of D_g. The plots obtained are almost identical as shown in Fig. 4.3(b), for D_i distributed according to the mixture of three Gaussians, with means of 15 ms, 20 ms, and 25 ms, with equal standard deviations of 4 ms, and weights equal to 0.25, 0.5 and 0.25 respectively. Fig. 4.3(c) illustrates the case when each path involves also several branches. In particular, the model in (2.3), which considers T_i and $\tau_{i,k}$ separately, is simulated explicitly. The cases when T_i have Gaussian distribution with mean 20 ms and standard deviation 4 ms, while $\tau_{i,k}$ have Gaussian distribution with different means and different standard deviations are shown. This case also represents a model which involves linear time-invariant filtering along each path. In Fig. 4.3(c), the global delay of each case is the sum of the means of T_i and $\tau_{i,k}$, that is again the overall mean propagation time.

Finally, the effects of bidirectional signalling during the observation window are investigated. Fig. 4.4(a) shows the scenario in which one quarter of D_i are reversed, that is D_i is distributed according to a mixture of two Gaussians, one with mean -20 ms and the other with mean 20 ms, both with the same standard deviation of 4 ms, and with weights equal to 0.25 and 0.75, respectively. The value of D_g is now 19 ms, which is slightly smaller than the mean value of the delays in the dominant direction of propagation. The other example is an extreme situation illustrated in Fig. 4.4(b), corresponding to the mixture of the same two Gaussians but with equal weights. Whereas there are now four local maxima of the coherence, at D_g equal to -13 ms, -12 ms, 12 ms or 13 ms, they are not

prominent, and in fact the most prominent feature of the curve is its plateau which extends from -20 ms to 20 ms. Fig. 4.4(c) is the zoomed-in version of Fig. 4.4(b), which shows the different positions of D_g more clearly.

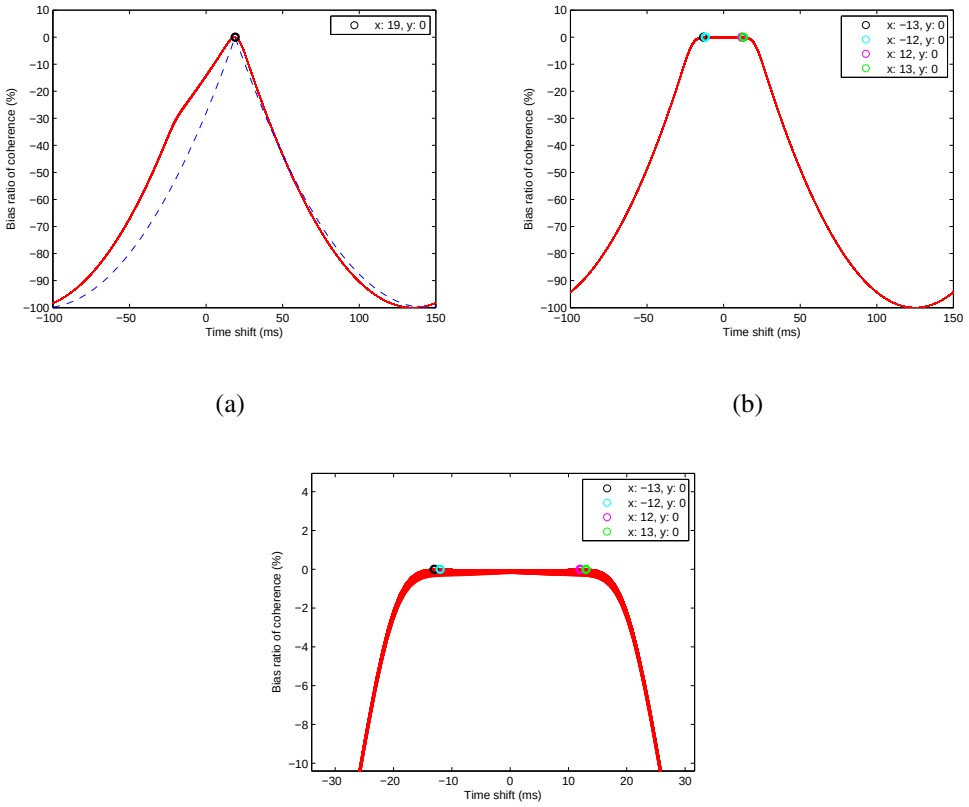

Fig. 4.4 Coherence bias curves in (4.6) for bidirectional coupling scenarios. (a) D_i are distributed according to a mixture of two Gaussians with standard deviation of 4 ms, and means of 20 ms and -20 ms, with weights equal to 0.75 and 0.25, respectively. Coherence bias curves in this case have prominent peaks, but their locations yield underestimates of mean delays of propagation in the dominant direction. Note, however, that although as much as 25% of signalling propagates in the opposite direction, the estimate of the mean delay in the dominant direction is not far from the actual value, *i.e.* 19 ms as opposed to 20 ms. (b) D_i are distributed according to a mixture of two Gaussians with standard deviation of 4 ms and means of 20 ms and -20, ms with equal weights. In this case there is no dominant direction of propagation. Coherence bias curves exhibit multiple local maxima, as marked on the plot, but these are not prominent. Instead, the curves exhibit a plateau which extends between the means of delays in the two directions. In all simulations, the frequency f is set to 24 Hz and T is set to 125 ms. (c) The zoom-in version of (b).

4.3 Results and Discussion

In this section, the results of applying the proposed methods described in Section 4.2 to EEG and FDI data recorded in the experiment described in Chapter 3 are presented. Conventional CMC is analysis in Section 4.3.1 and the locations of two prominent peaks are identified for each subject. Section 4.3.2 estimates the time delay by applying CMCTL centred around the specified peaks. The results are compared to those obtained using the methods reviewed in Chapter 2.

4.3.1 Time-frequency analysis

The STFT was performed on EEG and FDI signals collected in the experiment described in Chapter 3, using Hanning window of length $T = 125$ ms, shifted in 10-sample increments ($\Delta t = 9.8$ ms), as illustrated in Fig. 2.1(c). Reasons for choosing such window are given in Chapter 2 and Chapter 3. Fig. 2.1(c) shows most pronounced coherence in the frequency band centred at 24 Hz, and two prominent coherence peaks (also see Fig. 4.1 corresponding to Subject B), which will be referred to as Peak 1 and Peak 2. Centre frequencies, time instants, and levels of prominent coherence peaks of each subject are shown in Table 4.1. It can be noticed that the first prominent peak always appears between 1.5 s and 2.5 s while the second one appears between 2.5 s and 3.5 s.

4.3.2 Delay estimation and coherence enhancement

After the identification of two most prominent peaks, the CMCTL at time instants t_c and frequencies ω_c corresponding to these peaks was considered. Since the sampling frequency was 1024 Hz, the shortest time shift that could be identified was 0.98 ms. Nevertheless, owing to the length of observation window, the time

Table 4.1 Locations of the prominent peaks of the CMC between EEG and FDI across subjects.

Subject	Peak 1			Peak 2		
	Time (s)	Value	Frequency (Hz)	Time (s)	Value	Frequency (Hz)
B	1.898	0.1575	24	3.441	0.1356	24
J	2.162	0.1107	24	2.963	0.0842	24
K	1.674	0.1856	24	2.689	0.1490	24
L	2.123	0.0897	16	2.680	0.0771	16
N	1.957	0.0839	16	3.256	0.0578	32

resolution could not as high as 0.98 ms. Therefore, delay parameters τ_1 and τ_2 were varied in increments of 4 sampling points (about 3.9 ms) each. Before presenting results of delay estimation, it is of interest to investigate the drop-off of CMCTL away from local maxima. To that end τ_1 was fixed at the value corresponding to a local maximum of CMCTL and τ_2 was varied. Fig. 4.5 shows the drop-off curves obtained in this manner for both prominent peaks for two subjects. The drop-off curves corresponding to Peak 2 of both subjects are close to the drop-off profiles in Fig. 4.3 that correspond to unidirectional propagation, whereas the drop-off curves corresponding to Peak 1 are much wider, resembling more scenarios with bidirectional signalling illustrated in Fig. 4.4. A possible explanation is that Peak 1 is situated within a short time interval following the mechanical stimulus, when there could be more pronounced bidirectional signalling before movement control stabilises.

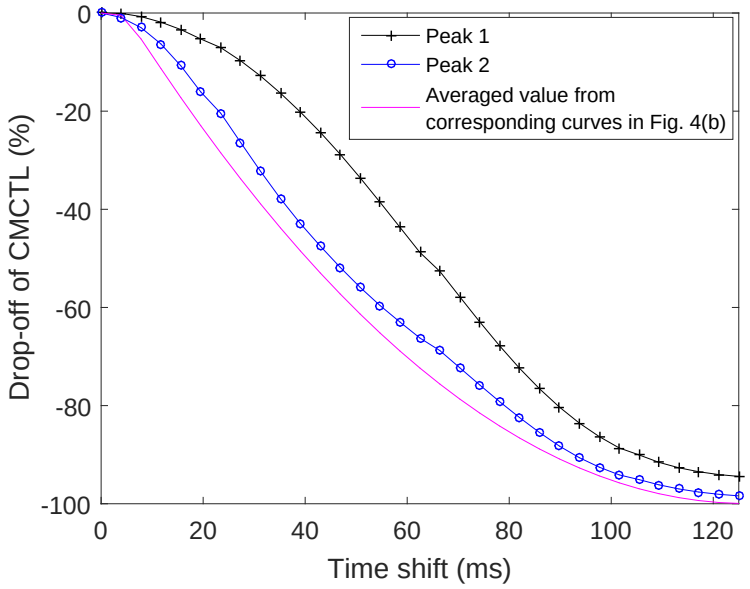

(a)

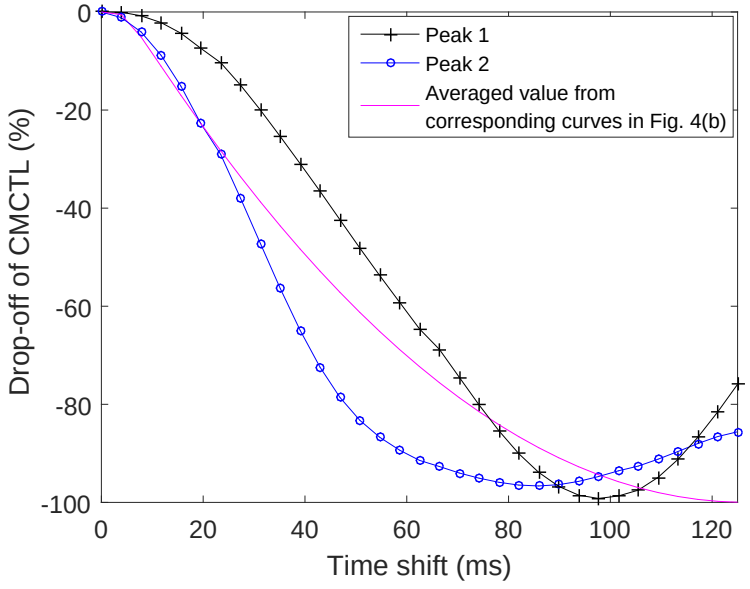

(b)

Fig. 4.5 Comparison between the bias ratio of Peak 1 (black), Peak 2 (blue) and the averaged values from the curves in Fig. 4.3(c) (pink). (a) Subject K (b) Subject L. The curves around Peak 2 are close to the drop-off profiles in Fig. 4.3(c) (pink), which correspond to unidirectional propagation, whereas the drop-off curves around Peak 1 are much wider, resembling more scenarios with bidirectional signalling illustrated in Fig. 4.4.

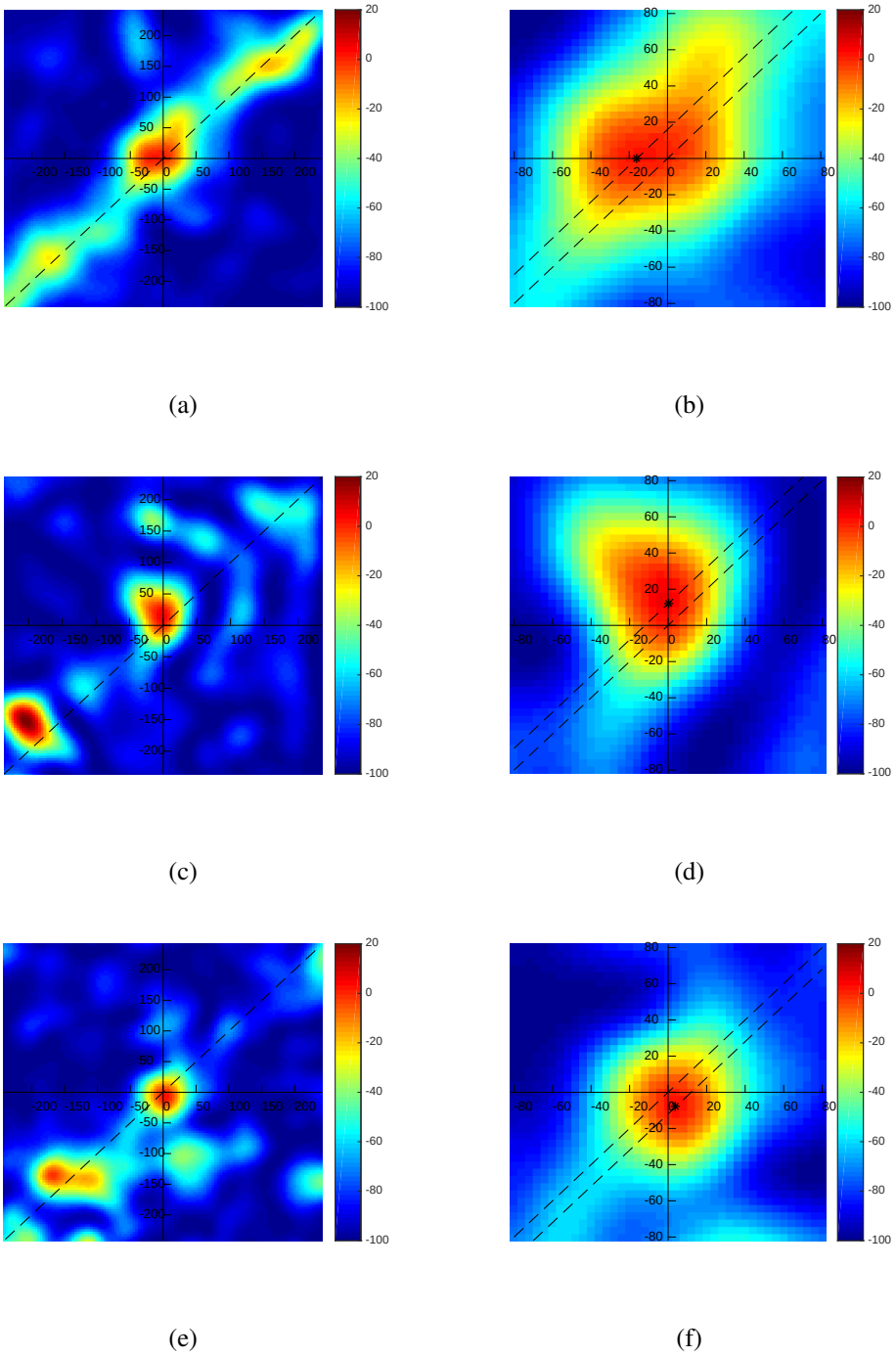

Fig. 4.6 Examples of CMCTL and time delay estimation around Peak 1. The x axis represents the shift of EEG, while the y axis represents the shift of EMG in samples, and the colour represents relative increase of coherence compared with that at the origin $(\tau_1, \tau_2) = (0, 0)$. Plots on the right are zoomed versions of the plots on the left. Local maxima are marked by "$*$" signs. Lines going through the maxima intersect the vertical axis at coordinates which are equal to the delay estimates.

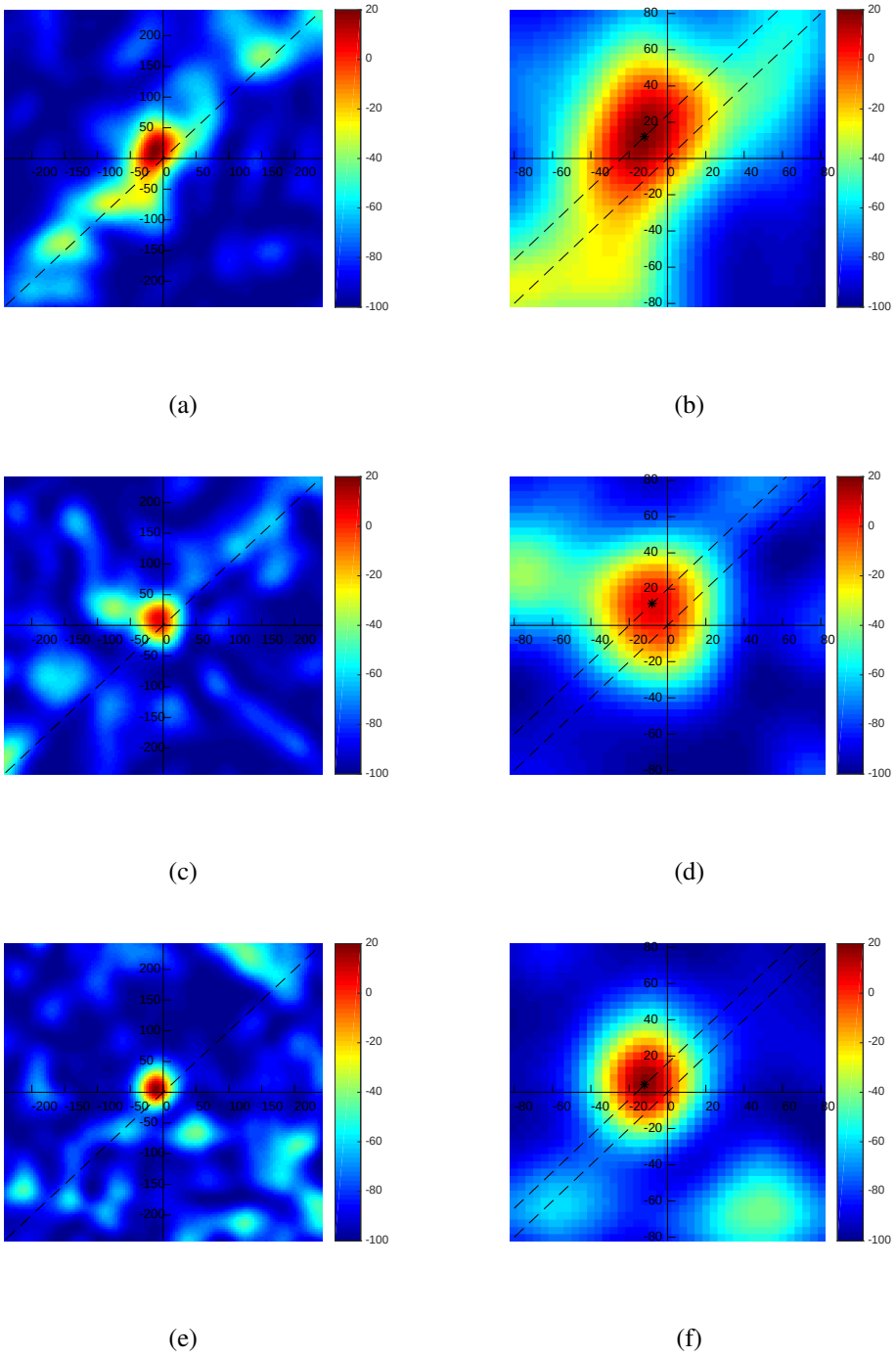

Fig. 4.7 Examples of CMCTL and time delay estimation around Peak 2. The x axis represents the shift of EEG while the y axis represents the shift of EMG in samples, and the colour represents relative increase of coherence compared with that at the origin $(\tau_1, \tau_2) = (0, 0)$. Plots on the right are zoomed versions of the plots on the left. Local maxima are marked by "$*$" signs. Lines going through the maxima intersect the vertical axis at coordinates which are equal to the delay estimates.

Table 4.2 Estimates of global time delays and levels of CMCTL increase at local maxima compared to the origin.

Subject	Peak 1		Peak 2	
	Global time delay (ms)	Coherence increase (%)	Global time delay (ms)	Coherence increase (%)
B	23.4 ±3.9	4.88	23.4 ±3.9	13.01
J	15.6 ±3.9	1.86	23.4 ±3.9	19.51
K	7.8 ±3.9	2.00	15.6 ±3.9	4.39
L	11.7 ±3.9	5.58	19.5 ±3.9	8.20
N	-11.7 ±3.9	2.72	15.6 ±3.9	19.45

Fig. 4.6 shows the CMCTL around Peak 1 for three subjects (J, L and N). It can be observed from these plots and the data in Table 4.2 that the CMCTL practically does not change in the small neighbourhood of the origin $(\tau_1, \tau_2) = (0,0)$, which based on the analysis in Section 4.2.3 and simulations shown in Fig. 4.4 suggests bidirectional signalling, and hence delay estimates that are lower than actual delays. It can be also noticed in Fig. 4.6(e) that there are areas of CMCTL increase on both sides of the $\tau_1 = \tau_2$ line, supporting further the presence of signalling in both directions. Fig. 4.6(b)(d)(f) show at a finer scale CMCTL regions around their local maxima, which are marked by "$*$". The intersection of the dashed-line passing though the coherence maximum with the τ_2 line in Fig. 4.6(b)(d)(f) then gives an estimate of the corresponding delays. Fig. 4.7 shows the CMCTL around Peak 2 for the same three subjects. It is evident from the figure and data in Table 4.2 that now the CMCTL increases significantly away from the origin $(\tau_1, \tau_2) = (0,0)$, and also that the highest coherence is found on the same side of the line $\tau_1 = \tau_2$, suggesting signalling in one direction and more accurate and reliable delay estimates. The global time delays estimated in this manner around Peak 1 and Peak 2 for the five subjects are shown in Table 4.2 (recall

that the time resolution of the CMCTL used for delay estimation is 3.9 ms). All delays estimated around Peak 2 are in the region 19.5 ± 3.9 ms which agrees with physiological facts discussed earlier. Delay estimates around Peak 1 are on average smaller, but still within the 19.5 ± 3.9 ms region except for Subject K. These lower delay estimates could be attributed to bidirectional signalling.

Table 4.3 Time delay estimates obtained by using state-of-the-art methods

Methods	Subject	Time delay (ms) of different time intervals				
		1.5 - 4.5 s	1.5 - 2.5 s	2 - 3 s	2.5 - 3.5 s	3 - 4 s
Phase-based estimation [28]	B	29.76	34.68	34.98	30.73	23.95
	J	1.52	2.07	0.94	2.31	5.69
	K	5.93	2.96	5.16	7.95	12.01
	L	19.17	8.76	28.36	52.59	53.99
	N	-2.71	21.48	14.47	4.38	10.33
Hilbert transform [30]	B	-29.3	-32.23	-31.25	-32.23	-32.23
	J	-16.60	-18.55	-19.53	-18.55	-19.53
	K	11.72	11.72	10.74	9.77	-31.25
	L	-37.11	-40.04	-37.11	-36.13	-39.06
	N	17.58	-51.76	15.63	-55.66	-55.66
Maximising coherence [39]	B	99.61	109.38	-17.58	57.62	28.32
	J	-7.81	-0.94	46.88	30.27	82.03
	K	-26.37	-49.80	0	-10.74	-94.73
	L	-52.73	0	-30.27	89.84	79.10
	N	-118.16	-186.52	21.48	-126.95	75.20

Subsequently, the above delay estimates are compared to those obtained using the linear phase model approach [28], its variation which estimates the non-linear component of the phase using the Hilbert transform [30], and the existing method based on maximising coherence [39]. Following the argument presented in [28], a weighted least squares regression was applied in the frequency range of significant coherence to fit a straight line through the phase of the cross-spectral density between EEG and EMG signals. Only the data collected in post-stimulus periods from 1.5 s to 4.5 s were used. These recordings were divided into three 1 s long non-overlapping segments. The time delays obtained in this manner vary widely across subjects. In order to decrease the effects caused by the non-stationarity of the signals and make the comparison with our algorithm more direct, the phase method was applied to different time intervals separately too. Then the modified algorithm based on the Hilbert transform was applied. Finally, the existing method based on maximising coherence was applied. Table 4.3 shows the estimated time delays in different intervals with these three approaches. Note that delays shorter than 10 ms are physiologically impossible given conduction velocities in nerve fibres [116]. The results in Table 4.2 are most directly comparable to the results of the other three methods in the $1.5-2.5$ s and $2.5-3.5$ s ranges, since Peak 1 and Peak 2, which are selected to estimate the global time delay around, are located in these intervals for all the subjects. Fig. 4.8 shows the phase spectra for three subjects (J, L and N). The weighted least squares regression analysis was applied to the frequency range where significant coherence appeared. The slope of the linear relation reveals the time delay between the synchronously recorded EEG and EMG. Comparing Table 4.2 with Table 4.3 shows that the results of our method are both more mutually consistent and in closer agreement with the underlying physiology.

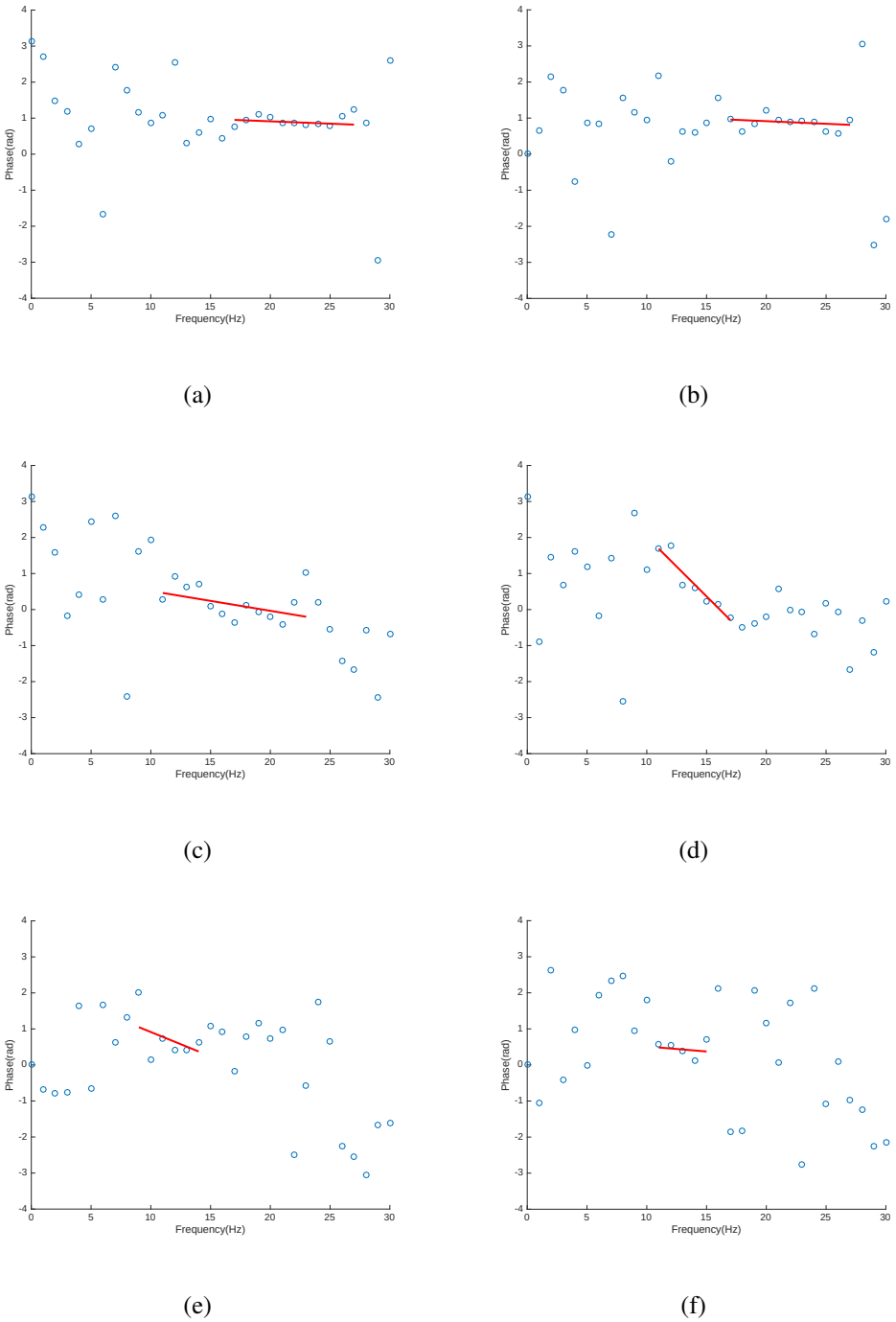

Fig. 4.8 Examples of delay estimation from phase spectrum. Red lines represent best-fit result from a weighted least squares regression analysis over frequency range of interest. Plots on the left and right show the phase spectra correspond to time interval $1.5 - 2.5$ s and $2.5 - 3.5$ s, respectively.

4.4 Further Considerations

Physiological studies have found that around $10-25\%$ of healthy subjects do not express significant cortico-muscular coherence. A question that naturally arises is whether in such cases the CMCTL can enhance the cortico-muscular coherence to a level above significance threshold. As it pointed out in Chapter 2, there are two known factors that could make CMC fall below the significance threshold: one is the bias due to misalignment, and the other is the contamination of EEG and EMG signals with noise and processes which are unrelated to the monitored activity [21]. The CMCTL methodology can compensate the bias due to misalignment, and in some cases that would be sufficient to reveal coherence which is normally not expressed. However, CMCTL cannot remove noise and other irrelevant EEG and EMG components, and if their combined level is high enough compared to the process of interest, the CMCTL alone will not be able to bring the coherence above significance threshold. Whereas denoising techniques are investigated in Chapter 5, it is worth noting here that adequate time-frequency resolution of spectral estimation which precedes coherence evaluation has the capability of implicitly enhancing the ratio between relevant signals and noise. To observe the underlying mechanism, note that the STFT transform is a two-dimensional sequence of correlations between a signal of interest and time-frequency atoms $\phi_{t_c,\omega_c}(t) = w(t-t_c)e^{j\omega_c t}$, where $w(t)$ is the STFT window function. The shape of the window function, its position in time t_c, and its centre frequency ω_c allow for some level of adaptation that could potentially increase the correlation of $\phi_{t_c,\omega_c}(t)$ with the signal of interest, and/or reduce its correlation with the noise, and thus increase the coherence. Fig. 2.2 shows an example of the opposite effect, where the time-frequency resolution of the spectral analysis at low-frequencies does not

match well the synchronised EEG and EMG events, which results in the drop of the coherence below the significance level.

The instances of the CMCTL revealing significant coherence in time-frequency regions where the conventional CMC was not expressed were noticed, however, that issue could not be investigated extensively using our data. Three of the subjects recruited for the original study [13] indeed did not express baseline CMC in the β range ($14-36$ Hz), which was of primary interest there, however, they all exhibited β-range CMC above the 95% confidence level following the stimulus.

Moreover, the spectral analysis using windows of length $T = 125$ ms, performed here, brought the coherence above significance level in some additional regions of the time-frequency plane, where it was not detected in the physiological study for which longer windows, $T = 500$ ms, were used [13].

Fig. 4.9 illustrates the enhancement of cortico-muscular coherence via a combined effect of adequate time-frequency resolution of the underlying spectral analysis and the CMCTL methodology. While significant coherence in the β range is not expressed in the time interval after 3 s when spectral analysis is performed using Hanning window of length $T = 500$ ms, with $\Delta t = 250$ ms shifts, (see Fig. 4.9(a)), the plot in Fig. 4.9(b) shows that the coherence in the same time-frequency region is revealed when Hanning window of length $T = 125$ ms is used, and shifted in time with $\Delta t = 9.8$ ms increments. Then the CMCTL was performed around the peak which emerged at $t_c = 3.461$ s and $\omega_c = 24$ Hz, which increased the level of coherence by another 24%, as shown in Fig. 4.9(c), bringing it ultimately to the 0.05 level.

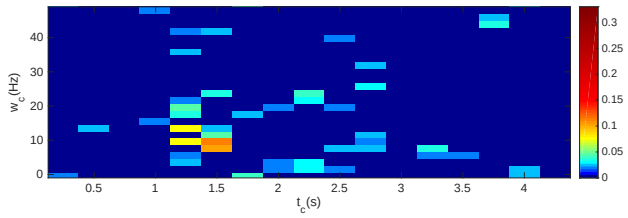

(a)

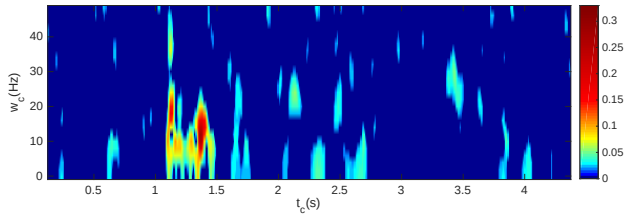

(b)

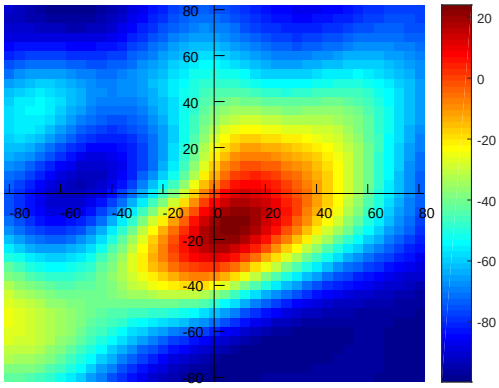

(c)

Fig. 4.9 Coherence enhancement achieved via adequate time-frequency resolution of spectral estimation combined with CMCTL. (a) The CMC plot obtained via the STFT computed at $M = 512$ frequencies, using Hanning window of length $T = 500$ ms, with $\Delta t = 250$ ms shifts between consecutive windows. The coherence is very weak, and cannot be observed in the β band in the interval after 3 s. (b) The CMC plot obtained via the STFT which is computed using Hanning window of length $T = 125$ ms, with $\Delta t = 9.8$ ms shifts between consecutive windows. The coherence is enhanced almost everywhere in the time-frequency plane, and becomes evident in the β band, in the interval after 3 s. (c) The CMCTL performed around the peak which emerged at $t_c = 3.461$ s, $\omega_c = 24$ Hz. It increases the maximum coherence value by another 24% bringing to 0.05. The colour scale in this plot represents the relative increase of the CTMCTL with respect to the CMCTL at the origin. CMC values below the 95% confidence limit are set to zero in both plots.

It is also worth noting that as a result of employing the time-frequency resolution provided by the shorter window, the coherence is enhanced everywhere in the β range, however it disappeared at frequencies below 10 Hz in the $3-3.5$ s interval, suggesting that optimal time-frequency resolution needs to be non-uniform, and that finding optimal solutions merits further research.

4.5 Conclusions

This chapter focused on estimating the delay between the motor cortex and the periphery in addition to coherence enhancement through compensation of the delay. According to the model of the motor control system presented in Chapter 2, different delays may be involved corresponding to events propagating via multiple paths. Other than the delay defined in the case of a single-path system, the global delay was introduced to define the delay in the case of a multi-path system, which is a more realistic model of cortico-muscular pathways than the commonly assumed single-path system. The physical interpretation of the global delay was discussed in this chapter and simulations for different propagation scenarios were performed, which gave a deeper comprehension over the view of the delay in multi-path propagation. Bidirectional coupling that happens simultaneously in different pathways, which could not be ignored was investigated as well. In order to avoid the interference caused by different events, the delay estimation was investigated around the time instant corresponding to some specific coherence peaks. The CMCTL, which is the coherence between EEG and EMG segments taken with a time lag from a central observation point was introduced and an algorithm for estimating the delay between coupled cortical and muscular events

as the time lag corresponding to the local maxima of the CMCTL function was proposed.

Using physiological data, the potential of the CMCTL function to increase coherence levels was illustrated and the information about temporal structures of cortico-muscular interactions was provided. Delay estimates obtained by applying the proposed algorithm to physiological data are in close agreement with underlying physiology, whereas in the situations when that is not the case, the discrepancies are in agreement with the analysis provided in this chapter. Moreover, cases regarding the subjects with no significant CMC expressed were considered and examples of increasing CMC to significant level via CMCTL were shown.

The technique of CMCTL also has capacity to enhance coherence, but it is limited. The means of denoising with regard to removing incoherent components is needed for increasing CMC, which will be presented in the next chapter.

Chapter 5

CORTICO-MUSCULAR COHERENCE ENHANCEMENT

The previous chapter introduced the methodology of CMCTL, which in addition to its use in estimation of the time lag between synchronous processes in the brain and muscles, exhibited some, albeit limited ability to increase the level of CMC. The main reason for the typically low level of coherence between sEMG and EEG signals collected synchronously during controlled motor tasks is the presence of noise and activities unrelated to the task of interest. This chapter explores techniques for enhancing CMC via the methods which aim to separate synchronous cortico-muscular components from the mixtures captured by sEMG and EEG recordings. The proposed approaches are assessed using the simulated data and the data collected in the experiments described in Chapter 3. It will be shown that the proposed methods can achieve substantial CMC enhancement.

5.1 Introduction

The influence of noise components on the level of coherence was discussed earlier in Section 2.2.2. Aiming to extract the signal $y_c(t)$ responding to the considered cortical excitation signal $x_c(t)$ from the original noise-corrupted sEMG signal $y(t) = y_c(t) + n_y(t)$, this chapter turns attention to increasing the level of CMC by removing noise components.

One approach towards increasing the level of EEG and EMG components relative to the considered activities is via blind source separation (BSS) techniques, which aim to separate individual components from their noisy mixtures. ICA being a type of BSS method, has been successfully used for the denoising of multi-channel EEG and EMG signals [46–49]. We propose a method for noise reduction, which is inspired by Wavelet Independent Component Analysis (WICA). This method is useful especially for low-channel count data, which are of particular importance for minimising health-care costs and simplifying the operation of diagnostic data collection.

Another approach proposed in this chapter is inspired by the techniques of sparse signal representation, which has become one of the most active areas in digital signal processing over the past decade. Most natural signals are a superposition of only a few waveforms from their corresponding highly structured dictionaries. In our setting, we postulate that with a properly constructed dictionary and well designed sparse decomposition techniques, it is possible to represent motor-control components in EEG and EMG signals using a few higher amplitude waveforms, while the background activity and noise will spread over many low intensity components due to the absence of structure [117]. The means above has

a potential to facilitate the extraction of relevant components from EEG and EMG signals, ultimately leading to increased CMC levels.

This chapter is organised as follows. In Section 5.2, a method is proposed for enhancing relative levels of sEMG components coherent with the synchronously recorded EEG signal via a variant of WICA combined with a novel component selection algorithm. The effectiveness of the proposed algorithm is demonstrated using the data collected during neurophysiological experiments. This coherence enhancement method will be referred to as Coherent Wavelet Enhanced Independent Component Analysis (COWICA). Section 5.3 presents a denoising method based on dictionary learning and sparse signal representation.

5.2 Coherent Wavelet Enhanced Independent Component Analysis

As introduced in Section 2.4.4, WICA has been used in previous studies to overcome the limitation of insufficient numbers of channels for ICA to be able to separate independent sources from their mixtures [50–53, 55]. Inspired by these studies, this section investigates applying wavelet decomposition prior to ICA to generate wavelet components (WCs) and thus increase the effective number of mixtures in the context of CMC analysis.

Section 5.2.1 describes the proposed method which combines WICA that separates independent components and a greedy algorithm for components selection that aims to maximise the coherence between resynthesised sEMG signal and EEG. In Section 5.2.2, simulated data are used for an assessment of the effectiveness of COWICA approach under different signal-to-noise ratios (SNRs). The method is then applied to data collected in the neurophysiological experiments

and compared in terms of its effectiveness in enhancing CMC to the denoising algorithm based on wavelet expansion thresholding, described in Section 2.4.2, which is commonly used for noise removal in biological signal processing. The impact of main COWICA parameters on the effectiveness of the method is then investigated. Further considerations about combining the COWICA with CMCTL are presented in Section 5.2.3.

5.2.1 Methodology

The main idea behind WICA is that certain independent components may not be present in all components of the wavelet decomposition of the original available signals, so that their wavelet expansion components may yield a relatively higher number of different mixtures. In motor control, different consecutive frequency bands have different functional importance, which suggests that WICA could be particularly effective in the context of separating independent components from low-channel count sEMG recordings, and that the frequency resolution of the underlying wavelet decomposition should mimic functional sEMG bands.

In order to increase the number of components as much as possible, all wavelet expansion components up to a certain scale P are used as the input to ICA. The matrix of mixture sEMG signals then becomes a matrix of WCs, which is $\mathbf{Y}_{WC} = [\mathbf{y}_{1,1} \ \ldots \ \mathbf{y}_{1,P+1} \ \ldots \ \mathbf{y}_{N_{\text{mix}},1} \ \ldots \ \mathbf{y}_{N_{\text{mix}},P+1}]^T$, where $\mathbf{y}_{j,1},\ldots,\mathbf{y}_{j,P+1}$ are the wavelet expansion vectors corresponding to sEMG signal of the jth channel and the number of mixtures increases from N_{mix} to $N'_{\text{mix}} = N_{\text{mix}} \times (P+1)$. Then a matrix of source signals $\mathbf{Q} = [\mathbf{q}_1 \ \mathbf{q}_2 \ \ldots \ \mathbf{q}_{N_s}]^T$ can be obtained by ICA, which corresponds to the wavelet independent components (WICs).

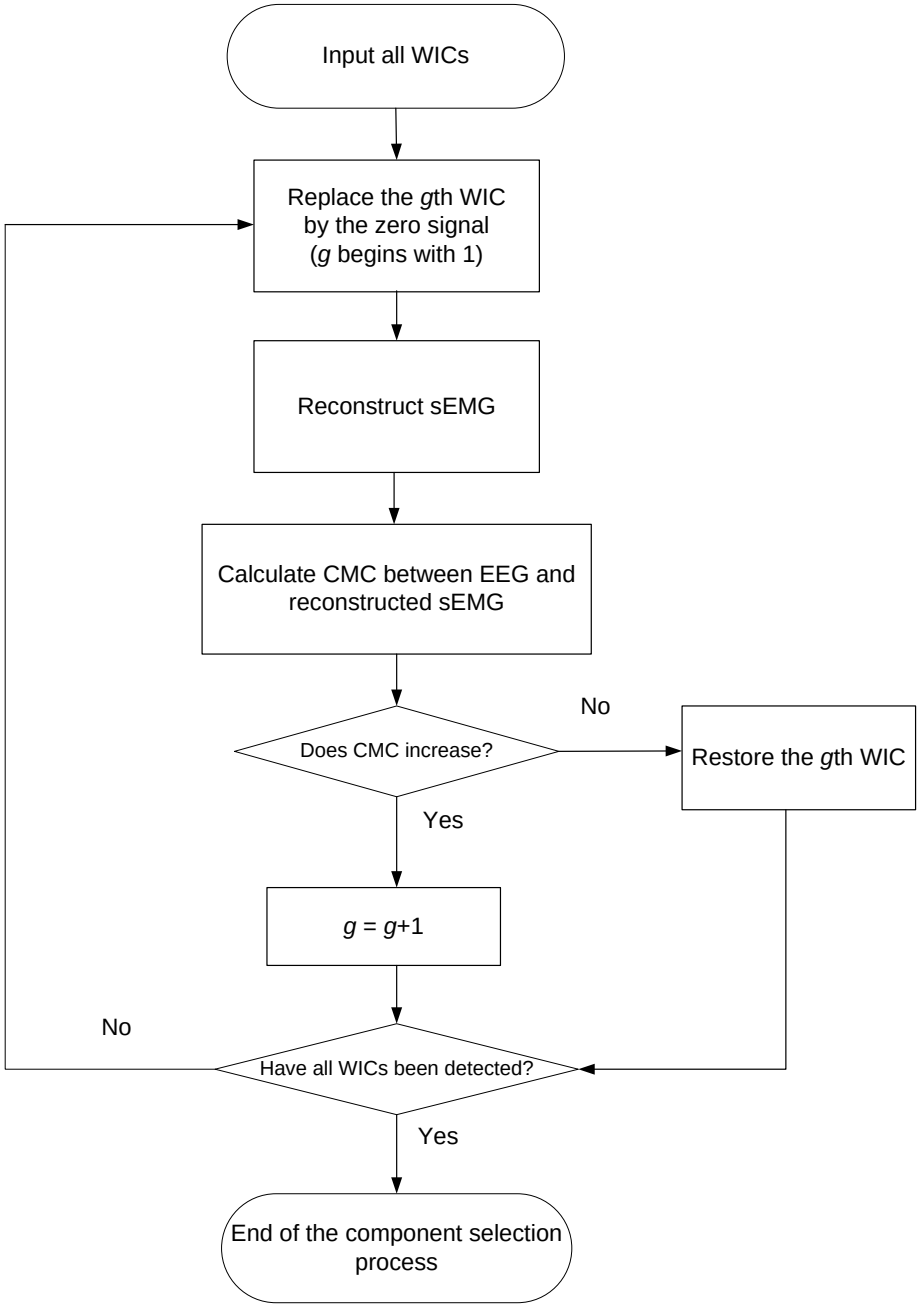

Fig. 5.1 Flowchart of the component selection process. The procedure consists of three steps: (1) initialisation, (2) WIC removal, (3) CMC estimation and WIC selection.

The problem that needs to be resolved once WICs are obtained is to find those which constitute the sought sEMG activity. Since in the context of CMC analysis, a synchronous EEG signal is available, the method is proposed to select WICs based on their impact on CMC level, as those which are involved in the considered motor task would increase the overall coherence level, whereas those which are unrelated to the task would effectively act as an independent noise that lowers the coherence. For that purpose a greedy selection algorithm is proposed. A subset of components $\mathbf{q}_i$ selected in this manner is recombined, aiming to reconstruct a version of sEMG which contains a higher relative level of the component $y_c(t)$ which is the response to the cortical activity $x_c(t)$. The proposed algorithm is illustrated by the flowchart shown in Fig. 5.1, and its details are as follows:

1) **Initialisation.** Perform WICA on input sEMG signals to obtain WICs $\mathbf{q}_j,\ j = 1,2,...,N_s$. WICs obtained by WICA are input for the selection. An WIC counter g is set to $g = 1$, and the initial value of CMC, C_{xy}^0, is computed as the value of CMC between EEG and sEMG that is reconstructed with all WICs.

2) **WIC removal.** The gth wavelet independent component (WIC) is removed, *i.e.* it is replaced by the zero signal. The matrix of WICs is thus updated with the gth WIC discarded, and sEMG signal is reconstructed with the updated matrix of WICs.

3) **CMC estimation and WIC selection.** The CMC between EEG and reconstructed sEMG signals is calculated. If it is higher than C_{xy}^{g-1}, the coherence C_{xy}^g to be compared next time will be updated with the value of CMC calculated between EEG and the reconstructed sEMG signals. Otherwise, if the CMC is lower than or equal to C_{xy}^{g-1}, the gth WIC, $\mathbf{q}_g$, is restored in

the updated matrix of WICs and the reference coherence level is set to $C_{xy}^{g} = C_{xy}^{g-1}$.

4) **Iteration.** The index g is incremented by 1 and steps 2) to 4) are repeated until all WICs have been considered, *i.e.* $g = N_s$.

The coherence between EEG and sEMG, which are non-stationary processes, was estimated in this study in the short-time Fourier domain [72, 75]. In particular, the time-varying power spectral and cross-spectral densities were estimated by averaging the STFT magnitude spectra over different epochs via (2.10) and (2.11). The coherence between EEG and reconstructed sEMG is then estimated following (2.12). Note that only the CMC at peak frequency is taken into account during the process of the proposed component selection algorithm.

5.2.2 Results and discussion

Before applying the proposed method to the EEG and sEMG signals which were acquired during a motor control task introduced in Chapter 3, the performance of COWICA method for simulated data under different SNRs is investigated. The simulated EEG data were generated by the wavelet-based method Bridwell *et al.* proposed in [118]; the code is available at http://mialab.mrn.org/software/simeeg. In order to mimic the motor control task introduced in Chapter 3, only the component corresponding to β band was regarded as the cortical excitation signal that was related to the process of interest. To be specific, the simulated EEG signal was filtered by a Butterworth bandpass filter with the lower cutoff frequency of 13 Hz and a higher cutoff frequency of 36 Hz. Then, simulated sEMG signals of two channels, Channel 1 and Channel 2, were generated by passing the output of the bandpass filter through two LTI systems. Both systems were modelled as having

20,000 paths with different attenuations and delays, generated as described in Section 4.2.3.

The simulated sEMG of Channel 1 was used as the sEMG signal to be denoised and the sEMG of Channel 2 was used as an additional signal for the COWICA algorithm to separate independent components from the two-channel sEMG signals before the reconstruction of sEMG corresponding to Channel 1. Pseudorandom noise with normal distribution was added to both EEG and sEMG signals. Two additional components added to sEMG data were generated using the sum of sine waves with random attenuations and phases. These components are regarded also as "noise" since these frequency bands are not involved in considered motor tasks.

The COWICA method with $'db1'$ was applied to 180 segments of two-channel sEMG signals simulated in this manner. Each segment was 128 samples long. The number of scales of the wavelet transform used in this experiment was set to 7, and the number of independent components was set to 14. Results of the experiment are shown in Table 5.1. It can be observed from the table that the relative increase in CMC levels exhibits a monotonically increasing trend as the SNR decreases, whereas the overall CMC level increases with the SNR.

Table 5.1 Increase of CMC between EEG and reconstructed sEMG achieved by COWICA for simulated data under different SNRs

SNR (dB)	Original CMC value	after COWICA	
		CMC value	CMC increase (%)
-20	0.0354	0.0952	168.93
-15	0.1818	0.3171	74.42
-10	0.4612	0.6149	33.33
-5	0.7146	0.8514	19.14

The algorithm was then applied to EEG and sEMG data recorded in the neurophysiological experiment described in Chapter 3. The FDI signal was used as the sEMG to be denoised, whilst the FPB signal was used with FDI for the separation of independent components. The coherence between EEG and FDI was estimated via the STFT using Hanning window of length W = 125 ms (128 samples) with shifts Δt = 9.8 ms (10 samples) that provided the most suitable time-frequency resolution [23]. The COWICA was applied to each window of data separately.

The COWICA was compared in terms of its effectiveness in CMC enhancement to wavelet threshold denoising (WTD). Both WTD and the wavelet decomposition step of COWICA, were performed using *Daubechies*, *Symlets* and *Coiflet* wavelet families. Since the sampling rate used was 1024 Hz, and α (8 to 13 Hz), β (13 to 36 Hz) and γ (36 to 85 Hz) frequency bands have different functions in sensory-motor integration, in order to approximate this frequency resolution, 7 scales of the wavelet transform were used. The number of independent components was set to 14. However, for the WTD, the most effective number of scales depends on the particular subject. The results are reported for the number of scales which achieved the highest coherence increase. Note that in the case of WTD both EEG and sEMG are denoised, whereas in the case of COWICA only sEMG was enhanced.

An example of CMC enhancement of subject B after WTD and COWICA is shown in Fig. 5.2(b) and Fig. 5.2(c), respectively, in comparison with the original CMC shown in Fig. 5.2(a). It can be observed from these figures that both methods increase CMC especially where it exhibits strong synchronisation, but COWICA improves CMC markedly whilst WTD practically does not achieve pronounced enhancement. Moreover, after applying COWICA, significant coherence appears

even where it could not be observed in both pre-stimulus period (0 s to 1 s) and post-stimulus period (1.5 s to 5 s).

Next, COWICA is compared with WTD in terms of the increase of CMC at specific coherence peaks. The thesis focuses on the CMC enhancement at prominent coherence peaks instead of the averaged increase of CMC of the whole signal, because the motor cortex and the periphery might not exhibit synchronous behaviour all the time. The methods were only applied to the segments corresponding to two prominent peaks. Peak 1 appears between 1.5 s and 2.5 s, and Peak 2 appears between 2.5 s and 3.5 s [23] after the beginning of the data collection period. Random initial weight matrix $\mathbf{W}$ was used for FastICA algorithm, which is based on a fixed-point iteration scheme [93], and the best results achieved over 100 such random initialisations were presented. Table 5.2 shows relative increase in the level of CMC at the two prominent peaks in the post-stimulus period. It can be observed that CMC is increased substantially by applying COWICA, however WTD does not improve the coherence considerably. Note that in Table 5.2 for WTD the best results of those achieved with different wavelets and number of scales of the wavelet transform are presented. Results obtained by using COWICA are shown for Daubechies wavelets $'db1'$, $'db4'$, $'db7'$ and $'db10'$ and 7 scales of the wavelet transform. Comparable results were obtained with other wavelet families.

Lastly, the impact of some COWICA parameters on the effectiveness of CMC enhancement is investigated. Taking Peak 2 of subject B as an example, Table 5.3 shows how the coherence value changes under different levels of wavelet decomposition and when the preset initial number of sought independent components varies. Note that COWICA with $'db1'$ was applied and it was applied to just 128 samples around Peak 2. It can be observed from Table 5.3 that the coherence value

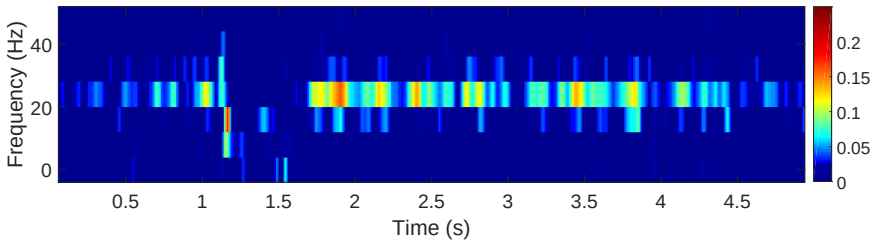

(a)

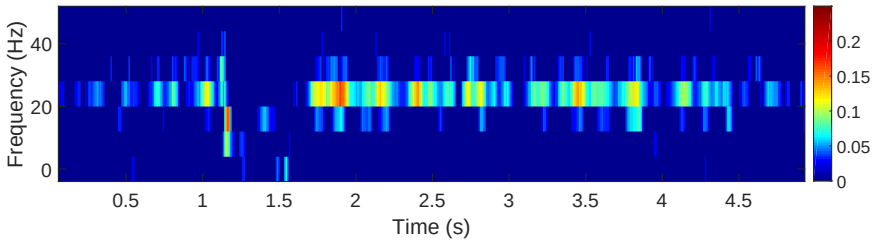

(b)

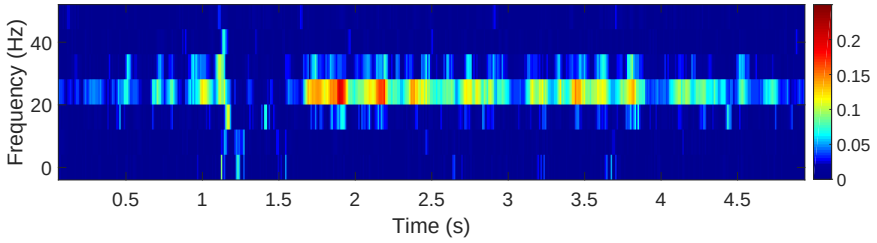

(c)

Fig. 5.2 CMC plots obtained with Hanning window of length $W = 125$ ms and shifts of 9.8 ms between consecutive windows. CMC values below the 95% confidence limit are set to zero. (a) Original CMC between EEG and sEMG. (b) CMC between EEG and sEMG after denoising performed by applying WTD with *sym*8 wavelet at 4 scales. (c) CMC between EEG and denoised sEMG after applying COWICA with *db*7 wavelet at 7 scales.

Table 5.2 Increase of CMC achieved by COWICA and WTD

Subject	Coherence increase of Peak 1 (%)					Coherence increase of Peak 2 (%)				
	by	by COWICA				by	by COWICA			
	WTD	*db*1	*db*4	*db*7	*db*10	WTD	*db*1	*db*4	*db*7	*db*10
B	7.11	28.89	30.41	32.89	32.70	3.69	23.89	17.26	18.66	16.22
J	4.61	31.62	18.79	17.34	19.51	5.30	30.05	23.28	19.60	24.70
K	4.15	12.50	11.91	13.39	15.09	8.99	44.83	33.29	36.51	40.74
L	12.42	24.30	27.76	27.98	31.22	5.51	29.31	38.26	33.72	41.50
N	6.96	30.99	33.84	33.25	32.66	3.27	83.04	27.85	33.21	28.37

varies only a little when the number of independent components changes whilst the number of scales of the wavelet decomposition is fixed, which indicates that the result of COWICA is not sensitive to the number of independent components. In terms of the number of scales of wavelet decomposition, coherence value does not change much when it is decreased from 7 to 6. However, when the number of scales is lower than 6, the final coherence value, obtained after component selection, exhibits a considerable decrease. There is nearly no increase of coherence when the number of scales is 2. A possible explanation is that since the sampling frequency is 1024 Hz, when the number of scales is 7 or 6, there will be a wavelet component that just covers the β-range frequency band, in which CMC is observed primarily in this study. On the other hand, when the level is lower than 6, the component which contains the β-range frequency band also involves some other frequency bands.

Table 5.3 Coherence values between EEG and reconstructed sEMG after applying COW-ICA with different levels of wavelet decomposition and different numbers of independent components

Level of wavelet decomposition	Number of independent components	Coherence value
7	14	0.1680
	10	0.1682
	6	0.1688
6	14	0.1677
	10	0.1672
	6	0.1662
5	12	0.1591
	8	0.1603
	4	0.1597
4	10	0.1444
	8	0.1432
	4	0.1468
3	8	0.1402
	6	0.1416
	4	0.1414
2	6	0.1365
	4	0.1375
	2	0.1352

5.2.3 Combination of cortico-muscular coherence with time lag and coherent wavelet enhanced independent component analysis

As discussed in Chapter 4, the CMCTL methodology can also enhance CMC levels, so the idea that seems worth considering is to combine the CMCTL method with the COWICA for even better results. Moreover, delay estimates obtained by means of CMCTL methodology can be used to align synchronous processes and

boost the effectiveness of COWICA. However, some issues have to be considered before these two approaches can be combined.

In order to combine these two methods, not only the CMCTL between EEG and FDI signals, but also the CMCTL between EEG and FPB signals needs to be considered, as FDI and FPB are the two available sEMG signals. The COWICA is then meant to be applied to the shifted version of EEG and the two-channel sEMG segments around prominent coherence peaks, as they indicate the presence of synchronous cortico-muscular activities. Table 5.4 shows the time instants, values and centre frequencies of prominent peaks of the coherence between FPB and EEG signals of each subject. However, locations of the corresponding coherence peaks between EEG and synchronous FDI signals, shown in Table 4.1, can be substantially different. For most subjects, the locations vary within 20 ms in time domain. However, sometimes the difference can be substantial not only in time domain but also in the frequency domain. For example, Peak 2 of the coherence between EEG and FDI of subject N is located at 3.256 s, centring at 32 Hz, but it moves to 3.627 s and 16 Hz for the CMC between EEG and FPB. It is unclear whether applying the COWICA to such segments corresponding to different recording times is meaningful at all. In addition, when calculating the coherence between EEG signal and the reconstructed sEMG signal, in order to select eligible components, it is unclear what should be the frequency at which the coherence should be maximised. These issues require further consideration before the CMCTL and COWICA methodologies could be combined properly.

Table 5.4 Locations of the prominent peaks of the CMC between EEG and FPB across subjects.

Subject	Peak 1			Peak 2		
	Time (s)	Value	Frequency (Hz)	Time (s)	Value	Frequency (Hz)
B	1.918	0.1607	24	3.461	0.1050	24
J	1.713	0.1200	24	2.963	0.0806	24
K	1.674	0.1255	24	3.002	0.1553	24
L	2.113	0.0795	16	2.689	0.0410	16
N	1.947	0.0890	16	3.627	0.0950	16

5.3 Coherent component enhancement via sparse signal representation

This section considers separation of weak coherent signals using techniques of dictionary learning and sparse signal representation. In Section 5.3.1, the problem of sparse representation of synchronous EEG and sEMG signals is formulated first, followed by an overview of Alternating Direction Method of Multipliers (ADMM) algorithm, which is used here to solve this problem. Analogously to the development of the COWICA, the sparse representation method is then combined with a greedy component selection algorithm geared towards increasing CMC levels. The effectiveness of proposed approach is illustrated by applying it to the simulated data and the neurophysiological signals described in Section 5.3.2.

It is important to note that the sparse signal representation can be guaranteed if the restricted isometry property (RIP) condition [119] is satisfied [120]. Note, however, that RIP is only a sufficient but not a necessary condition for sparse recovery [120]. Moreover, verifying the RIP itself is an NP-hard problem. Hence,

we do not insist on the RIP in this study. Instead, as our intention is to facilitate the extraction of coherent components from EEG and sEMG signals, the same motor control task is repeated L times ($L \approx 200$) and the sparse representation of simultaneously recorded EEG signals $\mathbf{X} = [\mathbf{x}_1\ \mathbf{x}_2\ ...\ \mathbf{x}_L],\ \mathbf{x}_i \in \mathbb{R}^n$ and sEMG signals $\mathbf{Y} = [\mathbf{y}_1\ \mathbf{y}_2\ ...\ \mathbf{y}_L],\ \mathbf{y}_i \in \mathbb{R}^n$ is estimated. Since there is a repetition of the motor-control signal of interest, whereas the noise is random, the signal of interest is assumed to have a sparse representation so that it is possible to represent motor-control components using a few higher amplitude waveforms, while noise will spread over many low intensity components. There, however, can be components that are not relevant to the considered activity but also repeated over experiment trials. Therefore, a component selection algorithm is proposed to extract relevant components further by selecting the components which contribute to the coherence between reconstructed EEG and sEMG signals.

5.3.1 Methodology

To achieve the enhancement of coherent components in EEG and sEMG signals, first a dictionary in which they could potentially be represented in a sparse manner needs to be learned. The main idea of the algorithm proposed here is that structured synchronous EEG and sEMG components are expected to have sparse representation under such a common dictionary, which could facilitate noise removal. Hence, the aim is to find one dictionary $\mathbf{D} \in \mathbb{R}^{n \times K}$ for simultaneously recorded EEG signal $\mathbf{X} = [\mathbf{x}_1\ \mathbf{x}_2\ ...\ \mathbf{x}_L],\ \mathbf{x}_i \in \mathbb{R}^n$ and sEMG signal $\mathbf{Y} = [\mathbf{y}_1\ \mathbf{y}_2\ ...\ \mathbf{y}_L],\ \mathbf{y}_i \in \mathbb{R}^n$, where L is the number of trials in which both signals have sparse representation. To that end the matrix $\mathbf{R} = [\mathbf{X}\ \mathbf{Y}]$ of observation is formed and the dictionary is obtained by solving the problem in (2.34).

The sparse representation of EEG and sEMG signals with respect to this dictionary has the form

$$\begin{aligned} \hat{\mathbf{X}} &= \mathbf{D}\mathbf{S}_x, \\ \hat{\mathbf{Y}} &= \mathbf{D}\mathbf{S}_y \ , \end{aligned} \tag{5.1}$$

where $\mathbf{S}_x = [\mathbf{s}_{x,1}\ \mathbf{s}_{x,2}\ \ldots\ \mathbf{s}_{x,L}], \mathbf{s}_{x,i} \in \mathbb{R}^K$ and $\mathbf{S}_y = [\mathbf{s}_{y,1}\ \mathbf{s}_{y,2}\ \ldots\ \mathbf{s}_{y,L}], \mathbf{s}_{y,i} \in \mathbb{R}^K$ are the sparse expansion matrices corresponding to $\mathbf{X}$ and $\mathbf{Y}$, respectively. Once the dictionary $\mathbf{D}$ is generated, the sparse representation problem above can be formulated as

$$\min_{\mathbf{s}_{x,i},\mathbf{s}_{y,i}} \left\{ \sum_{i=1}^{L} \{ \frac{1}{2} \parallel \mathbf{x}_i - \mathbf{D}\mathbf{s}_{x,i} \parallel_2^2 + \frac{1}{2} \parallel \mathbf{y}_i - \mathbf{D}\mathbf{s}_{y,i} \parallel_2^2 + \lambda_1 \parallel \mathbf{s}_{x,i} \parallel_1 + \lambda_2 \parallel \mathbf{s}_{y,i} \parallel_1 \} \right\} . \tag{5.2}$$

Whilst techniques of dictionary learning typically produce both sparse representations of EEG and sEMG signals as well as the underlying dictionary, in order to obtain higher accuracy of the sparse representation, ADMM will be used to solve the sparse representation problem under the obtained $\mathbf{D}$ [105]. To that end, the sparse representation problem in (5.2), which is a convex optimisation problem with respect to $\mathbf{S}_x$ and $\mathbf{S}_y$, will be reformulated. First, the following matrices are introduced:

$$\mathbf{Z}_x = \mathbf{S}_x, \tag{5.3}$$

$$\mathbf{Z}_y = \mathbf{S}_y \ . \tag{5.4}$$

The sparse representation problem in (5.2) is then equivalent to

$$\min_{\mathbf{s}_{x,i},\mathbf{s}_{y,i},\mathbf{z}_{x,i},\mathbf{z}_{y,i}} \left\{ \sum_{i=1}^{L} \{ \frac{1}{2} \parallel \mathbf{x}_i - \mathbf{D}\mathbf{s}_{x,i} \parallel_2^2 + \frac{1}{2} \parallel \mathbf{y}_i - \mathbf{D}\mathbf{s}_{y,i} \parallel_2^2 + \lambda_1 \parallel \mathbf{z}_{x,i} \parallel_1 + \lambda_2 \parallel \mathbf{z}_{y,i} \parallel_1 \} \right\},$$

$$\text{subject to } \mathbf{z}_{x,i} = \mathbf{s}_{x,i},\ \mathbf{z}_{y,i} = \mathbf{s}_{y,i}\ , \tag{5.5}$$

where $\mathbf{z}_{x,i}$ and $\mathbf{z}_{y,i}$ represent the ith column vectors of matrices $\mathbf{Z}_x$ and $\mathbf{Z}_y$, respectively. The augmented Lagrange function of the problem becomes

$$\begin{aligned} L_{\rho_1,\rho_2}(\mathbf{S}_x,\mathbf{S}_y,\mathbf{Z}_x,\mathbf{Z}_y,\beta_1,\beta_2) = \sum_{i=1}^{L} \Big\{ & \frac{1}{2} \parallel \mathbf{x}_i - \mathbf{D}\mathbf{s}_{x,i} \parallel_2^2 + \frac{1}{2} \parallel \mathbf{y}_i - \mathbf{D}\mathbf{s}_{y,i} \parallel_2^2 \\ & + \lambda_1 \parallel \mathbf{z}_{x,i} \parallel_1 + \lambda_2 \parallel \mathbf{z}_{y,i} \parallel_1 + \beta_1^T (\mathbf{z}_{x,i} - \mathbf{s}_{x,i}) \\ & + \beta_2^T (\mathbf{z}_{y,i} - \mathbf{s}_{y,i}) + \frac{\rho_1}{2} \parallel \mathbf{z}_{x,i} - \mathbf{s}_{x,i} \parallel_2^2 \\ & + \frac{\rho_2}{2} \parallel \mathbf{z}_{y,i} - \mathbf{s}_{y,i} \parallel_2^2 \Big\}, \end{aligned} \tag{5.6}$$

where β_1, β_2 are column vectors, known as Lagrange multipliers. As a result, the minimisation problem (5.5) equals the minimisation of augmented Lagrange function $L_{\rho_1,\rho_2}(\mathbf{S}_x,\mathbf{S}_y,\mathbf{Z}_x,\mathbf{Z}_y,\beta_1,\beta_2)$. The ADMM algorithm introduced in Section 2.4.5 updates $\mathbf{S}_x^{k+1},\mathbf{S}_y^{k+1},\mathbf{Z}_x^{k+1},\mathbf{Z}_y^{k+1},\beta_1^{k+1},\beta_2^{k+1}$ iteratively according to (2.40).

Another model of the sparse representation problem regarding contemporaneously recorded EEG and sEMG signals was considered too, in which $\mathbf{X}$ and $\mathbf{Y}$ have sparse representation under different dictionaries $\mathbf{D}_x$ and $\mathbf{D}_y$, respectively, but with a correlated part in these different dictionaries. The sparse signal representation is

formed as

$$\begin{aligned}\hat{\mathbf{X}} &= [\mathbf{D}_{x,1}\ \mathbf{D}_{x,2}] \begin{bmatrix}\mathbf{S}_{x,1}\\ \mathbf{S}_{x,2}\end{bmatrix} = \hat{\mathbf{X}}_1 + \hat{\mathbf{X}}_2, \\ \hat{\mathbf{Y}} &= [\mathbf{D}_{y,1}\ \mathbf{D}_{y,2}] \begin{bmatrix}\mathbf{S}_{y,1}\\ \mathbf{S}_{y,2}\end{bmatrix} = \hat{\mathbf{Y}}_1 + \hat{\mathbf{Y}}_2\ ,\end{aligned} \tag{5.7}$$

where $\mathbf{D}_{x,1}$ and $\mathbf{D}_{y,1}$ correspond to the uncorrelated part, while $\mathbf{D}_{x,2}$ and $\mathbf{D}_{y,2}$ correspond to the correlated part of the observed processes. Therefore, the coherent components $\hat{\mathbf{X}}_2$, $\hat{\mathbf{Y}}_2$ and the incoherent components $\hat{\mathbf{X}}_1$, $\hat{\mathbf{Y}}_1$ are separated from each other. However, this approach requires some prior information about the dictionaries, which is typically not available in CMC analysis. For the model in (5.1), on the other hand, we learn a same dictionary without considering which atoms in it correspond to EEG or/and sEMG, without relying on any prior information. Therefore, (5.1) rather than (5.7) is used in this work.

Although sparse representation has the capacity to remove background noise, it may not be able to filter some components which are also irrelevant to the monitored activity. It turns out that sparse representation of EEG and sEMG signals alone is not sufficient to achieve a substantial increase in CMC levels (see Section 5.3.2), hence a further selection of coherent components using a greedy algorithm analogous to the selection algorithm of the COWICA methodology is considered. The complete CMC enhancement algorithm can be summarised as follows:

1) **Initial sparse representation.** Perform dictionary learning on input EEG and sEMG signals to obtain the dictionary $\mathbf{D}$ and then perform ADMM to obtain the sparse coefficient matrices $\mathbf{S}_x$ and $\mathbf{S}_y$. Any entries of $\mathbf{S}_x$ and

$\mathbf{S}_y$ below a threshold T_s are set to zero, and the sparse coefficient matrices become $\mathbf{S}_x^0$ and $\mathbf{S}_y^0$.

2) **Component selection initialisation.** Sparse coefficient matrix $\mathbf{S}_x^0$ is then used as the input for coherent component selection algorithm. The initial value of CMC, C_{xy}^0, is computed as the value of CMC between EEG and sEMG signals that are reconstructed with the dictionary $\mathbf{D}$ and the sparse coefficient matrices $\mathbf{S}_x^0$ and $\mathbf{S}_y^0$. Coefficient entry counters are set to $p = 1$ and $q = 1$, and the iteration counter is set to $g = 1$.

3) **Coefficient removal.** If the (p,q)th entry of sparse coefficient matrix is zero, jump to step 5), otherwise set $\mathbf{S}_x^0(p,q) = 0$. The sparse coefficient matrix is thus updated with the (p,q)th coefficient cleared, and EEG signal is reconstructed with the updated matrix of sparse coefficients and dictionary $\mathbf{D}$.

4) **CMC estimation and sparse coefficient decision.** The CMC between sEMG and reconstructed EEG signals is calculated. If it is higher than C_{xy}^{g-1}, the coherence C_{xy}^g to be compared next time will be updated with the value of CMC calculated between sEMG and the reconstructed EEG signals. Otherwise, if the CMC is lower than or equal to C_{xy}^{g-1}, the (p,q)th coefficient $\mathbf{S}_x^0(p,q)$ is restored in the updated matrix of sparse coefficients and the reference coherence level is set to $C_{xy}^g = C_{xy}^{g-1}$.

5) **Iteration.** The indices are set to $p = p+1$ and $q = q$ if $p < K$ and $q \leq L$. Otherwise, if $p = K$ and $q < L$, the indices are set to $p = 1$ and $q = q+1$. Step 3) to step 5) are repeated until all coefficients have been considered, *i.e.* $p = K$ and $q = L$.

6) **Repeat the process with sEMG.** Reset the indices to $p = 1$ and $q = 1$. The whole selection process, steps 3) to 5) are repeated with $\mathbf{S}_y^0(p,q)$.

Remark. The coherence between EEG and sEMG is estimated in the short-time Fourier domain in order to keep their statistical properties fairly constant over considered time intervals [72, 75]. Since the length of EEG and sEMG segments used for dictionary learning and sparse representation could be longer than the length of window of short-time Fourier analysis (STFA) used for coherence calculation, the highest coherence among all possible time shifts of the STFA is taken into account in the component selection decision in step 4) and in setting up the reference value in step 2) of the algorithm.

5.3.2 Results and discussion

The performance of the proposed approach based on sparse representation in terms of coherence enhancement using simulated data under different SNRs is investigated first. The method was applied to simulated EEG and sEMG of Channel 1, as described in Section 5.2.2. The size of the dictionary was set to 600 and the parameter λ, which controls the degree of sparsity was set to 0.05. The impact of the size of dictionary and the value of λ will be discussed later in this section. Results of this experiment are shown in Table 5.5.

The results in Table 5.5 show that the CMC values between simulated EEG and sEMG reconstructed with their sparse matrices before applying further component selection do not increase much compared to the CMC values between original simulated EEG an sEMG, but they increase to very high levels after applying further component selection algorithm, even if the SNR is as low as -20 dB. It should be noted that the CMC levels may not increase to such high levels

when physiological signals are used, due to their much more complex dynamics. In comparison with COWICA, the results of which are shown in Table 5.1, the proposed method based on sparse representation achieves a much more pronounced CMC enhancement.

Table 5.5 Increase of CMC achieved by the proposed method based on sparse signal representation before and after further component selection for simulated data under different SNRs

SNR (dB)	Original	before further component selection		after further component selection	
	CMC value	CMC value	CMC increase (%)	CMC value	CMC increase (%)
-20	0.0354	0.0366	3.39	0.9493	2581.64
-15	0.1818	0.1871	3.19	0.9742	435.86
-10	0.4612	0.4743	2.84	0.9872	114.05
-5	0.7146	0.7224	1.09	0.9877	38.21

The algorithm is then assessed on the physiological data. EEG and FDI segments of 128-sample, 256-sample and 512-sample length around two prominent coherence peaks (Peak 1 and Peak 2 introduced in Section 4.3.2), which were acquired during the experiment presented in Chapter 3, were used for dictionary learning and sparse representation. Learning using segments of 250 ms (256 samples) gave the best performance for the physiological recordings, the length of 256-sample was chosen for EEG and FDI segments in the estimation. However, during the process of component selection, the coherence between reconstructed EEG and sEMG signals was calculated using STFA windows of length 125 ms, as described in Section 3.3, due to the desired trade-off between time and frequency resolutions.

Table 5.6 illustrates the impact of the size of dictionary on the effectiveness of CMC enhancement. CMC values of Peak 2 for subject B obtained by means of the proposed method before and after further component selection using dictionaries

of different sizes are shown in Table 5.6, where λ was set to 0.05. It can be noticed that the benefit of increasing the number of atoms beyond 800 is minor. Since investigating the influence of dictionary size is very computationally demanding, dictionaries of sizes larger than 800 were not considered in experiments with data of other subjects. In fact, for some other subject, highest coherence values were obtained with dictionaries consisting 400 or 600 atoms.

To investigate the influence of λ_1 and λ_2 in (5.5) on the performance of the algorithm, the coherence levels are assessed at the two prominent peaks for $\lambda_1 = \lambda_2 = \lambda$. The results corresponding to the two peaks of all considered subjects, before the component selection algorithm, for different values of λ are shown in Table 5.7. As per the discussion in the previous paragraph, three dictionary sizes were considered in this experiment: 400, 600 and 800. The results which are shown in the table correspond to dictionary sizes which gave highest coherence. It can be observed from Table 5.7 that the CMC could decrease when λ is high, which could be due to the fact that although by increasing the sparsity one could remove more noise, some useful components could be eliminated in the process too. Results in Table 5.7 also show that with adequately selected λ the coherence between reconstructed EEG and sEMG corresponding to the sparse expansion matrices obtained via ADMM can be increased compared to the coherence between original EEG and sEMG signals. However, the increase is rather small. This is because although in the process of sparse representation much of background noise could be filtered out, some components not involved in the observed motor control task may not be removed. The selection of components is thus essential for further extraction of coherent components.

Table 5.6 CMC values between reconstruct EEG and sEMG before and after further component selection under different sizes of dictionary

Number of atoms	CMC value	
	Before further component selection	After further component selection
400	0.1310	0.2353
600	0.1429	0.4037
800	0.1484	0.5608
1000	0.1428	0.5682
1200	0.1474	0.5264
1500	0.1430	0.5730

Table 5.7 CMC values between EEG and sEMG reconstructed with their sparse expansion matrices obtained by ADMM under different values of λ compared to CMC value between original EEG and sEMG corresponding to Peak1 and Peak 2

Peak	Subject	Coherence value					
		Original	After ADMM under different values of λ				
			0.01	0.05	0.1	0.2	0.3
Peak 1	B	0.1575	0.1599	0.1577	0.1386	0.1049	0.0566
	J	0.1107	0.1129	0.1204	0.1256	0.1322	0.1335
	K	0.1856	0.1867	0.1722	0.1509	0.1117	0.0923
	L	0.0897	0.0905	0.0940	0.0971	0.1070	0.1132
	N	0.0839	0.0855	0.0908	0.0951	0.0740	0.0433
Peak 2	B	0.1356	0.1400	0.1429	0.1359	0.1126	0.0351
	J	0.0842	0.0846	0.0840	0.0829	0.0781	0.0723
	K	0.1490	0.1515	0.1481	0.1330	0.1030	0.0830
	L	0.0771	0.0775	0.0772	0.0767	0.0746	0.0717
	N	0.0578	0.0629	0.0634	0.0661	0.0539	0.0370

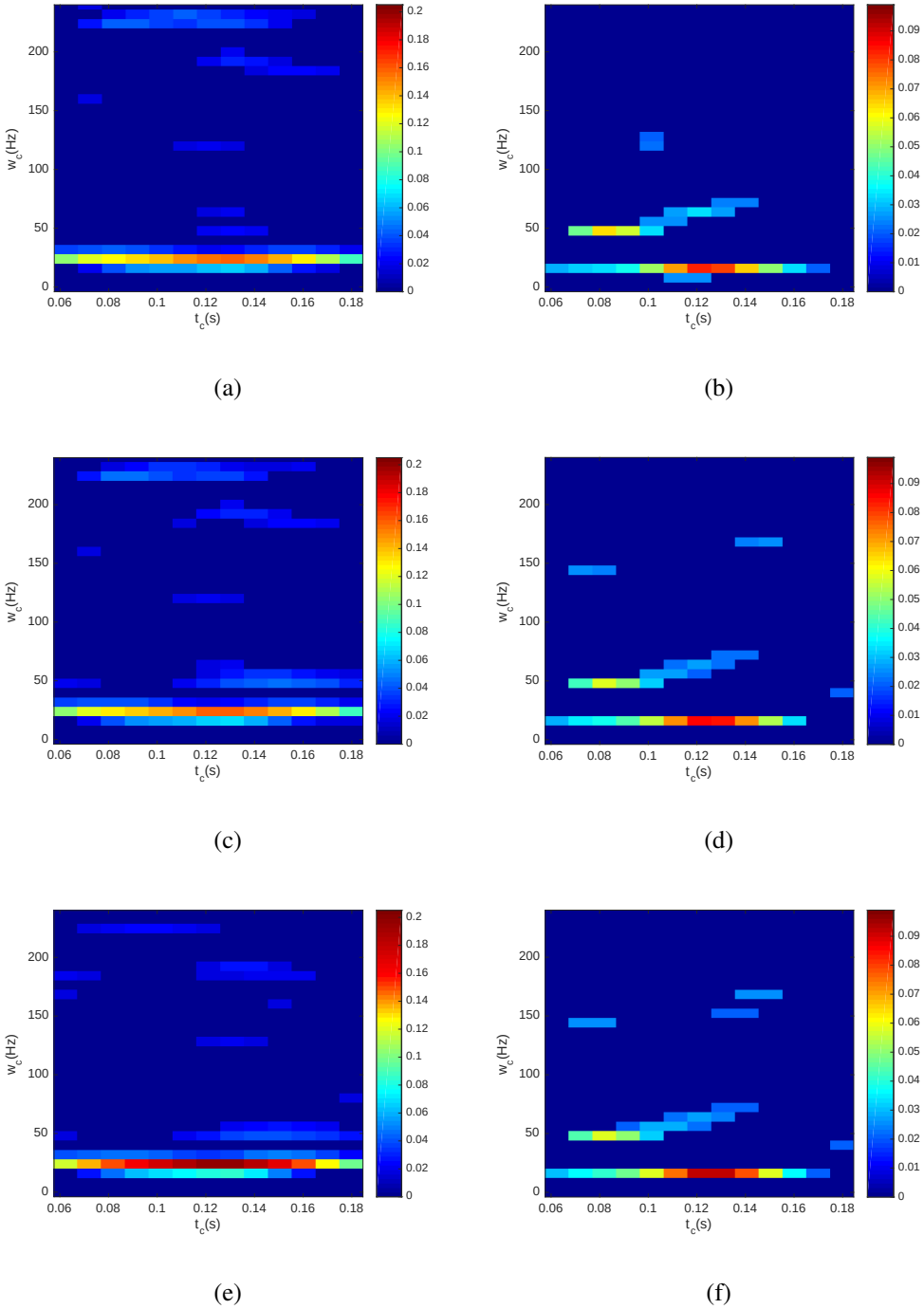

Fig. 5.3 Comparison between the CMC corresponding to original signals (top), signals after applying the denoising method based on sparse representation before further component selection (middle) and reconstructed signals after the further component selection (bottom). The plots correspond to segments of 256-sample length around Peak 1. CMC values below the 95% confidence limit are set to zero. Plots on the left are for subject B and plots on the right are for subject N. Note that the x axis represents the relative time in the segment instead of the time instant corresponding to the whole signal.

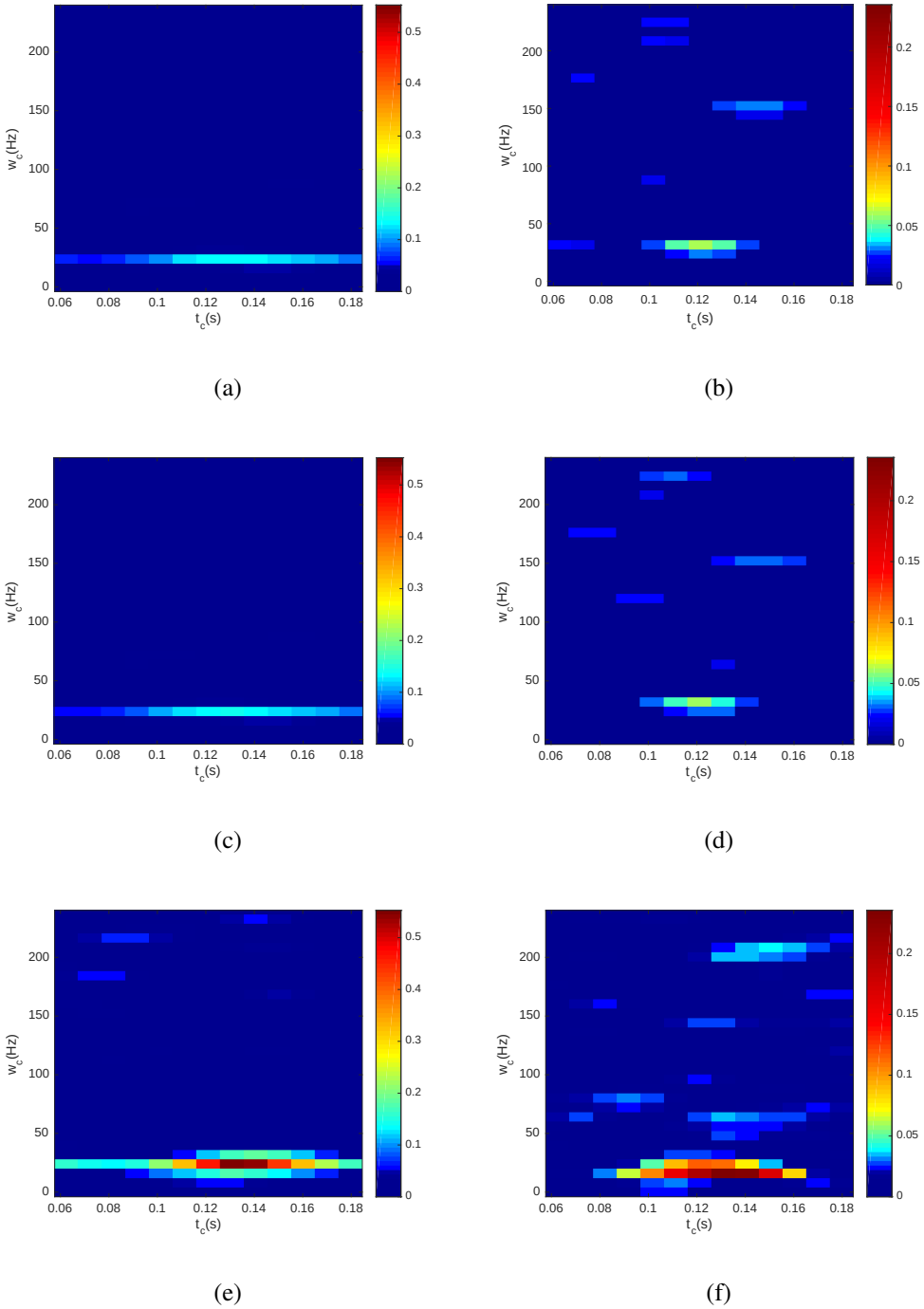

Fig. 5.4 Comparison between the CMC corresponding to original signals (top), signals after applying the denoising method based on sparse representation before further component selection (middle) and reconstructed signals after the further component selection (bottom). The plots correspond to segments of 256-sample length around Peak 2. CMC values below the 95% confidence limit are set to zero. Plots on the left are for subject B and plots on the right are for subject N. Note that the x axis represents the relative time in the segment instead of the time instant corresponding to the whole signal.

Fig. 5.3 and Fig. 5.4 compare the coherence between reconstructed EEG and sEMG signals around Peak 1 and Peak 2 after component selection to the corresponding coherence between original EEG and sEMG signals, as well as the corresponding coherence between reconstructed EEG and sEMG before component selection. The sparsity control parameter was set to $\lambda = 0.05$. It can be observed from these figures that owing to the further component selection, the overall method achieves significant increase on the levels of coherence. Moreover, around the coherence peaks, more β-range coherence is brought above the significance level by employing the component selection algorithm. The increase of coherence can also be observed in frequency regions where it is typically not expected, either before or after applying the component selection method, *e.g.* around 120 Hz in Fig. 5.4(d) and around 200 Hz in Fig. 5.4(f). Nonetheless, its level is much lower than the level of peak coherence which is observed in β range. A possible explanation is that although CMC is observed primarily within the β range in this study, it does not mean that there are no coherent components corresponding to other frequency ranges, since it can be observed that significant coherence spreads over the whole frequency domain in the plots of CMC between original EEG and sEMG signals. The components selected to maximise the CMC at peak frequency could also contribute to the CMC in other frequency ranges. In addition, the significant coherence, as defined by the 95% CL, may need to be reconsidered in the framework of sparse approximations.

The increase of coherence corresponding to the two prominent peaks of each subject is shown in Table 5.8. It can be observed that the increase of coherence corresponding to Peak 2 is substantial. However, coherence increase around Peak 1 is not as high; in fact, it is even slightly lower than the increase achieved by COWICA, as shown in Table 5.2, except in the case of subject L. As it was men-

tioned in Section 4.3.2, there could be more pronounced bidirectional signalling around Peak 1, than around Peak 2, and the algorithm based on dictionary learning may not have as good performance in bidirectional signalling scenarios as it has when signals are transmitted in just one direction. Peak 1 of subject L, on the other hand, occurs at 2.123 s, *i.e.* around one second after the mechanical stimulus, and the movement control perhaps stabilises by that time, which could explain this behaviour of the algorithm.

Note that in the process of dictionary learning, the initialised **D** is random. The obtained dictionary could thus be different for every initialisation, which could yield different results in terms of the increase of CMC. In experiments reported in this section, 100 initialisations were considered and the best results among all initialisations were reported.

Table 5.8 Increase of CMC achieved by the proposed method based on sparse signal processing after the further component selection

Subject	Peak 1		Peak 2	
	Coherence value	Coherence increase (%)	Coherence value	Coherence increase (%)
B	0.2046	29.90	0.5608	313.57
J	0.1335	20.60	0.1389	64.96
K	0.1966	5.93	0.2555	71.48
L	0.3374	276.14	0.1684	118.42
N	0.0998	18.95	0.1994	244.98

5.4 Conclusions

There are many previous approaches to denoising EEG and sEMG signals that rely on the abilities of wavelet analysis and/or ICA to facilitate the removal of

noise components. The limitation of applying such approaches to our research on denoising for coherence enhancement is that WTD may not be capable of removing some components unrelated to monitored activity which are not generally considered as noise. In the case of ICA, the number of channels has a considerable effect on its ability to separate independent sources. Since the number of estimated source signals cannot be larger than the number of observed mixtures, when the EEG and sEMG signals were acquired using a small number of channels ICA may fail to separate the source signals.

This chapter presented a denoising method, COWICA, based on the joint use of wavelet decomposition, ICA and a component selection algorithm. Firstly, wavelet decomposition generated wavelet components so that the effective number of mixtures increased. ICA was then applied to those wavelet components for source separation. Lastly, sEMG signal was reconstructed with the independent components in the wavelet transform domain. The components were selected by the algorithm with the purpose of contributing the coherence between monitored cortex and muscle activities.

By using simulated data, the effectiveness of COWICA under different SNRs was investigated. The potential of the proposed method to increase CMC levels by using physiological data was also illustrated in a comparative assessment along with WTD, which was commonly used for noise removal of biological signals. The COWICA approach showed a better performance in terms of increasing CMC levels at prominent coherence peaks. A particularly appealing feature of the method is that it is effective even when there are only two channels of sEMG.

In addition to COWICA, the coherent component enhancement via dictionary learning and sparse representation was proposed. Two models of the sparse representation problem were proposed, among which the model that did not require

prior information about the dictionary was chosen, where no such information was provided. By assuming a same dictionary for EEG and sEMG signals, the coherence between EEG and sEMG can be enhanced by investigating the relevance of the coefficients of their sparse expansions with respect to that dictionary. After generating the dictionary, ADMM was applied to find appropriate sparse representations. A component selection algorithm was then used to extract coherent components from the sparse expansions. The proposed method showed a very good performance in terms of the CMC enhancement for both simulated data and physiological EEG and sEMG signals, and in most cases it considerably outperformed COWICA. Situations in which COWICA achieved better results are scenarios in which one could expect more pronounced bidirectional signalling.

Chapter 6

CONCLUSIONS

This chapter concludes the thesis. The content of the thesis is summarised in Section 6.1. In Section 6.2 the main results are reviewed and the further work is discussed.

6.1 Summary

This thesis was concerned with discovering cortex-muscle interactions by developing a set of signal processing tools and measurement protocols which can be applied to EEG and EMG signals collected during a controlled motor task. One of the most commonly used signal processing methods that can be used to study the mechanisms of cortex-muscle interactions is CMC analysis. This thesis has focussed on two main factors that weaken the CMC thereby making communications between the motor cortex and muscles difficult to detect: 1) time delay and 2) component unrelated to observed activity.

In Chapter 1, the motivation of the research concerning the unmet clinical need for movement disorders was pointed out. The important role of CMC analysis

for understanding the underlying physiology so as to explore more individualised therapies was indicated. The importance of enhancing CMC for the detection of the synchrony between EEG and sEMG signals was introduced. The influence of time delay between coherent EEG and EMG events, and incoherent components involved in synchronously recorded EEG and EMG signals on the level of CMC was discussed.

In Chapter 2, background for understanding motor control system and CMC analysis, and existing relevant methodologies were discussed. First, a model of motor control system involving different delays and attenuations of the pathways was introduced, and the case of bidirectional propagation was discussed. Next, techniques for coherence analysis, including STFT and WT, were described. The effects of different time-frequency resolutions were discussed using EEG and EMG data recorded simultaneously during a motor task presented in Chapter 3. The main factors that decrease the level of CMC were discussed. Then, the existing methods for time delay estimation between EEG and EMG events were reviewed, with their limitations discussed. Finally, the noise reduction problem was introduced. Some denoising techniques in this context of biological signal processing were reviewed. WICA was touched upon, which could overcome the limitations imposed on ICA and encompass the advantages of both the wavelet decomposition and ICA. Dictionary learning and sparse signal representation were introduced.

Chapter 3 described the experiment for the collection of physiological signals used in this thesis. The experiment was designed and the recorded datasets were pre-processed. STFT was applied to the pre-processed EEG and EMG signals for CMC analysis. The frequency range of interest was β range, where the CMC was observed primarily in this study. The time instant corresponding to the time

when stimulus was delivered separated the whole period into two periods: pre- and post-stimulus periods. In order to avoid the possible influence of artefacts caused by the rapid movement, the immediate post-stimulus period was excluded in the estimation in Chapter 4 and Chapter 5.

In Chapter 4, the goal was to investigate the temporal relationship and estimate the time lag between coupled EEG and EMG signals. The concept of CMCTL was introduced, which was motivated by the need to compensate for the unknown delay between coupled cortex and muscle processes. The potential of CMCTL function to enhance CMC and provide information about temporal structures of cortex-muscle interactions was illustrated and compared to the conventional CMC. Due to the multiple paths involved in the information transmission between cortex and the periphery, each of which potentially introduces a different delay, the notion of the global delay was introduced to define the delay in the context of multi-path propagation. Simulated data were used to demonstrate that the time lag between EEG and EMG segments at points of local maxima of CMCTL corresponds to the average delay along the involved cortico-muscular conduction pathways when assuming Gaussian distributions to the delays. By applying the methods to physiological data, the results showed that delay estimates obtained by the proposed algorithm are in closer agreement with underlying physiology than those obtained by state-of-the-art methods. Further considerations with regard to healthy subjects where significant CMC cannot be observed were discussed. Examples showing the importance of adequate time-frequency resolution of spectral analysis and the capability of CMCTL to increase the coherence above the significant level were given. The CMCTL estimated the time delay, but exhibited limited ability for CMC enhancement. Denoising techniques were thus required.

Finally, Chapter 5 focused on CMC enhancement by the means of noise rejection. The noise includes not only the artefacts but also signals irrelevant to the considered cortical and motor activities in this thesis. Two approaches towards increasing the level of the synchronous EEG-EMG components were proposed and applied to the simulated data and the physiological data. ICA, combined with wavelet decomposition and a novel component selection algorithm was applied to sEMG signals from only two channels. Compared to WTD, the results by applying the proposed method to physiological data is more effective in terms of CMC enhancement. The problems occurring when combining this approach with the CMCTL approach were discussed. The other denoising approach was developed on the basis of sparse signal representation, which achieved an extraordinarily remarkable increase of CMC in some cases.

6.2 Discussion and Future Work

The potential of using neurophysiological techniques in motor neuroscience has not been fully realised, due to that the computational methods currently used in motor neurophysiology are severely limited in their ability to interpret relevant information. Particularly, the technique of CMC analysis has limitations that hinder its clinical use. In the first place, it is not easy to detect CMC in every healthy individual. In addition, CMC is even harder to detect during movement. These limitations, as suggested by previous work, are not only physiological [13], but as a result of the fact that dynamic cortico-muscular interactions are difficult to detect because of the limited capability of coherence analysis in its basic form [21, 23, 121]. The need for exploring advanced signal processing methods for the analysis of CMC has been pronounced.

Previous attempts to overcome these limitations include the use of directed coherence, rooted in multivariate autoregressive (MVAR) modelling [16, 35–37]. However, this approach sometimes requires a very large number of parameters, raising concerns about its applicability in the context of cortex-muscle interactions [37]. The aim of this thesis is to investigate some related methods further, propose advanced approaches to enhance CMC and explore important information for the study on cortico-muscular interactions.

As one of the main factors which decrease the level of CMC, the time delay between the coherent cortical and muscle activities is worth to investigate. Not only can CMC be enhanced by compensating the time delay, but also important information concerning the communications between the brain and muscles can be revealed by the delay estimation. Several methodologies regarding the delay estimation in biological systems have been proposed, many of which are based on the phase estimate. However, the phase-based estimation suffers from many problems. Hilbert transform has been used to deal with the problem caused by non-linear phase component. Unfortunately, its technical complexity and underlying assumptions restrain it from being applied to physiological studies. The time delay estimation in this thesis is obtained by using the method derived from the coherence function between two signals with their versions shifted in time. Although the concept of estimating the delay as the time offset that maximises coherence between EEG and EMG has already been proposed, the previous approach has some limitations and may not be applicable to EEG and EMG signals. The method proposed in this thesis uses STFT to estimate the coherence between nonstationary processes. Compared to the observation period of previous estimation which is commonly long enough to involve several events, the length of window regarding STFT in this study is much shorter. As discussed in this

thesis, adequate time-frequency resolution of spectral analysis can enhance the coherence by increasing the ratio between relevant components and noise. Finding optimal solutions of nonuniform time-frequency resolution is suggested for further research. In addition, the transmission in the cortico-muscular conduction system is not unidirectional and it is not via a single path. On one hand, directed coherence based on the Granger causality has been considered to solve the problem brought about by bidirectional connectivity, but the results with different individuals are highly inconsistent. On the other hand, since it involves different delays introduced by multiple paths, the delay in such a system has not been well defined. This thesis introduces the notion of global delay regarding bidirectional and multi-path propagation, presenting its physical interpretation mathematically and demonstrating that under certain assumptions, it corresponds to the average delay along the involved pathways. Additionally, EMG rectification that has been performed prior to CMC calculation in most studies has aroused controversy recently, on account of its non-linear nature. Thus, EMG rectification is avoided in this thesis. The above points result in a proposed method for estimating the time delay involved in cortex-muscle interactions, which can be identified as the main contribution of this thesis. Despite its potential to increase coherence levels by compensating the time delay between simultaneously recorded EEG and EMG signals, the method provides better information about the temporal structure of cortico-muscular interactions compared to the conventional CMC analysis.

When the relevant EEG and EMG components are considerably weak compared to the rest of components, alignment may not be able to enhance the coherence above the significant threshold. In order to increase the signal to noise ratio, where in this case signal refers to relevant EEG and EMG components involved in considered activity and noise encompasses components unrelated to

the process of interest, denoising techniques should be applied to the contaminated signals for the removal of noise. In terms of biological signals, WTD is a standard denoising technique. Although it can remove some noise such as background noise, some other irrelevant components may still remain. Some methodologies based on the joint use of wavelet decomposition and ICA have been proposed in the past, usually for artefact rejection from EEG signals [50–53, 55]. The wavelet decomposition has been used prior to ICA for diverse aims in previous research. One of the aims is to emphasise the non-Gaussian nature of the observed signals [122]. Besides, the wavelet decomposition itself can be used to remove artefacts [52, 53, 123]. Moreover, the effective number of mixtures can be increased by the wavelet decomposition, thus enhancing the performance of ICA regarding separating signals from a small number of channels [51, 55]. To minimise costs as well as simplify the operation for diagnostic data collection, low-channel count data acquisition is of great importance. Inspired by using wavelet decomposition to expand the numbers of mixtures, we propose to apply wavelet decomposition to generate wavelet components and then apply ICA to separate independent sources. The component selection algorithm is introduced to select the components with which the signals are reconstructed. The criterion of the component selection algorithm is to find the components that maximise the coherence at peak frequency. An interesting future work would be to explore this idea further using a larger number of channels obtained via High-Density sEMG.

Another proposed method regarding denoising of EEG and sEMG signals focused on the use of dictionary learning and sparse representation techniques, which have been widely used for denoising audio, video and image signals. Using the sparse signal representation makes it possible to filter components related to noise by spreading them with their intensity reduced. A common dictionary is

assumed for EEG and sEMG, and thus the investigation turned to their sparse coefficients. Even if the sparse representation alone cannot remove some of the components which are irrelevant to the considered activity, the further component selection algorithm helps to extract the coherent components.

References

[1] G. Abbruzzese and A. Berardelli, "Sensorimotor integration in movement disorders," *Movement disorders*, vol. 18, no. 3, pp. 231–240, 2003.

[2] M. Tinazzi, A. Priori, L. Bertolasi, E. Frasson, F. Mauguière, and A. Fiaschi, "Abnormal central integration of a dual somatosensory input in dystonia: Evidence for sensory overflow," *Brain*, vol. 123, no. 1, pp. 42–50, 2000.

[3] S. Baker, E. Olivier, and R. Lemon, "Coherent oscillations in monkey motor cortex and hand muscle EMG show task-dependent modulation," *J. Physiol.*, vol. 501, no. 1, pp. 225–241, 1997.

[4] B. Conway, D. Halliday, S. Farmer, U. Shahani, P. Maas, A. Weir, and J. Rosenberg, "Synchronization between motor cortex and spinal motoneuronal pool during the performance of a maintained motor task in man," *J. Physiol.*, vol. 489, no. Pt 3, pp. 917–924, 1995.

[5] D. M. Halliday, B. A. Conway, S. F. Farmer, and J. R. Rosenberg, "Using electroencephalography to study functional coupling between cortical activity and electromyograms during voluntary contractions in humans," *Neurosci. Lett.*, vol. 241, no. 1, pp. 5–8, 1998.

[6] S. Salenius, K. Portin, M. Kajola, R. Salmelin, and R. Hari, "Cortical control of human motoneuron firing during isometric contraction," *J. Neurophysiol.*, vol. 77, no. 6, pp. 3401–3405, 1997.

[7] P. Brown, S. Salenius, J. C. Rothwell, and R. Hari, "Cortical correlate of the Piper rhythm in humans," *J. Neurophysiol.*, vol. 80, no. 6, pp. 2911–2917, 1998.

[8] J. M. Kilner, S. N. Baker, S. Salenius, R. Hari, and R. N. Lemon, "Human cortical muscle coherence is directly related to specific motor parameters," *J. Neurosci.*, vol. 20, no. 23, pp. 8838–8845, 2000.

[9] J. Groß, P. Tass, S. Salenius, R. Hari, H.-J. Freund, and A. Schnitzler, "Cortico-muscular synchronization during isometric muscle contraction in humans as revealed by magnetoencephalography," *J. Physiol.*, vol. 527, no. 3, pp. 623–631, 2000.

[10] R. Kristeva, L. Patino, and W. Omlor, "Beta-range cortical motor spectral power and corticomuscular coherence as a mechanism for effective corticospinal interaction during steady-state motor output," *Neuroimage*, vol. 36, no. 3, pp. 785–792, 2007.

[11] R. Fisher, M. Galea, P. Brown, and R. Lemon, "Digital nerve anaesthesia decreases EMG-EMG coherence in a human precision grip task," *Experimental brain research*, vol. 145, no. 2, pp. 207–214, 2002.

[12] S. Graziadio, A. Basu, L. Tomasevic, F. Zappasodi, F. Tecchio, and J. A. Eyre, "Developmental tuning and decay in senescence of oscillations linking the corticospinal system," *J. Neurosci.*, vol. 30, no. 10, pp. 3663–3674, 2010.

[13] V. M. McClelland, Z. Cvetkovic, and K. R. Mills, "Modulation of corticomuscular coherence by peripheral stimuli," *Exp. Brain Res.*, vol. 219, no. 2, pp. 275–292, 2012.

[14] A. Stancak, T. T. Raij, M. Pohja, N. Forss, and R. Hari, "Oscillatory motor cortex–muscle coupling during painful laser and nonpainful tactile stimulation," *NeuroImage*, vol. 26, no. 3, pp. 793–800, 2005.

[15] M. Pohja and S. Salenius, "Modulation of cortex-muscle oscillatory interaction by ischaemia-induced deafferentation," *Neuroreport*, vol. 14, no. 3, pp. 321–324, 2003.

[16] C. L. Witham, C. N. Riddle, M. R. Baker, and S. N. Baker, "Contributions of descending and ascending pathways to corticomuscular coherence in humans," *J. Physiol.*, vol. 589, no. 15, pp. 3789–3800, 2011.

[17] C. N. Riddle and S. N. Baker, "Manipulation of peripheral neural feedback loops alters human corticomuscular coherence," *J. Physiol.*, vol. 566, no. 2, pp. 625–639, 2005.

[18] P. Brown, J. Marsden, L. Defebvre, F. Cassim, P. Mazzone, A. Oliviero, M. G. Altibrandi, V. Di Lazzaro, P. Limousin-Dowsey, V. Fraix, P. Odin, and P. Pollak, "Intermuscular coherence in Parkinson's disease: relationship to bradykinesia," *Neuroreport*, vol. 12, no. 11, pp. 2577–2581, 2001.

[19] S. Farmer, G. Sheean, M. Mayston, J. Rothwell, C. Marsden, B. Conway, D. Halliday, J. Rosenberg, and J. Stephens, "Abnormal motor unit synchronization of antagonist muscles underlies pathological co-contraction in upper limb dystonia." *Brain: a journal of neurology*, vol. 121, no. 5, pp. 801–814, 1998.

[20] P. Grosse, M. Edwards, M. Tijssen, A. Schrag, A. J. Lees, K. Bhatia, and P. Brown, "Patterns of EMG-EMG coherence in limb dystonia," *Movement disorders*, vol. 19, no. 7, pp. 758–769, 2004.

[21] V. M. McClelland, Z. Cvetkovic, and K. R. Mills, "Rectification of the EMG is an unnecessary and inappropriate step in the calculation of corticomuscular coherence," *J. Neurosci. Meth.*, vol. 205, no. 1, pp. 190–201, 2012.

[22] Y. Xu, V. M. McClelland, Z. Cvetkovic, and K. R. Mills, "Delay estimation between EEG and EMG via coherence with time lag," in *Proceedings of IEEE International Conference on Acoustics, Speech and Signal Processing (ICASSP)*, March 2016, pp. 734–738.

[23] Y. Xu, V. M. McClelland, Z. Cvetković, and K. R. Mills, "Corticomuscular coherence with time lag with application to delay estimation," *IEEE Transactions on Biomedical Engineering*, vol. 64, no. 3, pp. 588–600, March 2017.

[24] P. Brown, "Cortical drives to human muscle: the Piper and related rhythms," *Progress in neurobiology*, vol. 60, no. 1, pp. 97–108, 2000.

[25] P. Grosse, M. Cassidy, and P. Brown, "EEG-EMG, MEG-EMG and EMG-EMG frequency analysis: physiological principles and clinical applications," *Clin. Neurophysiol.*, vol. 113, pp. 1523–1531, 2002.

[26] R. Bortel and P. Sovka, "EEG-EMG coherence enhancement," *Signal Processing*, vol. 86, no. 7, pp. 1737–1751, 2006.

[27] G. C. Carter, "Bias in magnitude-squared coherence estimation due to misalignment," *IEEE Trans. Acoust., Speech, Signal Process.*, vol. 28, no. 1, pp. 97–99, 1980.

[28] T. Mima and M. Hallett, "Electroencephalographic analysis of corticomuscular coherence: reference effect, volume conduction and generator mechanism," *Clin. Neurophysiol.*, vol. 110, pp. 1892–1899, 1999.

[29] P. Brown, S. Farmer, D. Halliday, J. Marsden, and J. Rosenberg, "Coherent cortical and muscle discharge in cortical myoclonus," *Brain*, vol. 122, pp. 461–472, 1999.

[30] M. Lindemann, J. Raethjen, J. Timmer, G. Deuschl, and G. Pfister, "Delay estimation for cortico-peripheral relations," *J. Neurosci. Meth.*, vol. 111, pp. 127–139, 2001.

[31] F. Panzica, L. Canafoglia, S. Franceschetti, S. Binelli, C. Ciano, E. Visani, and G. Avanzini, "Movement-activated myoclonus in genetically defined progressive myoclonic epilepsies: EEG-EMG relationship estimated using autoregressive models," *Clin. Neurophysiol.*, vol. 114, pp. 1041–1052, 2003.

[32] T. Mima, J. Steger, A. E. Schulman, C. Gerloff, and M. Hallett, "Electroencephalographic measurement of motor cortex control of muscle activity in humans," *Clin. Neurophysiol.*, vol. 111, no. 2, pp. 326–337, 2000.

[33] M. Cassidy and P. Brown, "Spectral phase estimates in the setting of multidirectional coupling," *J. Neurosci. Meth.*, vol. 127, no. 1, pp. 95–103, 2003.

[34] S. F. Campfens, H. van der Kooij, and A. C. Schouten, "Face to phase: pitfalls in time delay estimation from coherency phase," *J. Comput. Neurosci.*, vol. 37, no. 1, pp. 1–8, 2014.

[35] S. N. Baker, M. Chiu, and E. E. Fetz, "Afferent encoding of central oscillations in the monkey arm," *J. Neurophysiol.*, vol. 95, no. 6, pp. 3904–3910, 2006.

[36] E. R. Williams, D. S. Soteropoulos, and S. N. Baker, "Coherence between motor cortical activity and peripheral discontinuities during slow finger movements," *J. Neurophysiol.*, vol. 102, no. 2, pp. 1296–1309, 2009.

[37] C. L. Witham, M. Wang, and S. N. Baker, "Corticomuscular coherence between motor cortex, somatosensory areas and forearm muscles in the monkey," *Front. Syst. Neurosci.*, vol. 4, 2010.

[38] G. C. Carter, "Coherence and time delay estimation," *Proceedings of the IEEE*, vol. 75, no. 2, pp. 236–255, 1987.

[39] R. Govindan, J. Raethjen, F. Kopper, J. Claussen, and G. Deuschl, "Estimation of time delay by coherence analysis," *Physica A*, vol. 350, pp. 277–295, 2005.

[40] J. V. Basmajian and C. J. De Luca, *Muscles alive: their functions revealed by electromyography*. Williams & Wilkins, 1985.

[41] C. J. De Luca and R. Merletti, "Surface myoelectric signal cross-talk among muscles of the leg," *Electroencephalography and clinical neurophysiology*, vol. 69, no. 6, pp. 568–575, 1988.

[42] K. Türker and T. Miles, "Cross-talk from other muscles can contaminate EMG signals in reflex studies of the human leg," *Neuroscience letters*, vol. 111, no. 1, pp. 164–169, 1990.

[43] D. Moshou, I. Hostens, G. Papaioannou, and H. Ramon, "Wavelets and self-organising maps in electromyogram (EMG) analysis," in *Proceedings of the ESIT*, 2000, pp. 14–15.

[44] A. Phinyomark, C. Limsakul, and P. Phukpattaranont, "An optimal wavelet function based on wavelet denoising for multifunction myoelectric control," in *Proceedings of the 6th International Conference on Electrical Engineering/Electronics, Computer, Telecommunications and Information Technology*, vol. 02, May 2009, pp. 1098–1101.

[45] L. Yu, "EEG de-noising based on wavelet transformation," in *Proceedings of the 3rd International Conference on Bioinformatics and Biomedical Engineering*, June 2009, pp. 1–4.

[46] R. N. Vigário, "Extraction of ocular artefacts from EEG using independent component analysis," *Electroencephalography and clinical neurophysiology*, vol. 103, no. 3, pp. 395–404, 1997.

[47] H. Nakamura, M. Yoshida, M. Kotani, K. Akazawa, and T. Moritani, "The application of independent component analysis to the multi-channel surface electromyographic signals for separation of motor unit action potential trains: part I—measuring techniques," *Journal of Electromyography and Kinesiology*, vol. 14, no. 4, pp. 423–432, 2004.

[48] T.-P. Jung, S. Makeig, C. Humphries, T.-W. Lee, M. J. Mckeown, V. Iragui, and T. J. Sejnowski, "Removing electroencephalographic artifacts by blind source separation," *Psychophysiology*, vol. 37, no. 2, pp. 163–178, 2000.

[49] R. Vigário, J. Sarela, V. Jousmiki, M. Hamalainen, and E. Oja, "Independent component approach to the analysis of EEG and MEG recordings," *IEEE transactions on biomedical engineering*, vol. 47, no. 5, pp. 589–593, 2000.

[50] X. Ren, Z. Yan, Z. Wang, and X. Hu, "Noise reduction based on ICA decomposition and wavelet transform for the extraction of motor unit action potentials," *J. Neurosci. Meth.*, vol. 158, no. 2, pp. 313–322, 2006.

[51] G. Inuso, F. La Foresta, N. Mammone, and F. C. Morabito, "Wavelet-ICA methodology for efficient artifact removal from electroencephalographic recordings," in *Proceedings of IEEE International Joint Conference on Neural Networks (IJCNN)*. IEEE, 2007, pp. 1524–1529.

[52] M. Zima, P. Tichavskỳ, K. Paul, and V. Krajča, "Robust removal of short-duration artifacts in long neonatal EEG recordings using wavelet-enhanced ICA and adaptive combining of tentative reconstructions," *Physiological measurement*, vol. 33, no. 8, p. N39, 2012.

[53] N. P. Castellanos and V. A. Makarov, "Recovering EEG brain signals: artifact suppression with wavelet enhanced independent component analysis," *J. Neurosci. Meth.*, vol. 158, no. 2, pp. 300–312, 2006.

[54] A. Hyvärinen, P. Ramkumar, L. Parkkonen, and R. Hari, "Independent component analysis of short-time Fourier transforms for spontaneous EEG/MEG analysis," *NeuroImage*, vol. 49, no. 1, pp. 257–271, 2010.

[55] N. Mammone, F. La Foresta, and F. C. Morabito, "Automatic artifact rejection from multichannel scalp EEG by wavelet ICA," *IEEE Sens. J.*, vol. 12, no. 3, pp. 533–542, 2012.

[56] J. Mairal, M. Elad, and G. Sapiro, "Sparse representation for color image restoration," *IEEE Transactions on image processing*, vol. 17, no. 1, pp. 53–69, 2008.

[57] B. Shen, W. Hu, Y. Zhang, and Y. J. Zhang, "Image inpainting via sparse representation," in *Proceedings of IEEE International Conference on Acoustics, Speech and Signal Processing*, April 2009, pp. 697–700.

[58] J. Wright, A. Y. Yang, A. Ganesh, S. S. Sastry, and Y. Ma, "Robust face recognition via sparse representation," *IEEE transactions on pattern analysis and machine intelligence*, vol. 31, no. 2, pp. 210–227, 2009.

[59] S. Aviyente, "Compressed sensing framework for EEG compression," in *Proceedings of IEEE/SP 14th Workshop on Statistical Signal Processing*, Aug 2007, pp. 181–184.

[60] H. Yu, H. Lu, T. Ouyang, H. Liu, and B. L. Lu, "Vigilance detection based on sparse representation of EEG," in *Proceedings of Annual International Conference of the IEEE Engineering in Medicine and Biology*, Aug 2010, pp. 2439–2442.

[61] M. Shokrollahi and S. Krishnan, "Sleep EMG analysis using sparse signal representation and classification," in *Proceedings of Annual International Conference of the IEEE Engineering in Medicine and Biology Society*, Aug 2012, pp. 3480–3483.

[62] C. Trenado, I. Mendez-Balbuena, E. Manjarrez, F. Huethe, J. Schulte-Mönting, B. Feige, M.-C. Hepp-Reymond, and R. Kristeva, "Enhanced corticomuscular coherence by external stochastic noise," *Frontiers in human neuroscience*, vol. 8, p. 325, 2014.

[63] H. Piitulainen, A. Botter, M. Bourguignon, V. Jousmäki, and R. Hari, "Spatial variability in cortex-muscle coherence investigated with magnetoencephalography and high-density surface electromyography," *J. Neurophysiol.*, vol. 114, no. 5, pp. 2843–2853, 2015.

[64] G. Birò and L. D. Partridge, "Analysis of multiunit spike records." *J. Appl. Physiol.*, vol. 30, no. 4, pp. 521–526, 1971.

[65] J. Weytjens and D. van Steenberghe, "The effects of motor unit synchronization on the power spectrum of the electromyogram," *Biol. Cybern.*, vol. 51, no. 2, pp. 71–77, 1984.

[66] D. F. Stegeman, J. H. Blok, H. J. Hermens, and K. Roeleveld, "Surface EMG models: properties and applications," *J. Electromyogr. Kines.*, vol. 10, no. 5, pp. 313–326, 2000.

[67] A. Merlo, D. Farina, and R. Merletti, "A fast and reliable technique for muscle activity detection from surface EMG signals," *IEEE Trans. Biomed. Eng.*, vol. 50, no. 3, pp. 316–323, 2003.

[68] J. Lataire and R. Pintelon, "Estimating a nonparametric colored-noise model for linear slowly time-varying systems," *IEEE Transactions on Instrumentation and Measurement*, vol. 58, no. 5, pp. 1535–1545, 2009.

[69] B. Bamieh and L. Giarre, "Identification of linear parameter varying models," *International journal of robust and nonlinear control*, vol. 12, no. 9, pp. 841–853, 2002.

[70] J. Rosenberg, A. Amjad, P. Breeze, D. Brillinger, and D. Halliday, "The Fourier approach to the identification of functional coupling between neuronal spike trains," *Prog. Biophys. Mol. Biol.*, vol. 53, no. 1, pp. 1–31, 1989.

[71] J. S. Bendat and A. G. Piersol, "Measurement and analysis of random data," *International Journal of Control*, 1966.

[72] G. Carter, C. Knapp, and A. Nuttall, "Estimation of the magnitude-squared coherence function via overlapped fast fourier transform processing," *IEEE Trans. Audio Electroacoust.*, vol. 21, no. 4, pp. 337–344, 1973.

[73] R. La Bouquin-Jeannes, A. A. Azirani, and G. Faucon, "Enhancement of speech degraded by coherent and incoherent noise using a cross-spectral estimator," *IEEE Transactions on Speech and Audio Processing*, vol. 5, no. 5, pp. 484–487, 1997.

[74] L. Cohen, *Time-frequency analysis*. Prentice Hall PTR Englewood Cliffs, NJ:, 1995, vol. 778.

[75] Z. Cvetkovic, "On discrete short-time Fourier analysis," *IEEE Trans. Signal Processing*, vol. 48, no. 9, pp. 2628–2640, 2000.

[76] J. B. Allen and L. R. Rabiner, "A unified approach to short-time Fourier analysis and synthesis," *Proceedings of the IEEE*, vol. 65, no. 11, pp. 1558–1564, 1977.

[77] M. Vetterli and J. Kovacevic, *Wavelets and Subband Coding*. Prentice-hall, 1995, no. LCAV-BOOK-1995-001.

[78] J.-P. Lachaux, A. Lutz, D. Rudrauf, D. Cosmelli, M. Le Van Quyen, J. Martinerie, and F. Varela, "Estimating the time-course of coherence between single-trial brain signals: an introduction to wavelet coherence," *Neurophysiologie Clinique/Clinical Neurophysiology*, vol. 32, no. 3, pp. 157–174, 2002.

[79] Z. Sankari, H. Adeli, and A. Adeli, "Wavelet coherence model for diagnosis of Alzheimer disease," *Clinical EEG and neuroscience*, vol. 43, no. 4, pp. 268–278, 2012.

[80] A. Klein, T. Sauer, A. Jedynak, and W. Skrandies, "Conventional and wavelet coherence applied to sensory-evoked electrical brain activity," *IEEE transactions on biomedical engineering*, vol. 53, no. 2, pp. 266–272, 2006.

[81] D. R. Brillinger, *Time Series: Data Analysis and Theory*. Siam, 1981, vol. 36.

[82] A. Piersol, "Time delay estimation using phase data," *IEEE Trans. Acoust., Speech, Signal Process.*, vol. 29, no. 3, pp. 471–477, 1981.

[83] M. S. Brandstein and H. F. Silverman, "A robust method for speech signal time-delay estimation in reverberant rooms," in *Proceedings of IEEE International Conference on Acoustics, Speech and Signal Processing (ICASSP-97)*, vol. 1, 1997, pp. 375–378.

[84] V. O. Alan, W. S. Ronald, and R. John, *Discrete-time signal processing*. New Jersey, Printice Hall Inc, 1989.

[85] P. Grosse, R. Guerrini, L. Parmeggiani, P. Bonanni, A. Pogosyan, and P. Brown, "Abnormal corticomuscular and intermuscular coupling in high-frequency rhythmic myoclonus," *Brain*, vol. 126, no. 2, pp. 326–342, 2003.

[86] O. P. Neto and E. A. Christou, "Rectification of the EMG signal impairs the identification of oscillatory input to the muscle," *J. Neurophysiol.*, vol. 103, no. 2, pp. 1093–1103, 2010.

[87] D. Farina, R. Merletti, and R. M. Enoka, "The extraction of neural strategies from the surface EMG," *J. Appl. Physiol.*, vol. 96, no. 4, pp. 1486–1495, 2004.

[88] V. M. McClelland, Z. Cvetkovic, and K. R. Mills, "EMG rectification has inconsistent effects on coherence analysis even in single motor unit studies," *J. Neurophysiol.*, vol. 111, no. 5, pp. 1150–1150, 2014.

[89] A. N. Akansu and R. A. Haddad, *Multiresolution signal decomposition: transforms, subbands, and wavelets*. Academic Press, 2001.

[90] S. G. Mallat, "A theory for multiresolution signal decomposition: the wavelet representation," *IEEE transactions on pattern analysis and machine intelligence*, vol. 11, no. 7, pp. 674–693, 1989.

[91] D. L. Donoho, "De-noising by soft-thresholding," *IEEE transactions on information theory*, vol. 41, no. 3, pp. 613–627, 1995.

[92] S. G. Chang, B. Yu, and M. Vetterli, "Adaptive wavelet thresholding for image denoising and compression," *IEEE Transactions on image processing*, vol. 9, no. 9, pp. 1532–1546, 2000.

[93] A. Hyvärinen and E. Oja, "Independent component analysis: algorithms and applications," *Neural Networks*, vol. 13, no. 4, pp. 411–430, 2000.

[94] T. M. Cover and J. A. Thomas, *Elements of Information Theory*. John Wiley & Sons, 2012.

[95] J.-F. Cardoso, "High-order contrasts for independent component analysis," *Neural Computation*, vol. 11, no. 1, pp. 157–192, 1999.

[96] G. R. Naik, D. K. Kumar, and H. Weghorn, "Performance comparison of ICA algorithms for isometric hand gesture identification using surface EMG," in *Proceedings of the 3rd International Conference on Intelligent Sensors, Sensor Networks and Information*, Dec 2007, pp. 613–618.

[97] G. R. Naik and D. K. Kumar, "Identification of hand and finger movements using multi run ICA of surface electromyogram," *Journal of medical systems*, vol. 36, no. 2, pp. 841–851, 2012.

[98] G. R. Naik, D. K. Kumar, V. Yadav, K. Wheeler, and S. Arjunan, "Testing of motor unit synchronization model for localized muscle fatigue," in *Proceedings of Annual International Conference of the IEEE Engineering in Medicine and Biology Society*, Sept 2009, pp. 360–363.

[99] A. Subasi and M. K. Kiymik, "Muscle fatigue detection in EMG using time–frequency methods, ICA and neural networks," *Journal of medical systems*, vol. 34, no. 4, pp. 777–785, 2010.

[100] M. J. McKeown and R. Radtke, "Phasic and tonic coupling between EEG and EMG demonstrated with independent component analysis," *J. Clin. Neurophysiol.*, vol. 18, no. 1, pp. 45–57, 2001.

[101] B. Azzerboni, M. Carpentieri, F. L. Foresta, and F. C. Morabito, "Neural-ICA and wavelet transform for artifacts removal in surface EMG," in *Proceedings of IEEE International Joint Conference on Neural Networks*, vol. 4, July 2004, pp. 3223–3228 vol.4.

[102] D. L. Donoho, "For most large underdetermined systems of linear equations the minimal ℓ_1-norm solution is also the sparsest solution," *Communications on pure and applied mathematics*, vol. 59, no. 6, pp. 797–829, 2006.

[103] K. Engan, S. O. Aase, and J. H. Husoy, "Method of optimal directions for frame design," in *Proceedings of IEEE International Conference on Acoustics, Speech, and Signal Processing. (ICASSP99)*, vol. 5, 1999, pp. 2443–2446 vol.5.

[104] M. Aharon, M. Elad, and A. Bruckstein, "K-SVD: An algorithm for designing overcomplete dictionaries for sparse representation," *IEEE Transactions on signal processing*, vol. 54, no. 11, pp. 4311–4322, 2006.

[105] S. Boyd, N. Parikh, E. Chu, B. Peleato, and J. Eckstein, "Distributed optimization and statistical learning via the alternating direction method of multipliers," *Foundations and Trends® in Machine Learning*, vol. 3, no. 1, pp. 1–122, 2011.

[106] T. Mima and M. Hallett, "Corticomuscular coherence: a review," *J. Clin. Neurophysiol.*, vol. 16, no. 6, pp. 501–511, 1999.

[107] K. G. Keenan, D. Farina, K. S. Maluf, R. Merletti, and R. M. Enoka, "Influence of amplitude cancellation on the simulated surface electromyogram," *J. Appl. Physiol.*, vol. 98, no. 1, pp. 120–131, 2005.

[108] R. Hodes, M. Larrabee, and W. German, "The human electromyogram in response to nerve stimulation and the conduction velocity of motor axons: studies on normal and on injured peripheral nerves," *Arch. Neuro. Psychiatr.*, vol. 60, no. 4, pp. 340–365, 1948.

[109] M. Vecchierini-Blineau and P. Guiheneuc, "Electrophysiological study of the peripheral nervous system in children. changes in proximal and distal conduction velocities from birth to age 5 years." *J. Neurol. Neurosur. Ps.*, vol. 42, no. 8, pp. 753–759, 1979.

[110] G. Parry and J. Steinberg, *Guillain-Barré Syndrome: From Diagnosis to Recovery*. Demos Medical Publishing, 2007.

[111] N. Hogan and R. W. Mann, "Myoelectric signal processing: Optimal estimation applied to electromyography - Part I: Derivation of the optimal myoprocessor," *IEEE Trans. Biomed. Eng.*, vol. BME-27, no. 7, pp. 382–395, July 1980.

[112] ——, "Myoelectric signal processing: Optimal estimation applied to electromyography - Part II: Experimental demonstration of optimal myoprocessor performance," *IEEE Trans. Biomed. Eng.*, vol. BME-27, no. 7, pp. 396–410, July 1980.

[113] P. A. Parker, J. A. Stuller, and R. N. Scott, "Signal processing for the multistate myoelectric channel," *Proceedings of the IEEE*, vol. 65, no. 5, pp. 662–674, May 1977.

[114] E. Clancy and N. Hogan, "Single site electromyograph amplitude estimation," *IEEE Trans. Biomed. Eng.*, vol. 41, no. 2, pp. 159–167, Feb 1994.

[115] ——, "Probability density of the surface electromyogram and its relation to amplitude detectors," *IEEE Trans. Biomed. Eng.*, vol. 46, no. 6, pp. 730–739, June 1999.

[116] A. Siegel and H. N. Sapru, *Essential Neuroscience*. Lippincott Williams & Wilkins, 2006.

[117] T. Xu, W. Wang, and W. Dai, "Sparse coding with adaptive dictionary learning for underdetermined blind speech separation," *Speech Communication*, vol. 55, no. 3, pp. 432–450, 2013.

[118] D. A. Bridwell, S. Rachakonda, R. F. Silva, G. D. Pearlson, and V. D. Calhoun, "Spatiospectral decomposition of multi-subject EEG: Evaluating blind source separation algorithms on real and realistic simulated data," *Brain topography*, pp. 1–15, 2016.

[119] E. J. Candes and T. Tao, "Decoding by linear programming," *IEEE transactions on information theory*, vol. 51, no. 12, pp. 4203–4215, 2005.

[120] R. Chartrand and V. Staneva, "Restricted isometry properties and nonconvex compressive sensing," *Inverse Problems*, vol. 24, no. 3, p. 035020, 2008.

[121] Y. Xu, V. M. McClelland, Z. Cvetković, and K. R. Mills, "Cortico-muscular coherence enhancement via coherent wavelet enhanced independent component analysis," in *Proceedings of the 39th Annual International Conference of the IEEE Engineering in Medicine and Biology Society (EMBC)*, July 2017, pp. 2786–2789.

[122] M. R. Mirarab, H. Dehghani, and A. Pourmohammad, "A novel wavelet based ICA technique using kurtosis," in *Proceedings of the 2nd International Conference on Signal Processing Systems*, vol. 1, July 2010, pp. V1–36–V1–39.

[123] S. Calcagno, F. La Foresta, and M. Versaci, "Independent component analysis and discrete wavelet transform for artifact removal in biomedical signal processing," *American Journal of Applied Sciences*, vol. 11, no. 1, p. 57, 2014.